EXPERIMENTAL INVESTIGATION OF IMPURITIES AND THEIR EFFECT ON ACOUSTO-ELECTRIC PROPERTIES OF LITHIUM NIOBATE

A Dissertation
presented in partial fulfillment of requirements
for the degree of Doctor of Philosophy
in the Department of Physics and Astronomy
The University of Mississippi

by

CHANDRIMA CHATTERJEE

May 2018

ABSTRACT

Lithium niobate ($LiNbO_3$ or LN) is a versatile material with widespread applications. Thus its fundamental properties continue to be of interest. At the same time, LN contains impurities and point defects, which affect its physical properties. This in turn could influence the performance of the practical devices using the specific properties. Thus it is important to identify these impurities, and predict what properties they might influence. This research aims at finding new crystal characteristics including the identification of point defects, and finding the distribution of the defects parallel to the optical crystallographic z-axis, and in a direction normal to the z-axis. Bulk crystals, wafers and ferroelectric phononic crystals such as periodically poled LN (PPLN) are studied. The spectra of photoluminescence (PL) reveal both charged and neutral impurities. The impurities may be classified as heavy metals, noble gases, color centers and antisite defects. The band scheme of LN is developed with the presence of intraband donor or acceptor levels. The impurities show a peak and valley distribution both parallel and normal to the z-axis. The distribution of the impurities and point defects in PPLN, can be used to identify the ferroelectric domain walls. Engineering application of these findings may be non-destructive characterization of phononic crystals.

The impurities and point defects affect crystal properties including conductivity, electromechanical transformation (EMT) and others. The charged defects are sensitive to local electric polarization, thus they affect the EMT at local points of the crystal. The EMT distribution reveals peaks and valleys. The distance between consecutive peaks and valleys of the

EMT distribution is similar to those obtained from PL measurements. Frequency dependence of the radio frequency admittance reveals peaks and valleys, which corresponds to specific ultrasonic modes in a plate. The revealed correlation between defects and EMT is a basis for nonlinear phenomena involving piezoelectricity including nonclassical nonlinearity, acoustical memory and others.

DEDICATION

This dissertation is dedicated to my family and teachers, whose love, support, patience and encouragement, guided me through this journey.

LIST OF SYMBOLS

T_{ij}	Component of the stress tensor
S_{ij}	Component of the strain tensor
ε_{ij}	Component of the dielectric tensor
e_{ij}	Component of the piezoelectric tensor, it is the induced polarization in the direction i per unit stress applied in direction j
g_{ij}	Induced electric field in direction i per unit stress applied in direction j
c_{ijkl}	Elastic stiffness tensor
s_{ijkl}	Elastic compliance tensor
d	Domain length
P	Periodicity of impurities and point defects. It is the distance between consecutive peaks or consecutive valleys in the distribution of impurities and point defects.
ξ	Acoustical displacement
k	Total electromechanical coupling coefficient
k_0	Part of the electromechanical coupling coefficient independent of impurities and point defects

k_d	Part of the electromechanical coupling coefficient dependent on impurities and point defects
ρ	Density of crystal
V	Voltage generated by mechanical stress
E	Electric field
D	Dielectric displacement
v	Velocity of the propagating acoustical wave
ω	Angular frequency

ACKNOWLEDGMENTS

I would like to thank my research advisor Dr. Igor Ostrovskii for giving me the opportunity to work with him. His guidance was extremely valuable to experimentally investigate impurities in lithium niobate and find out their influence on the acousto-electric properties of the material. The completion of this dissertation would not have been possible without the support of the Dissertation Committee members. I would like to thank Dr. Lucien Cremaldi, Dr. Cecille Labuda and Dr. Alexander Yakovlev for their interest in my research and their time commitment to the prospectus and dissertation.

I am very grateful to Dr. Lucien Cremaldi, Dr. Luca Bombelli, Dr. Kevin Beach and the faculty and staff of the Department of Physics and Astronomy for their encouragement and support since the first day I entered the department as a graduate student. I would like to thank the department for financially supporting me all along, to successfully defend my PhD dissertation. I also sincerely thank the graduate school for providing me with the dissertation fellowship in spring 2017. My experience as a graduate student is truly amazing and I cherish the year 2016 when I co-founded and presided over the University of Mississippi Women in Physics (UMWiP) group. I am extremely grateful to Dr. Cecille Labuda and Dr. Katherine Dooley who guided and supported me all along, from writing the grant proposal to request money for the group, establishing the group and ensure its smooth running. I sincerely thank my family members for always being there for me.

TABLE OF CONTENTS

LIST OF FIGURES

LIST OF TABLES

CHAPTER I

INTRODUCTION

1.1 Overview

Lithium niobate (chemical formula: $LiNbO_3$, abbreviated as LN) possesses exceptional electro-optic[1, 2, 3], acoustic[1], piezoelectric[1, 2], pyroelectric[1] and non-linear optical properties[2, 3]. It is used to tailor a wide range of products such as Bragg gratings[4], waveguides[5], holographic storage media[6], two-dimensional nonlinear photonic crystals[7], high temperature ultrasonic transducers[8 ,9], high performance acoustic surface wave transducers and delay lines[10].

LN is a ferroelectric material melting at about 1250°C. It has a Curie temperature of 1210°C. Single crystals of this material were first prepared by using the Czochralski technique of pulling from the melt[11]. The ideal composition of LN for growth is at the congruency point. The congruent composition contains between 48.4 molar % to 48.6 molar % Li_2O[12-18]. This means that the crystals contain many intrinsic defects[14]. Chemical and radiation treatment[13] also create defects which are ions of heavy metals.

Point intrinsic and extrinsic defects, which consist of ions of transition metals and rare-earth elements, are important defects in LN. The defects have an influence on the properties of the material, such as domain structure, electro-optical coefficients, light absorption, refractive indices, and others[13].

LN produces a nonclassical nonlinearity. This was observed as a non-exponential echo train[19-21]. Structural inhomogeneity of ferroelectric LN may be the cause[22]. The investigation of defects in LN has a long history with many publications on this topic[13, 23-30]. But the relationship between the defects and the acousto-electric properties has not yet been established. The purpose of this research is to establish a connection between the two. The following sections in this chapter are devoted to building the foundation for this research.

1.2 Development of Ultrasonics in Solids

Human beings are gifted with sense organs. One of them is the sense of hearing. Hearing is a long range interaction that is caused by sound waves. The animals that have perfected the sophisticated art of communication using sound waves are underwater mammals like whales and dolphins. They use ultrasound for communication. Ultrasound is a very powerful technology used in physical acoustics. It is the band in the acoustic spectrum above 20 kHz. It continues up into the MHz range, and finally at around 1GHz, it goes over into the hypersonic domain. Ultrasonic waves travel slowly, about 100,000 times slower than electromagnetic waves. This provides a way to display information in time. Ultrasonic waves can also easily penetrate opaque materials which visible light cannot. Since ultrasonic wave sources are inexpensive, sensitive, reliable, they provide a highly desirable method to image the interior of opaque objects.

The piezoelectric transducer led to some of the earliest and most important applications. One of the most important areas in low frequency Bulk Acoustic Wave (BAW) work was the development of Ultrasonic imaging[31-34]. By varying the position and angle of the transducer, several types of scans like the line scan, vertical scan and horizontal cross section scans were developed. The Surface Acoustic Wave (SAW) was discovered very early in the 1880s by Lord Rayleigh. However, in the device field it remained a scientific curiosity with very few applications until the development of the inter-digital transducer (IDT) by White and Voltmer in the 1960s[31]. IDTs convert acoustic waves to electrical signals and vice-versa by exploiting the piezoelectric properties of certain materials, for instance quartz, lithium niobate, lithium tantalite, lanthanum gallium silicate, and others[35]. Since then, SAW has been successfully used in TV filters[36, 37,] in signal processing[38], and sensors[39-42]. High power ultrasonics was one of the first areas of ultrasonics to be developed, but its theory has remained poorly developed[31]. It has heavy duty industrial applications and is a useful way to supply large amounts of heat, leading to ultrasonic soldering and welding of metals and plastics. Ultrasound is becoming increasingly important in medicine and is now taking its place along with X-ray and nuclear medicine as an important diagnostic tool[43-47]. In many ways, ultrasound is an ideal diagnostic tool; it is noninvasive, externally applied, non-traumatic and safe at acoustical intensities encountered in existing diagnostic equipment.

The non-destructive testing (NDT) is a wide group of analysis techniques used in science and industry to evaluate the properties of a material, component or system, without causing damage[48]. Because NDT does not permanently alter the article being inspected, it is a highly valuable technique that can save both money and time in product evaluation, troubleshooting and research. The most powerful way of evaluating material degradation is the ultrasonic method, since the characteristics of ultrasonic wave propagation are directly related to the properties of the material[49]. Most conventional methods use ultrasonic characteristics in the linear elastic region. However, they are sensitive only to gross defects but much less sensitive to micro-damage. In recent years, nonlinear ultrasonic behavior such as higher-harmonic generation, nonlinear resonance and mixed frequency response has been studied as a positive method for overcoming these limitations.

The interaction of light and sound was discovered early in the history of ultrasonics. Brillouin predicted the diffraction of light by an acoustic wave in 1922[50]. This was then confirmed with experimentation by Debye and Sears in 1932[51]. Acousto-optic effects are based on the change of the refractive index of a medium due to the presence of sound waves in the medium. Sound waves produce a refractive index grating in the material, and it is this grating that is "seen" by the light wave[52]. The variations in the refractive index, due to pressure fluctuations may be detected optically by refraction, diffraction and interference effects[53].

1.3 Strain Tensor

The basic idea is that forces will be applied to solid bodies to deform them. As a starting point there is a need to describe the deformation. If a point at $\vec{r}$ from the origin is displaced to a position $\overrightarrow{r'}$ by the force, then the deformation $\vec{u} = \overrightarrow{r'_i} - \vec{r}$ is called the displacement vector. In tensor notation $u_i = x'_i - x_i$ where u_i and x'_i are functions of x_i. The displacement of a point during deformation causes the distance dl between two closely spaced points to change. Before deformation

$$dl^2 = dx_1^2 + dx_2^2 + dx_3^2 = dx_i^2 \tag{1.1}$$

after deformation

$$dl'^2 = dx_i'^2 \tag{1.2}$$

Hence

$$dl'^2 = (dx_i + du_i)^2 \tag{1.3}$$

Using

$$du_i = \left(\frac{\partial u_i}{\partial x_k}\right) dx_k \tag{1.4}$$

$$dl'^2 = dl^2 + 2\frac{\partial u_i}{\partial x_k} dx_i dx_k + \frac{\partial u_i}{\partial x_k}\frac{\partial u_i}{\partial x_l} dx_k dx_l \tag{1.5}$$

this can be written as

$$dl'^2 = dl^2 + 2S_{ik} dx_i dx_k \tag{1.6}$$

where

$$S_{ik} = \frac{1}{2}\left(\frac{\partial u_i}{\partial x_k} + \frac{\partial u_k}{\partial x_i} + \frac{\partial u_l}{\partial x_i}\frac{\partial u_l}{\partial x_k}\right) \tag{1.7}$$

If the strains are sufficiently small, which will always be assumed to be the case in linear ultrasonics, then the quadratic terms can be ignored. The strain tensor S_{ik} is then

$$S_{ik} = \frac{1}{2}\left(\frac{\partial u_i}{\partial x_k} + \frac{\partial u_k}{\partial x_i}\right) \tag{1.8}$$

By construction, the strain tensor is symmetric so that nine terms reduce to six. Clearly three of these are diagonal and three are off-diagonal. Each diagonal term ($i = k = 1, 2$ or 3) has the simple significance shown in Figure 1-1. For example

$$S_{11} = \frac{\partial u_1}{\partial x_1} \tag{1.9}$$

is clearly the extension per unit length in the x_1 direction. Hence, the diagonal terms correspond to compression or expansion along one of the three axes. The off-diagonal terms can be understood with reference to Figure 1-1 for the case of a deformation of the plane, perpendicular to the z-axis. For small deformations,

$$\tan\alpha_1 \approx \alpha_1 = \frac{\partial u_y}{\partial x}, \tan\alpha_2 \approx \alpha_2 = \frac{\partial u_x}{\partial y} \tag{1.10}$$

where α_1 and α_2 are angles with the x-axis and y-axis, respectively. Thus the change in angle between the two sides of the rectangle is

$$\alpha_1 + \alpha_2 = \frac{\partial u_x}{\partial y} + \frac{\partial u_y}{\partial x} \tag{1.11}$$

is proportional to the shear strain S_{xy}.

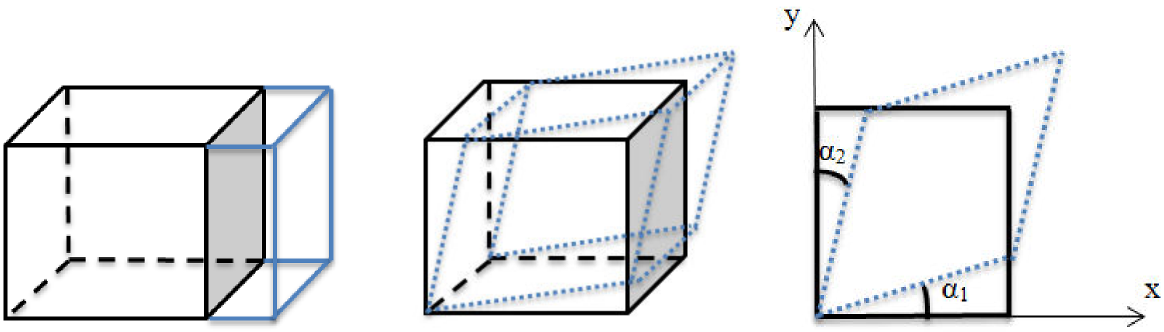

(a) (b) (c)

Figure 1-1. Strains for a unit cube: (a) Tensile strain u_{xx}, (b) Shear strain u_{xy}, (c) Definition of angles for shear strain u_{xy}.

1.4 Stress Tensor

We consider a body in static equilibrium under external forces such that there is no net translation or rotation. What is of interest is the effect of internal forces on a hypothetical unit cube inside the solid. There could be two types of forces acting on the cube; body forces acting on the volume or surface forces. Body forces such as gravity will not be considered, so that a description is needed for surface forces acting on the face of the cube. These forces will lead to deformation of the cube, which can be described by the strain tensor discussed in section 1.3.

Figure 1-2 shows that an applied force will generally be at some arbitrary angle to the unit cube. Since we are considering forces on the faces of the cube, we consider a particular face, for example, the xy face with normal along the z-axis.

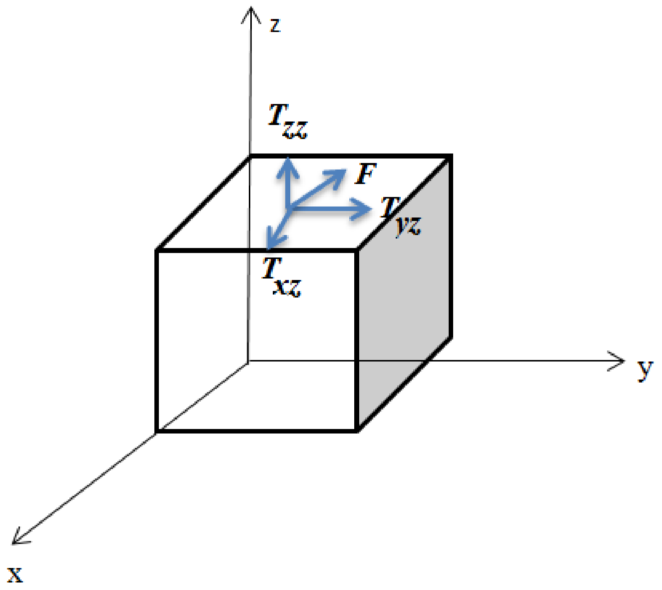

Figure 1-2: Definition of components of the stress tensor.

The components of the applied force can be separated into two major classes: (a) Normal components to the face giving rise to compressive or tensile stresses. (b) Tangential components, giving rise to shear stresses. For the example considered, there are two of these: dF_x and dF_y.

In one dimension, the stress on a rod is defined as the force per unit area. Extending this definition to three dimensions, clearly there are two vectors involves. The first one is in the direction of the surface normal and the second one is in the direction of the force. It follows that in three dimensions, the stress must be described by a stress tensor of rank two, as observed from equation 1.12.

$$T_{zz} = \frac{F_z}{A_z}, T_{zy} = \frac{T_z}{A_y}, T_{zx} = \frac{F_z}{A_x} \tag{1.12}$$

so that all components are described by a stress tensor of rank two.

1.5 Hooke's Law

In its simplest form, Hooke's law states that for small elongations of an elastic system, the stress is proportional to the strain. In order to prove Hooke's las, the stress T_{ij} is expanded as a Taylor series in the strain S_{kl}.

$$T_{ij} = T_{ij}(0) + \left(\frac{\partial T_{ij}}{\partial S_{kl}} \right)_{S_{kl}=0} S_{kl} + \frac{1}{2} \left(\frac{\partial^2 T_{kl}}{\partial S_{ij} \partial S_{mn}} \right)_{S_{ij}=0, S_{mn}=0} S_{ij} S_{mn} + \ldots.. \tag{1.13}$$

The first term $T_{ij}(0) = 0$ at $S_{ij} = 0$, since stress and strain go to zero simultaneously for elastic solids. The third nonlinear term will be neglected here; it forms the basis of the third-order elastic constants and nonlinear acoustics. In linear elasticity, the series is truncated after the second term, leading to

$$T_{ij} = c_{ijkl} S_{kl} \tag{1.14}$$

where

$$c_{ijkl} = \left(\frac{\partial T_{ij}}{\partial S_{kl}} \right)_{S_{kl}=0} \tag{1.15}$$

is known as the elastic stiffness tensor or elastic constant tensor. The elastic compliance tensor s_{ijkl} is defined as the inverse of the stiffness tensor.

$$s_{ijkl} = c_{ijkl}^{-1} \tag{1.16}$$

The stiffness tensor is a fourth-rank tensor as it links two second-rank tensor. Since T_{ij} and S_{kl} are symmetric, c_{ijkl} is also symmetric.

$$c_{ijkl} = c_{jikl} = c_{ijlk} = c_{jilk} \tag{1.17}$$

The reciprocity is given by

$$c_{ijkl} = c_{klij} \tag{1.18}$$

These symmetry operations reduce the number of independent constants from 81 to 36 to 21 for crystals of different symmetries. The number varies from 21 (triclinic) to 3 (cubic). For isotropic solids there are only 2 independent elastic constants.

It is standard practice to use a reduced notation for the elastic constants, due to the symmetry of T_{ij} and S_{kl}. Since each of the latter has six independent components, the c_{ijkl} tensor has a maximum of 36. This leads to the reduced notation where $c_{\alpha\beta} \equiv c_{ijkl}$, where ij and kl go in pairs. The six α and β values are shown in Table 1-1.

Table 1-1. Conversion table from regular indices to reduced indices.

$\boldsymbol{\alpha, \beta}$	***ij, kl***
1	11
2	22
3	33
4	23=32
5	31=13
6	12=21

Hooke's law can be expressed in the reduced form as $T_i = c_{ij}S_j$ where *i, j* = 1 to 6. T_1, T_2, T_3 are longitudinal stresses and T_4, T_5, T_6 are transverse stresses. S_1, S_2, S_3 are longitudinal strain and S_4, S_5, S_6 are transverse strains.

In materials physics, elastic constants describe the inter-atomic force constants that are second derivatives of the energy with respect to atomic positions. Thus elastic constants provide important information about the atomic location and the structure of the lattice. Elastic constants are often associated with the behavior of materials such as speed of sound, Poisson's ratio, elastic anisotropy ratio[54-56], hardness[54, 57], ductility and brittleness[54, 58, 59], and others.

1.6 Lamb's Waves

Lamb waves propagate in solid plates. They are elastic waves whose particle motion lies in the plane that contains the direction of the wave propagation and the plate normal (the direction perpendicular to the plate). Lamb waves are constrained by the elastic properties of the plate or surface they are guided by. They have wide applications in non-destructive testing of materials[31]. In Lamb waves the partial wave modes are composed of longitudinal and transverse components in the sagittal plane. Lamb waves are dispersive, so the phase and group velocities vary with frequency. The particle motion in Lamb waves is elliptical with its x and z components depending on the depth within the plate. There are both symmetric and antisymmetric modes. The phenomenon of velocity dispersion leads to a rich variety of experimentally observed waveforms when acoustic waves propagate in plates. It is the group velocity v_g and not the phase velocity v_p, that determines the modulations seen in the waveform.

The zero modes are symmetric and antisymmetric. They are the only modes that exist over the entire frequency spectrum from zero to infinity. In low frequency modes (i.e. when the wavelength is greater than the plate thickness), they are often called the "extensional modes" and "flexural modes". The zero order symmetrical modes (S_0) travel at the plate velocity in the low frequency regime where it is properly called the 'extensional mode'. The plate stretches in the direction of propagation and contracts correspondingly in the thickness direction. As the frequency increases and the wavelength becomes comparable with the plate thickness, curving of the plate stats to have a significant influence on its effective stiffness. The phase velocity drops smoothly while the group velocity drops precipitously towards a minimum. At higher frequencies, both the phase and group velocities of the S_0 mode converge. The zero order antisymmetrical modes (A_0) are the 'flexural mode' or the bending mode. For very low frequencies, the group velocity is twice the phase velocity. The group and phase velocities of the A_0 mode converge at higher frequencies.

1.7 Piezoelectricity

Piezoelectricity was discovered in 1880 by the French physicists Jacques and Pierre Curie. This is the most widely used method to excite ultrasonic waves[31]. Piezoelectricity is the electric charge that accumulates in certain solid materials like crystals, certain ceramics, and biological matter such as bones, DNA, and certain proteins in response to applied mechanical stress[60]. This is the direct piezoelectric effect. The piezoelectric effect is understood as a linear electromechanical interaction between the mechanical and electrical state in crystalline materials with no inversion symmetry[61, 62]. The piezoelectric effect is a reversible process. So when a piezoelectric crystal is placed in an electric field, the crystal exhibits strain, i.e. the dimensions of the crystal change. This is the converse piezoelectric effect. For example, Lead Zirconate Titanate crystals will generate measurable piezoelectricity when their static structure is deformed by about 0.1 % of the original dimension. Conversely, those same crystals will change about 0.1 % of their static dimension when an external electric field is applied to the material[63]. The converse piezoelectric effect is used in the generation of ultrasonic sound waves[64].

The nature of the piezoelectric effect is closely related to the presence of electric dipole moments in solids. The latter may be induced for ions on crystal lattice sites with asymmetric charge surroundings (as in $BaTiO_3$), or may be directly carried by molecular groups (as in cane sugar). The dipole density or polarization (dimensionality Cm/m^3) may easily be calculated for crystals by summing up their dipole moments per volume of the crystallographic unit cell[65]. As every dipole is a vector, the dipole density P is a vector field. Dipoles near each other tend to be aligned in regions called Weiss domains[66]. Such materials are ferroelectric and will be discussed in detail in the next section. The domains are usually randomly oriented, but can be aligned using the process of poling. This is a process by which a strong electric field is applied across the material, usually at elevated temperature.

Let us consider a simple one dimensional model. Suppose that $\pm q$ are the charges of the positive and negative ions, and a is the charge in dimension of a unit cell. Again, for simplicity, we suppose one atom of piezoelectric material per unit cell. Then the induced polarization can be expressed as qa per unit cell volume eS, where e is the piezoelectric stress constant and S is the strain. Then the usual relation for dielectric media can be written as

$$D = \varepsilon_0 E + P \tag{1.19}$$

or

$$D = \varepsilon^S E + eS \tag{1.20}$$

where D and E are the electric displacement and electric field, respectively. The superscript S is standard in literature for such relations and corresponds to permittivity at constant or zero strain. In a similar way, it can be shown that

$$T = c^E S - eE \tag{1.21}$$

Equations (1.20) and (1.21) are known as the piezoelectric constitutive relations.

Since there are two electrical variables (D, E) and two mechanical variables (T, S), there are several different possible ways of writing the constitutive relations. In fact choosing one electrical and one mechanical quantity as independent variables, we easily find that there are four different sets of constitutive relations that can be written. If for example, we choose T and E as independent variables, we can write $S = S(T, E)$ and $D = D(T, E)$. For small variations one can make a Taylor expansion of S and D about equilibrium values and retain only the linear terms, resulting in

$$S = \left(\frac{\partial S}{\partial T}\right)T + \left(\frac{\partial S}{\partial E}\right)E \tag{1.22}$$

$$D = \left(\frac{\partial D}{\partial T}\right)T + \left(\frac{\partial D}{\partial E}\right)E \tag{1.23}$$

The proportionality constants are defined by

$$s^E = \left(\frac{\partial S}{\partial T}\right)_E, \; d = \left(\frac{\partial S}{\partial E}\right)_T = \left(\frac{\partial D}{\partial T}\right)_E \text{ and } \varepsilon^T = \left(\frac{\partial D}{\partial E}\right)_T \tag{1.24}$$

where the equality for d (and similar conditions for the other constitutive relations) can be obtained by thermodynamic considerations. Thus we have

$$S = s^E T + dE \tag{1.25}$$

$$D = dT + \varepsilon^T E \tag{1.26}$$

In a similar way for the other constitutive relations, we have

$$S = s^E T + dE \tag{1.27}$$

$$E = -gT + \beta^T D \tag{1.28}$$

$$T = c^E S - eE \tag{1.29}$$

$$D = eS + \varepsilon^S E \tag{1.30}$$

$$T = c^D S - hD \tag{1.31}$$

$$E = -hS + \beta^S D \tag{1.32}$$

The definition of piezoelectric constants follows from equations (1.25) to (1.32).

$$d = \left(\frac{\partial S}{\partial E} \right)_T = \left(\frac{\partial D}{\partial T} \right)_E \tag{1.33}$$

$$g = \left(-\frac{\partial E}{\partial T} \right)_D = \left(\frac{\partial S}{\partial D} \right)_T \tag{1.34}$$

$$e = \left(-\frac{\partial T}{\partial E} \right)_S = \left(\frac{\partial D}{\partial S} \right)_E \tag{1.35}$$

$$h = \left(-\frac{\partial T}{\partial D} \right)_S = \left(-\frac{\partial E}{\partial S} \right)_D \tag{1.36}$$

1.8 Ferroelectricity

A ferroelectric material has a spontaneous electric polarization that can be reversed by the application of an external electric field. Ferroelectricity was first discovered in Rochelle salt in 1920 by Valasek[67]. In general, the direction of spontaneous polarization is not the same throughout a macroscopic crystal[68]. Rather, the crystal consists of a number of domains; within each domain the polarization has a specific direction, but this direction varies from one domain to another. Ferroelectric materials show a hysteresis in the *P* versus *E* relationship as shown in Figure 1-3.

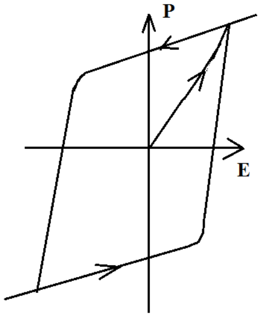

Figure 1-3. Schematic representation of hysteresis in the polarization (*P*) versus applied electric field (*E*) relationship.

Most materials exhibit ferroelectricity only below a certain phase transition temperature, called the Curie Temperature T_c, and are paraelectric above this temperature. The spontaneous polarization vanishes, and the ferroelectric crystal transforms into a paraelectric state. Many ferroelectrics lose their piezoelectric properties completely above T_c completely, because their paraelectric phase has centrosymmetric crystallographic structure[69].

Partition between domains with different directions of dipole polarizations are called domain walls. Domain walls are classified as 180° and non 180° walls. The polarization directions are antiparallel to each other on either side of a 180° domain wall. A material may have a combination of these domain walls. For example, in Barium titanate , the direction of polarization of neighbouring domains differs either by 90° or by 180°; this is a consequence of the three mutually perpendicular axes along which the spontaneous polarization may occur[68] .

A number of interesting experiments on the formation of domains and the motion of domain walls in $BaTiO_3$ have been carried out by Merz[68, 70]. His work shows that when an opposite electric field is applied in a direction opposite to that of the spontaneous polarization, a large number of new needle shaped domains of about 10^{-4} cm width are created , as shown in Figure 1-4[68] .

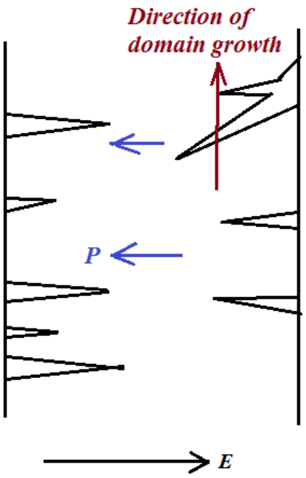

Figure 1-4. Schematic representation of new antiparallel domains resulting from application of an external field *E*. The arrows pointing to the right represent the direction of the electric field *E*, while the arrows pointing to the left represent the spontaneous polarization *P*. The arrow pointing up shows the direction of domain growth [68].

These new domains grow essentially in the forward direction rather than sideways. This behaviour is quite different from that of ferromagnetic materials, where the change in direction of magnetization is accomplished by the growth of domains which have the right direction of magnetization, the growth results from a sideways motion of the domain walls. This indicates that the forward coupling of the electric dipoles is much stronger than the sideways coupling. Merz has given some semiquantitative arguments which confirm this behaviour. When one estimates the energy per cm^2 of a domain wall between antiparallel domains , and minimizes this with respect to the wall thickness, it is found that the wall thickness is of the order of a few lattice distances. In contrast with this, the wall thickness in a ferromagnetic material is of the order of 300 lattice constants. Thus to move a domain wall in $BaTiO_3$ sideways over one lattice distance, requires an energy which is about equal to the energy of the wall itself. In a ferromagnetic material, it takes roughly 1/300 of the total wall energy to displace the wall over one lattice distance. For Rochelle salt and for KH_2PO_4, it has also been found that the wall thickness is considerably smaller than for ferromagnetic materials[68, 71].

The structure of ferroelectric domains is of practical interest because the ferroelectric domain wall contribution to the dielectric, piezoelectric, and elastic properties of ferroelectrics is quite significant, and these contributions can be several times larger than the intrinsic lattice piezoresponse[72]. Compared with the single crystal domain properties, the ferroelectric domain properties are more complicated in ceramics as a result of their elaborate aspects, such as the distribution of permittivity and polarization axes, the elastic and dielectric boundary conditions of the grains, and the internal properties of grain boundaries[72]. Furthermore, orthorhombic symmetry leads to much more complicated patterns in the distribution of domains than those of the tetragonal structures that are composed of only two types of domains (90° and 180°). The ferroelectric domain structure and morpholigy was studied in Li-doped $(K,Na)NbO_3$ or (KNN) ceramics, using a piezoresponse force microscope[72]. Four types of domains were observed in these material systems; they were (60°, 90°,120°,180°). The 90° domains were dominantly distributed. Figure 1-5 show the orientation of 90^o and non 90^o domain walls in ferroelectric materials.

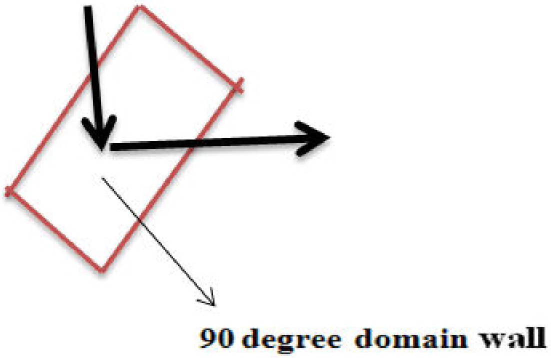

(a)

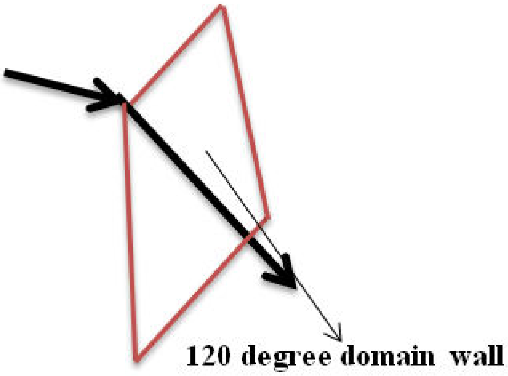

(b)

Figure 1-5. Polarization directions of domains (black arrow) and domain walls (in red) at (a) 90 degrees, (b) 120 degrees in ferroelectric materials.

Domain walls in ferroelectric materials were demonstrated to promote photovoltaic effects[73,74], enhanced electromechanical response[73,75], anomalous electron transport behaviour[73,76], magnetoresistive properties[73]. Despite all advances in theory and experiment, the experimental characterization of intrinsic domain walls remain a challenging task[73]. Scanning

Probe Microscopy (SPM) is the most common technique for gaining insight to the physics of ferroelectric domain walls and related effects. Today SPM variants, like the conductive atomic force microscopy (c-AFM) and piezoresponse force microscopy (PFM) are commonly used to measure the local electronic transport and piezoresponse at these domain walls[73] . Besides SPM, electron microscopy techniques, like transmission electron microscopy (TEM), or scanning electron microscopy (SEM) have been applied to gain valuable information about the structure[73]. High-resolution X-ray photoemission electron microscopy (X-PEEM) is also a well established method for imaging ferroelectric domain structures. In this method, the domain walls are visualized by analyzing the energy distribution of photo-excited electrons[73].

1.9 Defects in Crystals

Point defects are defects that occur only at or around a single lattice point. They are not extended in space in any dimension. Strict limits for how small a point defect is are generally not defined explicitly. Typically these defects involve at most a few extra or missing atoms. Many point defects, especially in ionic crystals, are called centers. For example a vacancy in many ionic solids is called a luminescence center, a color center or F-center. These defects permit ionic transport through crystals. Some point defects are discussed below.

Vacancy defects are lattice sites, which would be occupied in a perfect crystal, but are vacant. If a neighboring atom moves to occupy the vacant site, the vacancy moves in the opposite direction to the site, which used to be occupied by the moving atom. The stability of the surrounding crystal structure guarantees that the neighboring atoms will not simply collapse around the vacancy. In some materials, neighboring atoms actually move away from a vacancy, because they experience attraction from atoms in the surroundings. A vacancy (or pair of vacancies in an ionic solid) is sometimes called a Schottky defect.

Interstitial defects are those defects where atoms assume an unoccupied site in the crystal. In interstitial defects, two or more atoms may share the same lattice site, thereby increasing its total energy. Alternatively, small atoms in some crystals may occupy interstitial sites in energetically favorable configurations, such as hydrogen in palladium. A nearby pair of a vacancy and an interstitial is often called a Frenkel defect. This is caused when an ion moves into an interstitial site and creates a vacancy.

Substitutional defects are those defects in which an impurity atom is incorporated at a regular atomic site in the crystal structure. This is neither a vacant site nor is the atom on an interstitial site. The atom is not supposed to be anywhere in the crystal, and is thus an impurity.

Antisite defects occur when atoms of different type exchange positions. For instance, let us assume that type A atoms sit on the corners of a cubic lattice, and type B atoms sit in the center of the cubes. If one cube has an A atom at its center, the atom is on a site usually occupied by a B atom, and is thus an antisite defect. This is neither a vacancy nor an interstitial, nor an impurity.

Dislocations are linear defects. They are lines around which some of the atoms of the crystal are misaligned. Their main role in the microstructure is to control the yield strength and subsequent plastic deformation of the crystalline solids at ordinary temperature. Dislocations can be observed using Transmission Electron Microscopy.

1.10 Growth of Lithium niobate crystals

LN is a synthetic crystal, which was first grown in the early 1960s using the Czochralski technique[67, 77]. Other growth techniques such as Verneuil, flux, Bridgman, Stepanov can also be used[67]. Growth is most easily initiated along the z-axis, but other orientations can also be grown by providing a seed of the correct orientation. The Czochralski method is used to successfully grow large and heavy crystals of LN[78].

The Czochralski growth method is widely used for industrial crystal growth, most notably that of Silicon. The pure compound of the material to be grown is melted in a crucible in the growth station. A seed crystal suspended from a rotating seed rod is then lowered into the furnace cavity, and the tip is touched into the melt. If the melt temperature is in the appropriate range, just slightly above the melting point of the material (1250°C for LN), growth of a crystal can be initiated by starting to slowly withdraw the seed rod. New crystal material will attach to the solid seed, cooled by conducting heat through the seed rod. As the growth progresses, the diameter of the growing crystal is controlled by adjusting the crucible temperature. Lowering the heating power will accelerate the crystallization and lead to a diameter increase, while increasing the power will act to decrease the crystal diameter. Figure 1-6 shows a schematic representation of the Czochralski growth process of LN[16].

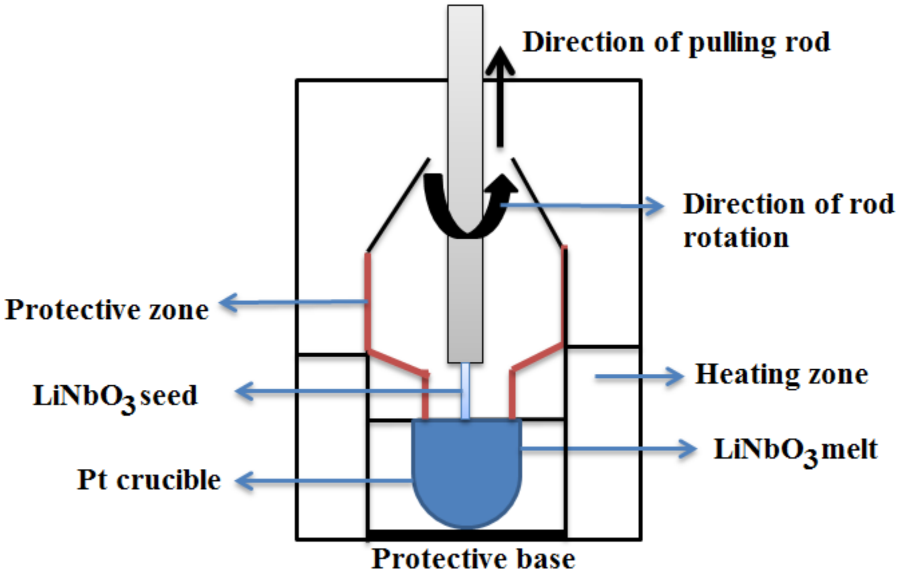

Figure 1-6. Schematic representation of the growth process of LN using the Czochralski method. LN crystals are usually pulled from melts contained in Platinum crucibles. The components of a Czochralski system are the crucible containing the melt, the heat generation with surrounding insulation (heater), seed pull and rotation mechanism[16].

The Czochralski process of LN crystal growth is usually divided into the following six phases[16].

a) Preparation of materials:

A Platinum crucible that contains the material of LN to be crystallized is placed inside the heater where a growth chamber is formed. The melt temperature is set to 1250 °C which is the melting point of LN, and the entire melt is kept in the liquid state. A crystal seed is attached to the lower end of a pulling rod and is lowered enough to be heated to a temperature that is close to the melt temperature, but not so low that it makes contact with the melt surface[16].

b) Seeding

The pulling rod is lowered to get the seed in contact with the melt surface. A phase change reaction at the solid-liquid interface occurs. The melt meets the seed, which is at a lower temperature. If the temperature of the melt is right, atoms from the liquid will adhere to the seed and crystallization will take place. Higher temperature causes the seed to melt off the pulling rod while lower temperature causes flashing-out; i.e. the melt freezes locally around the seed, and may even snap the seed off the pulling rod[16]. To avoid dislocations propagating from the seed into the growing crystal, seeds are typically cut from previously grown crystals with low dislocation densities[67].

c) Core growth

After the seed is successfully dipped, the pulling rod begins to rise. The proper solid-liquid interface is maintained and crystallization continues. The melt temperature is adjusted so that the crystal will grow out with gradual increase in diameter like a cone. At the same time the pulling rod keeps rotating at a proper speed to average out radial asymmetries[16]. Table 1.1 shows the pulling and rotation speeds, crystal diameters, melt composition and orientation. In this table, the data for crystals with large diameter is presented[19] . These crystals are of special interest for industrial production.

d) Main growth

Main growth starts when the crystal reaches the desired diameter. During the main growth, the diameter of the crystal should remain a constant, resulting in a cylindrical crystal. The cylindrical part of the crystal is the most utilized and so of most interest. Diameter control is the focus of the crystal growth control problem[16].

Table 1-2. Growth parameters of LN crystals in the Czochralski method[19]

Pulling speed (mm/hr)	Crystal diameter (mm)	Melt composition (mol% Li_2O)	Growth axes
2-3	100-125	48.6	Y
5	50-75	48.6	Y, Z
3-4	75	48.6 (Fe)	Z
3	83	48.6	Z

e) Separation of the crystal from the melt

After the necessary crystal length has been achieved, the crystal is separated from the melt by accelerated pulling. Tapering the crystal bottom to avoid heat shock is typically not necessary. An annealing stage follows to reduce the risk of cracking.

f) Cooling

The crystal is brought into a space of low thermal gradient at a temperature where dislocations move easily. The dislocations will adjust to lower the strain energy of the crystal. In highly strained crystals, dislocations typically will form grain boundaries. After completion of the annealing step, the crystal is slowly cooled to room temperature in order to avoid thermally induced cracking.

1.11 Observation of Acoustical Memory (AM) from Lithium niobate

Fundamental nonlinearity results from the fact that the interatomic potential function is not a parabola. LN appears to produce a nonclassical nonlinearity, which may arise from structural inhomogeneity of the crystal. This was observed as a non-exponential echo train and cannot be explained by nonparallelism of the sample surfaces[22].

LN demonstrates a physical effect called Acoustical Memory in which an acoustical tone burst is stored inside the crystal and reemitted at a later time of the order of 70 μs[21]. This phenomenon is dependent on frequency and temperature. Figure 1-8 shows the AM signal observed in bulk LN samples. The acoustical longitudinal modes propagated in the *[001]* axis, which is the piezoelectrically active direction. The AM was observed in the frequency (*f*) range between 16 MHz to 26 MHz. The size of the memory centers is calculated in Ref. 21 as $L \approx \frac{V}{2f}$. With a velocity V along the *[001]* direction of 7.3 x 10^3 m/s, this gives an approximate dimension ranging between 140 to 230 μm.

The AM effect was also investigated in the frequency range between 2.5 MHz to 10 MHz[19]. It was found that there exists a hysteresis relationship between the memory signal and the driving force. This reflects the nonclassical nonlinearity. The amplitude hysteresis of the first and second harmonics of the direct wave further reflects this kind of characteristic. Furthermore, the amplitude of the acoustical memory signal at 2.5 MHz increases with increasing temperature, while it decreases with increasing temperature at 25.9 MHz.

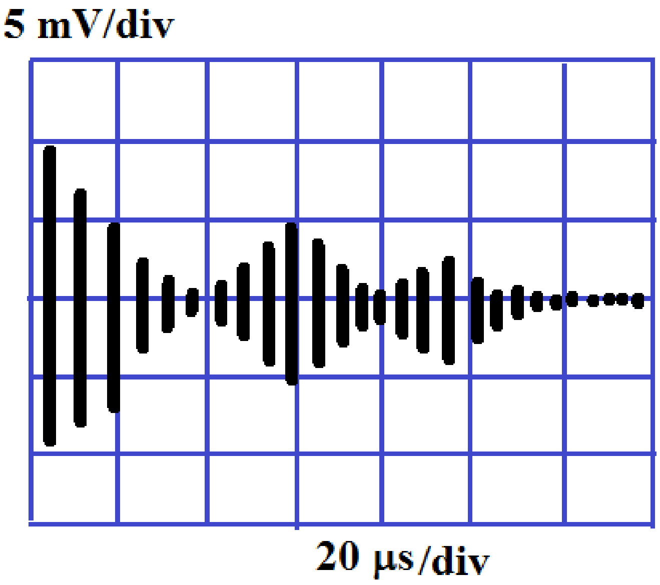

Figure 1-7. Schematic sketch of typical acoustical memory signal observed from LN at room temperature. The memory signals are the after signals that appear after the main burst has died down.

When ultrasonic waves pass through LN samples, a portion of the sound energy will shift to substructures of superlattices and anomalous regions. This is due to the presence of defects, which form subsources of ultrasonic vibration. After a nonlinear interaction between the primary sound source and subsource, the sound energy is retransmitted and a memory signal appears. On the other hand, acoustical stress leads to a redistribution of ferroelectric domains. The domain walls can be placed in motion by the piezoelectrically active acoustical wave. The vibration of ferroelectric domains and defects, which originates from the piezoelectric effect, still remains after ultrasonic waves have passed through the sample. This kind of phenomenon occurs only in crystals because other media do not have domain structures. The memory signal is closely related to the crystals microstructure because the memory signal is also quite different in different directions. Therefore, the memory signal can indicate the micro characteristics of the crystal[19].

Nonclassical nonlinearity was observed in periodically poled Lithium tantalite (PPLT)[79] as shown in figure 1-8. The oscillograms for the radio frequency burst propagation consisted of secondary vibrations denoted by S1, S2 and S3. The S signals follow the main bursts A1, A2 and A3. The S signals were not observed from a single domain crystal. This led to the conclusion that the inter-domain walls are responsible for nonclassical nonlinearity in PPLT.

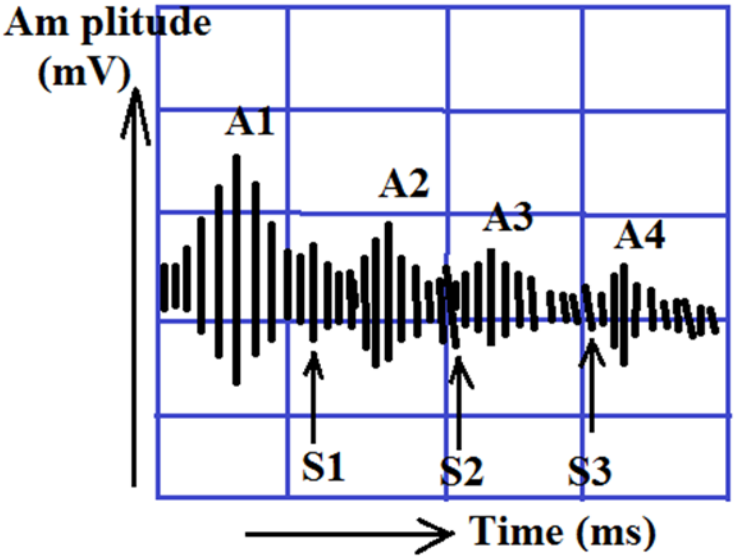

Figure 1-8. Sketch of acoustical wave propagation in piezoelectrics, showing the presence of secondary signals (S1, S2 and S3) in addition to the main burst (A1, A2 and A3).

1.12 Defects and Electrical Conduction in Lithium niobate

The electrical conductivity of LN at room temperature was found to be about 10^{-18} (mΩ cm)$^{-1}$ [80] . The charge transport obeys an Arrhenius-type dependence on the temperature. The conductivity is given by[81, 82]

$$\sigma = \sigma_0 \exp(-\frac{E_a}{k_B T}) \tag{1.36}$$

Where E_a is the activation energy and $\sigma_0 = en\mu_0$, where n is the ion density, μ_0 is the ion mobility and *e* is the elementary charge. At room temperature, E_a lies in the range of 0.1 eV to 0.49 eV[81] . The rather low value of σ_0 makes it very difficult to measure the DC (direct current) conductivity at room temperature.

The mechanism of electrical conduction at room temperature involves two defects in LN, the F-center[82] and the small polarons $\mathrm{Nb_{Li}}^{4+}$ [81, 82]. The F-center is a vacant cationic site, (whose location is represented by position vector $\boldsymbol{r_1}$), which traps an electron (e^-). Under the influence of an external electric field, the F-center moves to a new location $\boldsymbol{r_2}$. This may be represented by:

$$[F_1^+(\boldsymbol{r_1}) + e^-(\boldsymbol{r}_1)] \rightarrow [F_2^+(\boldsymbol{r_2}) + e^-(\boldsymbol{r}_2)] \tag{1.37}$$

This means that under an external electric field, it is the electron that moves from site $\boldsymbol{r_1}$ to site $\boldsymbol{r_2}$. This may be represented by:

$$e^-(\boldsymbol{r_1}) \rightarrow e^-(\boldsymbol{r_2}) \tag{1.38}$$

This is one of the mechanisms of electrical conduction in LN which is schematically represented in Figure 1-9.

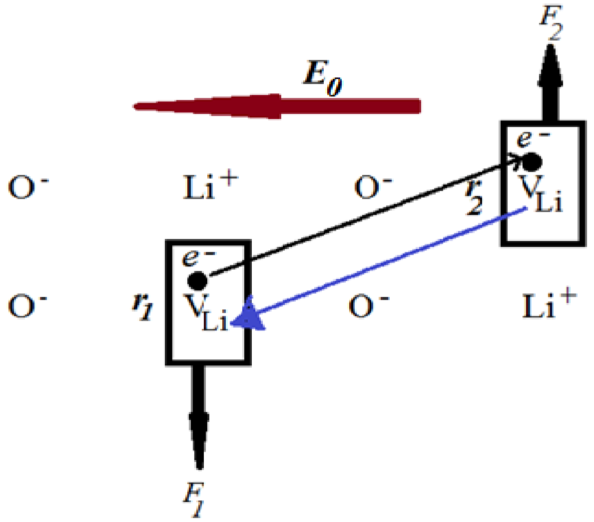

Figure 1-9. The figure shows charged ions O^-, Li^+ and the Li vacancy V_{Li} in the crystal lattice. An electron e^- is trapped at the site of a lithium vacancy with position vector $\boldsymbol{r_1}$. This constitutes the F-center (F_1) at position $\boldsymbol{r_1}$. Under the influence of an external electric field $\boldsymbol{E_0}$, the electron at $\boldsymbol{r_1}$ moves to the site of another Lithium vacancy at $\boldsymbol{r_2}$. This constitutes a new F-center (F_2) at the position $\boldsymbol{r_2}$. A Lithium vacancy is left behind at the site $\boldsymbol{r_1}$. Thus the Li vacancy V_{Li} moves in a direction which is opposite to the motion of the electron. The motion of the Li vacancy is responsible for electrical conduction in Lithium niobate.

The second mechanism is by the hopping of small polarons (Nb_{Li}^{4+}). The polaronic effect is observed when Nb_{Li}^{5+} at a site (for instance $\boldsymbol{r_3}$) captures an electron (from a site say $\boldsymbol{r_4}$) and becomes Nb_{Li}^{4+}[83]. This may be shown as:

$$Nb_{Li}^{5+}(\boldsymbol{r}_3) + e^-(\boldsymbol{r}_4) \rightarrow Nb_{Li}^{4+}(\boldsymbol{r}_3) \tag{1.39}$$

Thus the motion of the electron may be shown as:

$$e^{-}(\boldsymbol{r}_4) \rightarrow e^{-}(\boldsymbol{r}_3) \tag{1.40}$$

The electronic charge is strongly localized around the Nb^{4+} ion that distorts the oxygen octahedron around it. Under the influence of an externally applied electric field, this change in electronic configuration moves from site to site. This mechanism contributes to the electrical conduction in LN.

CHAPTER II

SAMPLES AND EXPERIMENTAL PROCEDURE

In this chapter, the samples and experimental techniques used to measure the spectra of PL from LN and their effect on acousto-electric properties are discussed. The samples used are z-cut and y-cut single wafers, plates and bulk single crystals, and a PPLN crystal. The experimental procedures employed may be broadly classified as optical measurements to observe PL spectra from LN and electrical measurements to determine the effet on acousto-electric properties.

2.1 The Structure of Single Crystal Lithium niobate

Lithium niobate does not occur naturally, all crystals of lithium niobate are artificially grown. Its crystal structure and physical properties received intense study at Bell Laboatories. Of the 32 crystal classes, 20 are seen to produce a spontaneous polarization when subjected to an external stress and these are known as the piezoelectric classes. Of the 20 piezoelectric classes, 10 are characterized by the fact that they have at least one unique polar axis which retains a spontaneous polarization without an external electric field or applied stress and these are known as the polar classes. Within the 10 classes of polar crystals some crystals reverse the direction of spontaneous polarization under the application of an electric field. Upon removal of the electric field, they do not go back to their original configuration. This property cannot be distinguished from the symmetry of the crystal structure alone and classification must so be done experimentally. These crystals are known as the ferroelectrics and it is within this group of crystals that we find LN[80].

The crystal structure of LN is trigonal, meaning that it has a three-fold rotational symmetry about the polar axis. It also possesses a mirror plane parallel to the axis of rotation which places it in the crystal class 3m, in the Hermann-Mauguin notation. The oxygen atoms form octahedra around the cations and are arraged along the polar axis. The polar axis is also the direction of the optic axis for LN. Therefore, all defects that are present in the direction of the polar axis, may influence optical properties of LN. The polar axis is the z-axis in LN, which also happens to be the piezoelectrically active direction. As a result, defects present along the polar axis influence acousto-electroc properties of LN. The oxygen tetrahedral interstices remain empty whilst the oxygen octahedra are filled with either lithium or niobium cations or vacancies along the positive polar direction. In commercially available doped LN, the larger atoms of point defects (such as Fe^+) has a higher chance of settling in the interstitial locations or at the positions of the niobium vacancies. At temperatures above the Curie temperature (*Tc*), the crystal is paraelectric with the niobium cations located in the geometric centers of their oxygen octahedra and the lithium cations at a position of ±0.037 nm on either side of the oxygen plane with equal probability[80]. As the crystal cools through the Curie temperature the phase transition from paraelectric to ferroelectric takes place. This transition is of second order since no abrupt change is seen at *Tc*. The niobium cations move away from the geometric center of the oxygen octahedra and the lithium cations arrange co-operatively to the same side of the oxygen plane. Long range forces control the ordering of the movement from the paraelectric positions such that dipole moments of the individual unit cells align and a net spontaneous polarization is obtained. The position of the cations within the oxygen octahedra distorts the octahedra such that the oxygen-

oxygen distance in the planes nearest the cations is less than that of the plane opposite[80]. At room temperature the niobium cation, then, has a larger effect upon the oxygen octahedra than lithium. The distortion of the oxygen octahedron by niobium is responsible for the formation of crystal defects. The heavy niobium atom knocks of a lithium atom and occupies its position in the lattice. This results in the formation of an antisite defect. The region around the antisite defect is locally stressed and the oxygen octahedron is distorted. On the application of an external electric field, this distortion moves along the direction of the field creating a polaron. The presence of a heavy atom including the host niobium and charged point defects polarizes the surrounding oxygen atoms. The additional polarization is responsible for increases electromechanical efficiency of LN which is investigated in detail in Chapter 4.

LN is a ferroelectric material consisting of domains and domain walls. An electric field is usually applied to fabricate a single crystal. The application of the electric field displaces the lithium and niobium atoms. The movement of these host atoms create new vacancies and interstitial defects in the material. Electrons from neighboring atoms get trapped in the vacancies resulting in the formation of the F-center. The formation of these conductive defects are useful in applications that require LN to conduct electricity. However, the presence of these point defects also show up as spurious nonlinear signals which is undesired in practical aplications including transducers. It is impossible to create a defect free crystal as the presence of defects minimizes the internal energy of the crystal, thereby leading to stability. Commercially available LN has several additional impurities doped into crystal to enhance applications in electro-optic devices. These dopants are usually heavy transition metals. In fact, Lithium tantalite is often doped with the radioactive metal Thorium to enhance its usage in pyroelectric nuclear fusion, as discussed in section 3.7. Figure 2-1 shows the crystal structure of LN with the presence of a point defect.

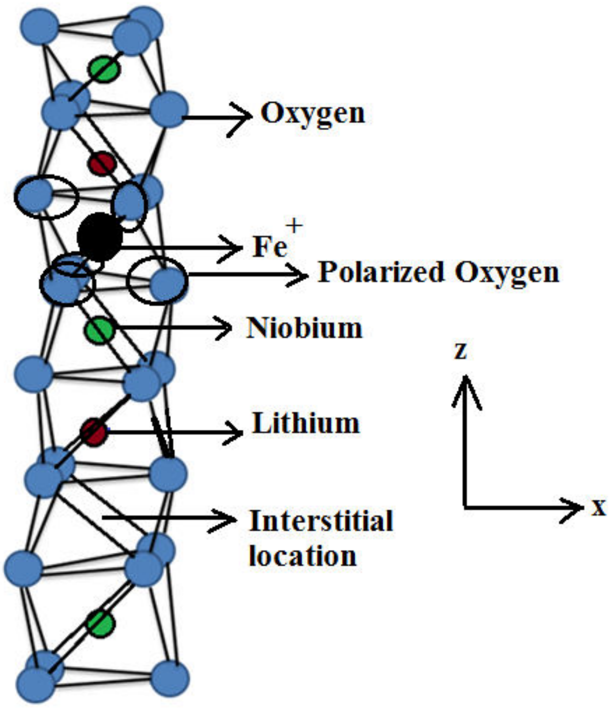

Figure 2-1. The crystal structure of LN showing host atoms Li, Nb and O in the zx-direction. The presence of a charged dopant Fe^+ polarizes the O atoms around it. More the presence of heavy charged point defects, more is the polarization of O thereby leading to increased electromechanical efficiency. This will be investigated in Chapter 4.

LN has been recognized as one of the most versatile materias for application in modern optics in a broad range extending from the near UV to the far IR. The combination of ferro-, pyro-, piezoelectric properties with large electro optic , acousto-optic and photoeleatic coefficients as well as strong photorefractive and photovoltaic effects made LN one of the most studies materials in the last 50 years[18]. The crystals were grown by the Czochralski method by the end of the 1980s. High quality congruent single crystals were grown by this method.

There are numerous spectroscopic methods for the characteriztion of the composition and properties of LN. Measurement of the UV absorption edge is a simple, fast and accurate method to determine the crystal composition, especially near to the stoichiometric composition. The band edge is defined as the wavelength where the absorption coefficient α equals 20 cm^{-1}. Weak absorption in band tail is related to defetcs like antisite Nb_{Li} and possibly lithium vacancies V_{Li+}[18]. Both types of defects are present in nonstoichiometric crystals, their charge compensating each other . They simultaneously disappear at the stoichiometric composition.

The IR absorption of the hydroxyl (OH^-) ions also yield valuable information. LN crystals grown in air contains hydroxyl ions incorporated during the growth process. These ions occupy regular oxygen sites in the lattice with possible charhe compensators in their surroundings. The stretching vibration of the OH^- ion can be detected in the IR spectral range at about 3484 cm^{-1} (2.87 μm)[18].

An extended X-ray absorption fine structure (EXAFS) spectroscopy highlights evident changes in the local structure around iron[83]. This is due to the presence of small polarons. Fe^{3+} captures an electron and becomes Fe^{2+}, a small bound polaron. The electronic charge is strongly localized around the Fe ion and closely resembles the atomic Fe d_z^2 orbitals, suggesting a scarce hybridiation of such states. On formation of Fe_{Li} substitutionals, the Fe ion is shifted along the crystal axis by 0.09 Angstrom, with respect to the substitutes Li. Thus a structural change occurs along the crystal symmetry axis. This behaviour is also similar to Nb_{Li} substitutionals. Figure 2-2 shows microstructure of ferroelectric materials like LN.

Raman spectroscopy is a useful and efficient tool to probe the local structural properties of LN and derived materials and devices[84].This is possible because all first order Raman lines in LN are assigned to transverse or longitudinal optical phonons and their associated ionic motions. Any change due to the incorporation of defects can thus be detected by a modification in the position, width, and / or intensity of Raman lines.

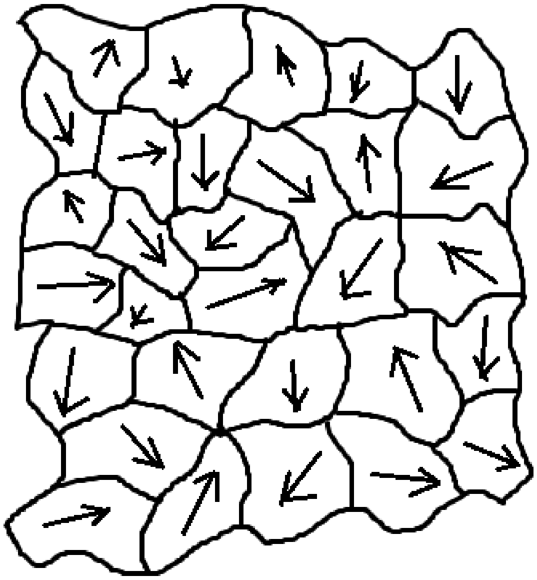

Figure 2-2. Schematic sketch of the microstructure of a ferroelectric material. The arrows represent the ferroelectric domains, which are separated by ferroelectric domain walls. For single crystal fabrication, an external electric field is applied. The microscopic ferroelectric domains align in the direction of the electric field. But all defects do not disappear, these defects manifest themselves as nonclassical nonlinear signals in LN.

2.2 Periodically Poled Lithium niobate (PPLN)

Therapeutic ultrasound is an emerging and growing area of fundamental and applied research including various mediacal applications. Recent developments include rigorous research in High Intensity Focus Ultrasound[85, 86] and its clinical aspects[87] including ultrasound applications for drug delivery[88], medical ultrasonic transducers for high frequency operation[89], and others. Research on periodically poled ultrasound transducers is connected to ceramic materials with inversely poled ferroelectric domains[90, 91], their efficiency of acousto-electric transduction in bulk[92] and two-dimensional acoustic superlattices[93].

Usually periodically poled domains are fabricated in bulk crystals of the type of $LiNbO_3$, $LiTaO_3$, $BaTiO_3$, Lead Zirconate Titanate (PZT), and others, and in modern wafers of $LiNbO_3$

and $LiTaO_3$. PPLN is widely used in nonlinear optical applications[94-97] such as optical resonators[98], second harmonic generation[99] and others. It is used in telecommunication applications[100] such as radio filters[101] and others. Interest in acoustic superlattices has grown because of their potential applications as ultrasonic transducers[102, 103]. Periodically poled lithium niobate (PPLN) is an artificially engineered material in which adjacent domains are inverted using electric poling techniques. One of the limitations of this method id the effect of broadening of domains outside the electrodes, which hampers creation of domain structures with submicron period[104]. In order to fix this problem, periodic poling by electron beam patterning was developed[94, 104-107]. However irradiation of the free crystal surface conductivity led to delocalization of the space charge by inhomogeneous spreading of electrons thus limiting the structure period[104]. Recently the electron beam poling technique has been modified by covering the irradiated surface by a thin photo- or electron beam resistant dielectric layer, with high concentration of charge carrier traps [94, 104, 108, 109]. The layer has led to charge localization and improvement of the domain pattern quality. Domain inversion switches the sign of all odd rank tensors, in particular the piezoelectric tensor e_{ijk}, from one domain to the next. The sign of even rank tensors such as permittivity ε_{ij} or elastic constant c_{ijkl} remain unchanged upon domain inversion.

2.3 Samples used for the Experiment

Single crystal and periodically poled LN samples were used for optical and electrical measurements. The single crystal samples were of the bulk, wafer and plate type. The crystals were grown by the Czochralski method and were of different cuts. The bulk crystals were Z-cut. They were of two types: polarized (LNO-P) and unpolarized (LNO-U). The polarized crystal was cylindrical in shape while the unpolarized sample was a semi-cylinder. Fig 2-3 schematically shows the bulk samples.

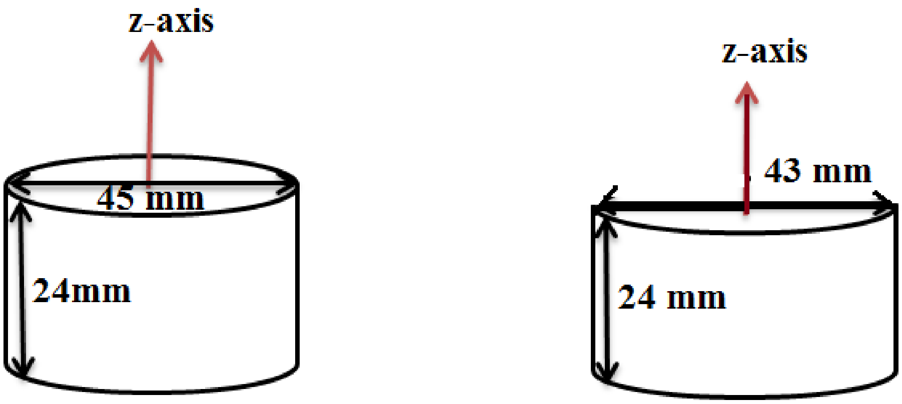

(a) (b)

Figure 2-3. Schematic representation of the bulk samples: (a) LNO-P, (b) LNO-U.

The process of rotation and pulling by the Czochralski method create macroscopic grooves or swirls on the outer surface of the LN cylinders. The thickness of the swirls depends on the pulling rate while the crystal is being grown. The swirl defects are caused by the condensation of excess thermal point defects from the melt. Swirl defects have been observed in Czochralski grown Silicon[110]. However the outer swirl defects show up in the PL measurements and suppresses the contribution of the native point defects. In order to include the native point defects, a small portion of the bulk crystals was polished and PL spectra was recorded from this flat surface. Figure 2-4 shows the swirl defects and polished part in bulk LN crystal. In order to record readings from the inner points of the crystal, data was recorded from the unpolished diametric plane of LNO-U. The half cylinders are obtained by cleaving an unpolarized bulk cylinder into two halves. Figure 2-5 shows the natural structure of the domains on the diametric plane.

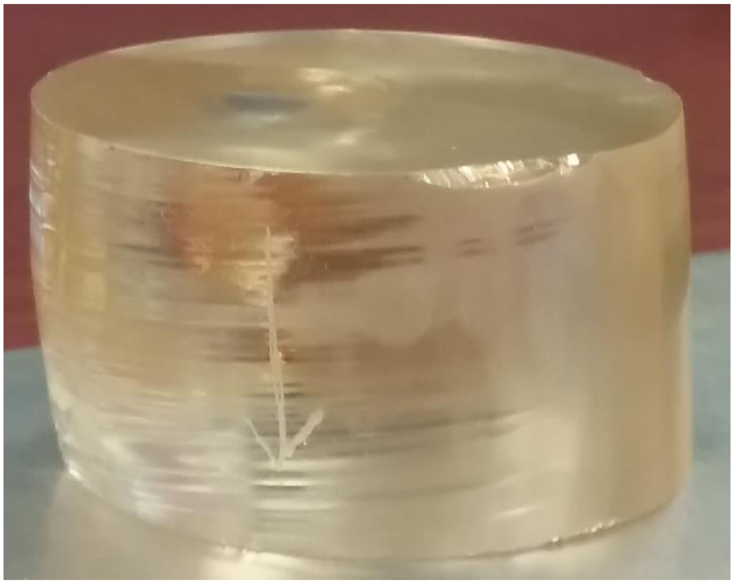

Figure 2-4. Macroscopic swirl defects on the outer face of LNO-P crystal. Polishing is performed towards the right to flatten out the grooves. The arrow shows the direction of the +z-axis.

Figure 2-5. Macroscopic structure of domains on the cleaved diametric plane of LNO-U bulk crystal.

Other than bulk crystals, single crystals of different cuts in the form of wafers and plates were studied. The ZX-cut wafer was optically polished and purchased from MTI Corporation, Richmond, California. The second wafer was y-cut with metal contacts deposited partly on both faces of the sample. This sample was grown in Europe. In addition a YZ-cut plate was used which was optically polished on one side. This ample was purchased from MTI Corporation. Figure 2-6 shows a schematic diagram of the wafer and plate samples.

The geometrical structure of the ferroelectric phononic supperlattice sample is shown in figure 2-7. The ZX-cut PPLN plate (ZX-PPLN) had 88 domains (or 44 domain pairs) with neighboring domains poled in the opposite direction. Domains of + type are polarized upward as shown is figure 2-7 (a), while domains of – type are polarized downward. The length of all domains is equal to 0.45 mm. Therefore the periodicity of the structure is 0.90 mm. The PPLN structure is surrounded by a protecting zone as shown in figure 2-7 (b).

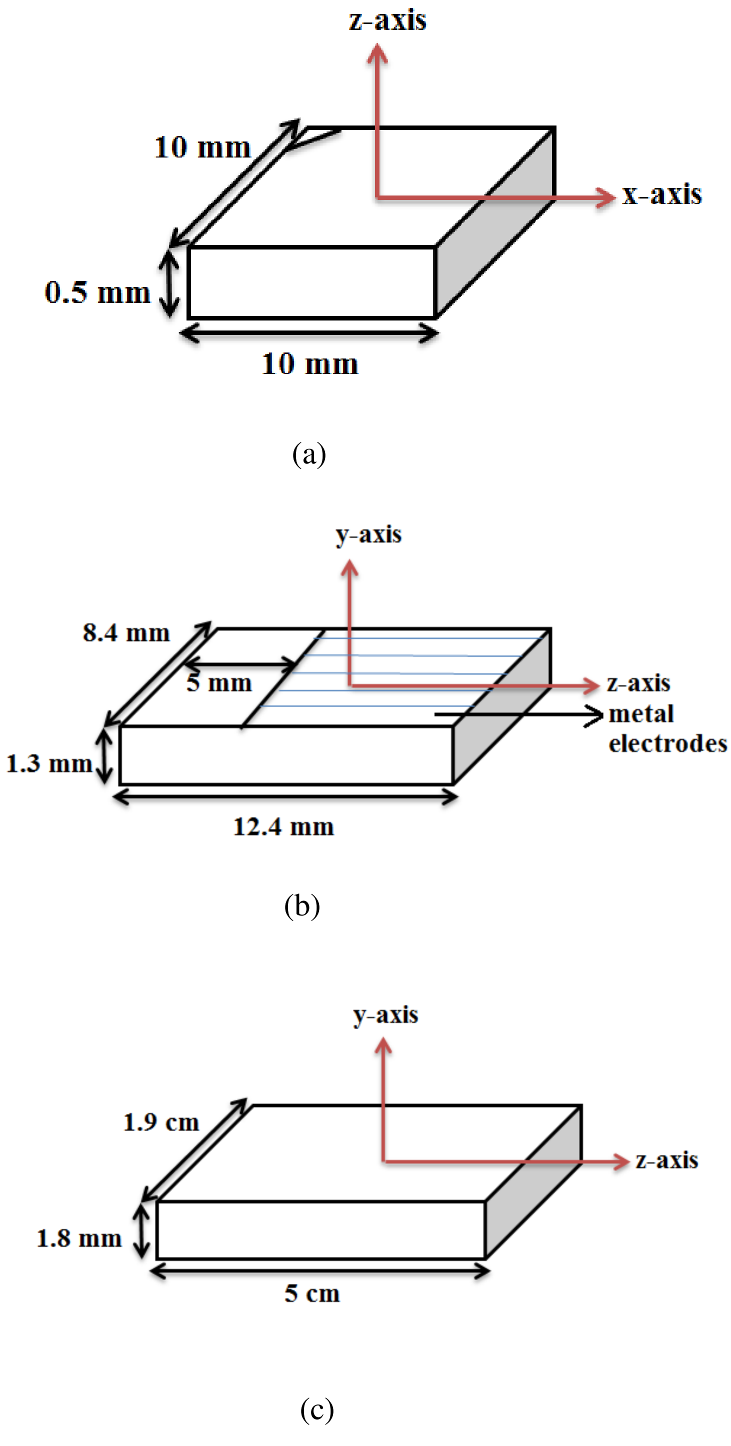

Figure 2-6. The wafers and plate sample that were used. (a) ZX-LNO-Wafer-1, (b) YZ-LNO-Wafer-2, and (c) YZ-LNO-Plate

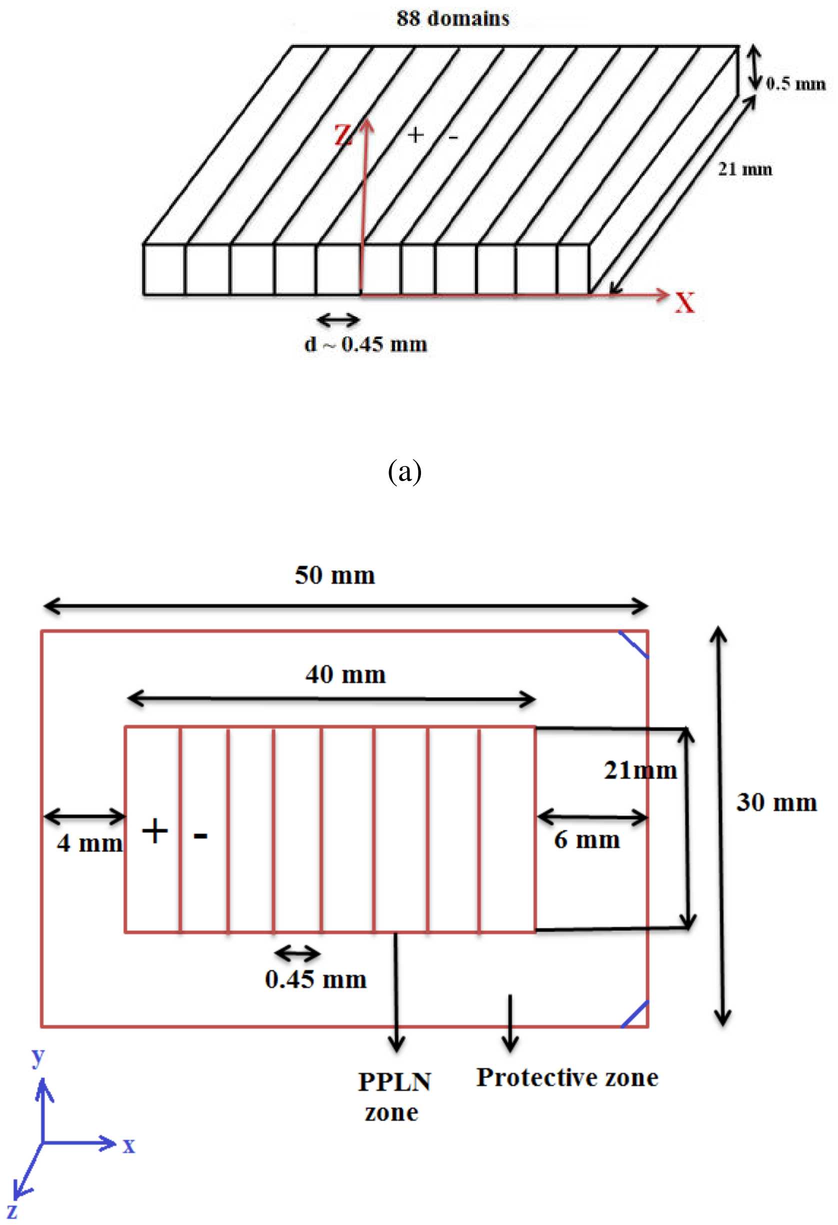

(a)

(b)

Figure 2-7. (a) PPLN structure consisting of oppositely poled domains, (b) ZX-PPLN structure containing PPLN zone and protective zone. The protective zone protects the crystal frm damage or breaking.

2.4 Experimental Method to Observe Spectra of Photoluminescence from Lithium niobate

The experimental setup is shown in Figure 2-8. The photoluminescence was excited by a Xenon arc lamp. The output power of the lamp was set to 60 Watt during the experiment to obtain a steady and bright beam of light. The light from the lamp falls on slit S0, and is then incident on an excitation monochromator M1. The wavelength of the excitation monochromator is fixed to 310 nm during the experiment. It is observed that the peaks due to the defects are sharpest at this excitation. Since the electronic transition takes place between quantum energy levels, the wavelength of 310 nm provides the best excitation for the transitions to occur. The light from the excitation monochromator M1 passes through the slit S1 and then falls on the sample. The reflected light from the sample passes through a slit S2 into an emission monochromator M2. The light from the emission monochromator passes into a Photo Multiplier Tube P.M.T which counts the number of photons emitted per second. During the experiment , slits widths were maintained between 0.5 nm and 1.2 nm, for the different LN samples. It was observed that diffraction was minimum at these slit widths.

All samples were fixed to sample holders that were specially made at the machine shop in the Department of Physics and Astronomy. The samples were then mounted in the sample compartment of the spectrofluorometer shown in Figure 2-8. The mounting of the samples is shown in Figure 2-9. The sample holders and fixed to the flat base of a movable screw. The screw was rotated in steps of tens of microns so that spectra is recorded from very closely spaced points on the sample.

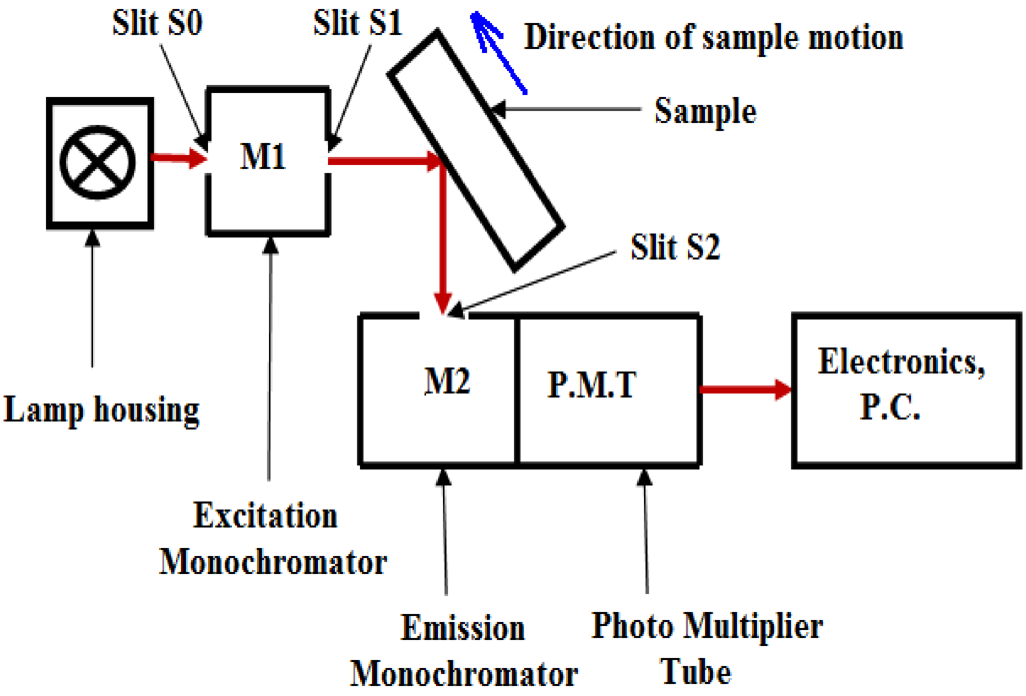

Figure 2-8. Experimental setup to obseve spectra of PL from LN samples. The PL spectra are recorded with the help of a Quantamaster^{TM} 400 Spectrofluorometer manufactured by Photon Technology International.

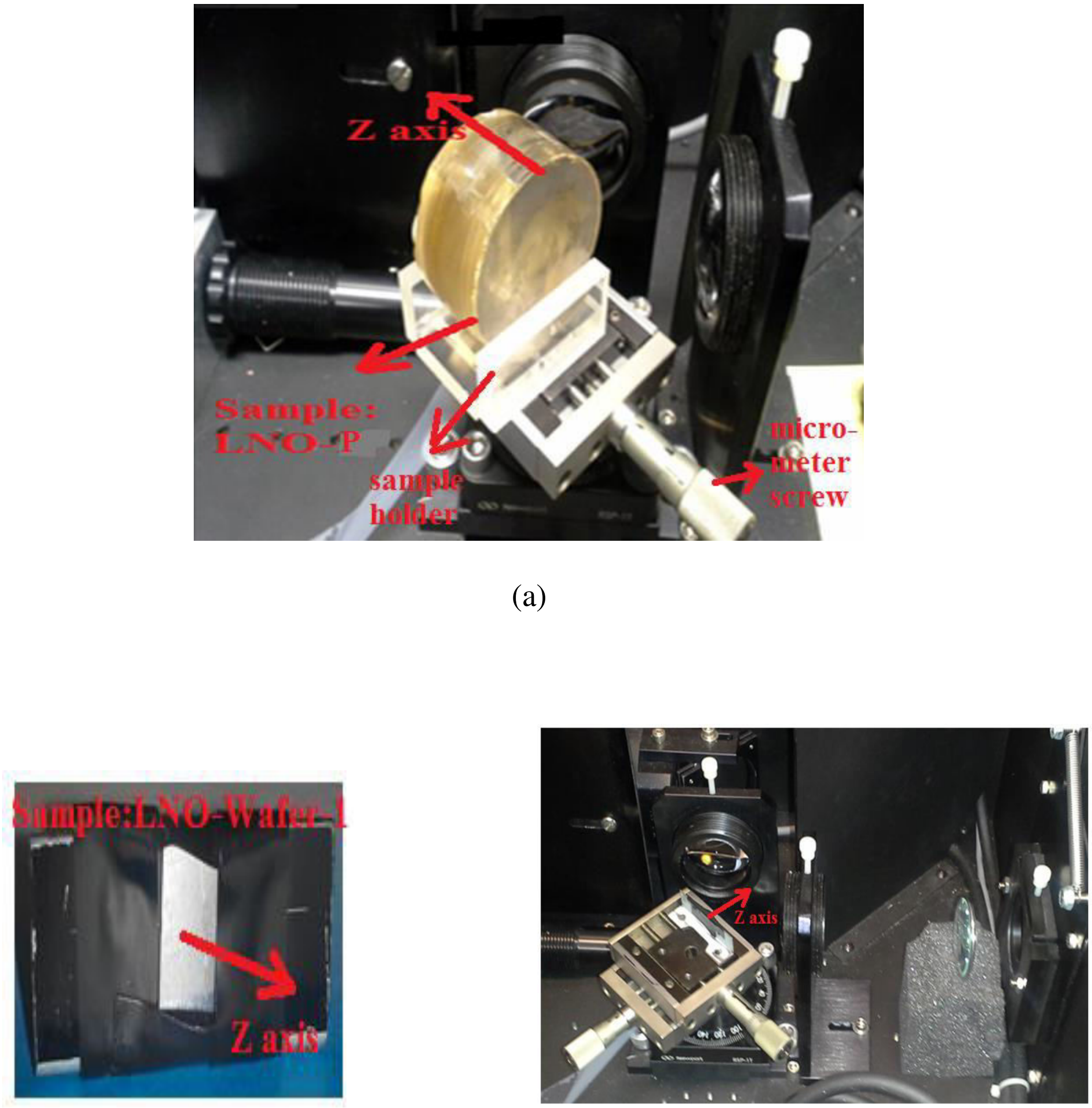

(a)

(b)

(c)

Figure 2-9. Samples mounted on customized sample holders and fixed to the flat base of a movable screw: (a) Mounting of the polarized bulk crystal LNO-P. The crystal is moved parallel to the z-axis, (b) sample holder for the ZX-LNO-Wafer-1, (c) mounting of ZX-LNO-Wafer-1. The sample is moved perpendicular to the z-axis.

The samples were illuminated with green light in order to adjust the position in the sample compartment. This is because green light is the easiest to detect. The width of the slits S0 and S1 were adjusted until a sharp image of the slit was formed on the sample. The width of the image formed on the sample is of the order of tens of microns and is measured with a micrometer screw. There was a surrounding region of light of lesser brightness around the image of the slit. The slit widths were adjusted to minimize the brightness of this surrounding region. But it could not be completely eliminated. Figure 2-10 shows the light spot on the LN sample. The position of the sample should be adjusted in a way so that the output light forms a sharp image on the slit S2 of the emission monochromator. It is at this position that the peaks of the PL spectra are well resolved.

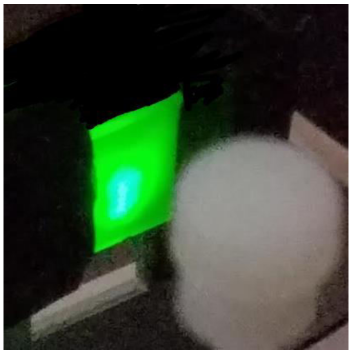

Figure 2-10. Image of the slit illuminated by green light on the face of the sample ZX-LNO-Wafer 1. The sample holder is covered with black non-photoluminescent paper on all sides. This prevents additional peaks corresponding to the sample holder to show up in the PL spectra.

In order to calibrate the instrument, the distribution of the noble gas Ne impurity in the sample ZX-LNO-Wafer-1 was measured. This sample was chosen since it was optically polished on both sides. It can be observed from Figure 2-11 that the distribution of Ne lies within the error in counts. The spread in PL intensity is low, ±1.9% from the average PL intensity (I_{avg}(Ne)), as shown in Figure 2-11. This is expected as Ne is a noble gas, and thus its distribution in the crystal should not vary a lot. This proves that the instrument for observing PL spectra from LN is calibrated.

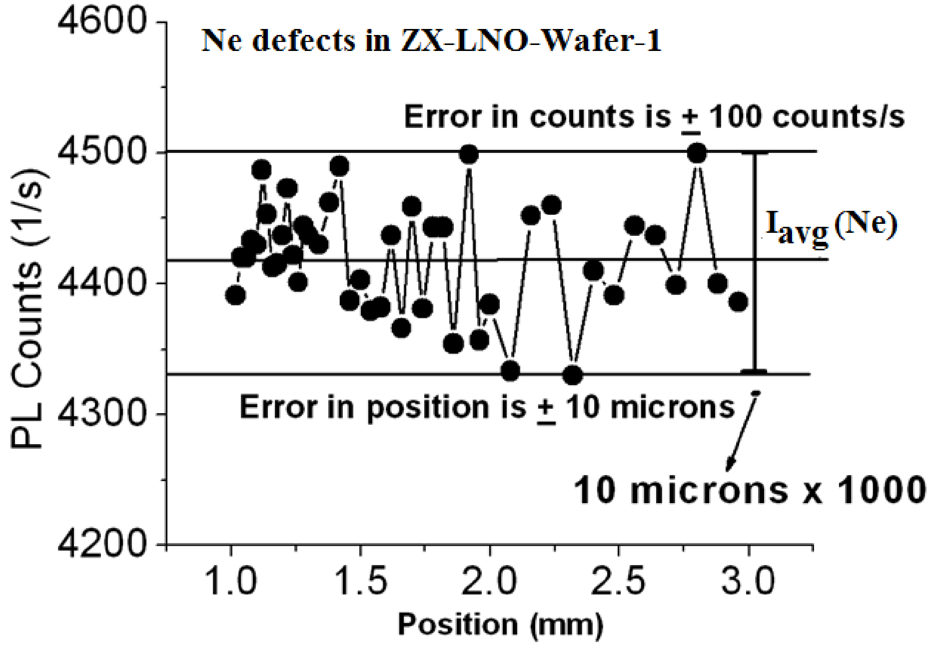

Figure 2-11. Distribution of Ne defects in ZX-LNO-Wafer-1. The error in PL counts which is ±100 counts/s is obtained by running the instrument with all slits closed. The error in position comes from the least count of the micrometer screw.

2.5 Experimental Setup to Observe Spectra of Polarized Photoluminescence from Lithium niobate

The linear polarization of luminescence light allows conclusions on the symmetry of defects in different materials. The polarization dependent PL allows determination of the symmetry of the defects relative to the optic axis (*c*) of the crystal[111]. Polarization depepndent PL has been applied for the analysis of symmetry in molecules or color centers. In semiconductors it has been used for the analysis of the band structure. In materials with non-cubic symmetry like chalcopyrites, the linear polarization of luminescence light allowed to identify three shallow acceptor levels[111]. Thus investigation of the polarized PL light from LN would be important to draw conclusions on the symmetry of the impurities in the material.

A polarizer was inserted in front of the slit S2 in the sample compartment. The experimental setup is shown in Figure 2-12. The polarizer had two settings 1) when the electric field vector $\overrightarrow{\boldsymbol{E}_{PL}}$ of the incident was parallel to the optic axis *c*, and 2) when $\overrightarrow{\boldsymbol{E}_{\boldsymbol{PL}}}$ is perpendicular to *c*.

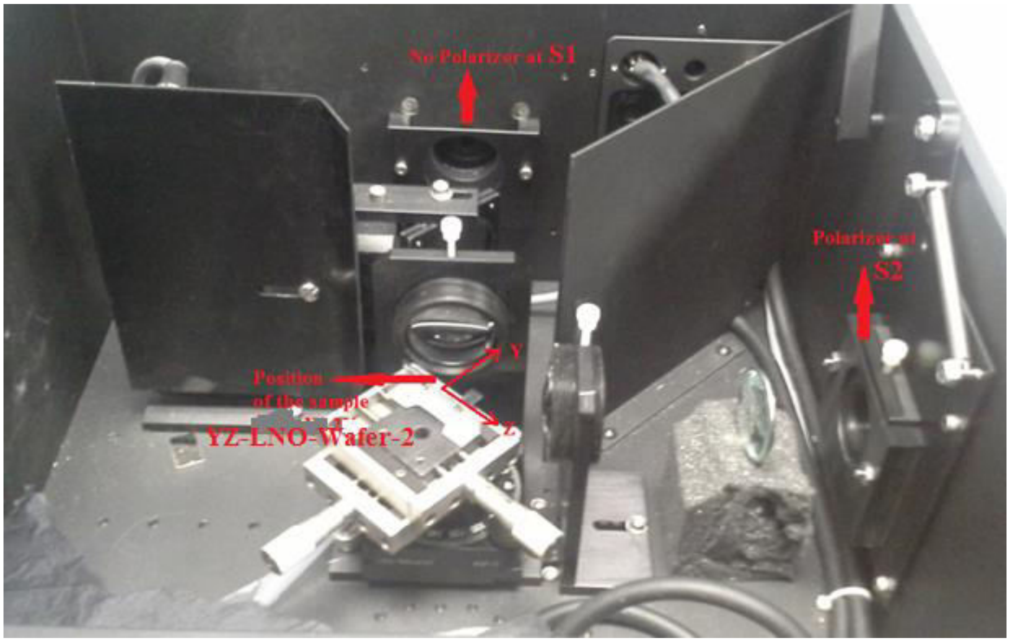

Figure 2-12. Experimental setup to observe polarized spectra of PL from LN. The polarizer is mounted at S2, befor the emission monochromator. No polarizer present at S1. This ensures that the light incident on the sample is unpolarized, but the luminescence light is polarized. The sample shown in the figure is YZ-LNO-Wafer-2.

2.6 Experimental Method for Observing Spectra of Optical Transmission from Lithium niobate

The apparatus used to observe transmission spectrum from LN was a Perkin Elmer Lambda 18 Ultraviolet/Visible Spectrometer. The operating wavelength was in the range 300 nm to 900 nm. The wavelength resolution used was 1 nm. The samples were optically polished and mounted on sample holders before making measurements from them. The experimental setup is shown schematically in Figure 2-13. The instrument has two arms, in one arm the optical transmission of the sample is measured. The other arm is used as the reference. A drawback of the instrument is that it switches lamps at 319.2 nm which might lead to different measurement sensitivities in different spectral ranges. The instruments used to observe the transmission spectra were the wafer ZX-LNO-Wafer-1 and the bulk samples LNO-P and LNO-U.

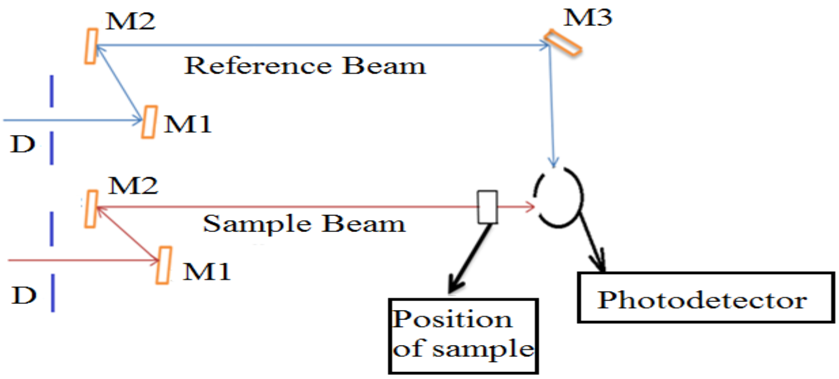

Figure 2-13. Experimental setup to observe transmission spectra from LN. The software used to control the settings of the instrument was UV Win Lab. The instrument uses two lamps, a deuterium lamp in the ultraviolet wavelength range, and a halogen lamp in the visible wavelength range. The diaphragm D controls the diameter of the beam of light, and was set to 4 mm during the experiment. The mirrors M1, M2 and M3 reflect the beam before it enters the photodetector.

2.7 Experimental Method to Measure Electromechanical Transformation from Lithium niobate

Figure 2.14 (a) shows a schematic diagram to experimentally investigate the electromechanical transformation (EMT) from LN. The EMT is estimated by reading an electric potential (V) generated while applying a mechanical force to a local point. The applied mechanical force is kept constant while rmeasuring the voltage from different points of the sample. The charged defects are sensitive to local electric polarization, so it is expected that they will influence the EMT at a local point in the crystal. The mechanical force is applied with a hammer, which is basically a hard plastic stick with the tip sharpened. The size of the tip is less than 10 μm and is measured by a microscope manufactured by The Precision Tool and Instrument Co. Ltd. The hammer fell freely under gravity, the tip travelled a distance (d) before striking the face of the LN crystal. Figure 2.14 (b) shows that the plot of the voltage V versus d. The experiment was performed with d equals to 10 mm, where the relationship between V and d is linear. A mechanical guide was used to ensure that the hammer was positioned vertically before release. The electric potential V generated is an estimate of the EMT. The micrometer screw is rotated in steps of a hundred micron for YZ-LNO-Plate and tens of microns for ZX-LNO-Wafer-1, to change the point of impact of the hammer on the crystal. This helps to investigate the EMT from different points of the crystal.

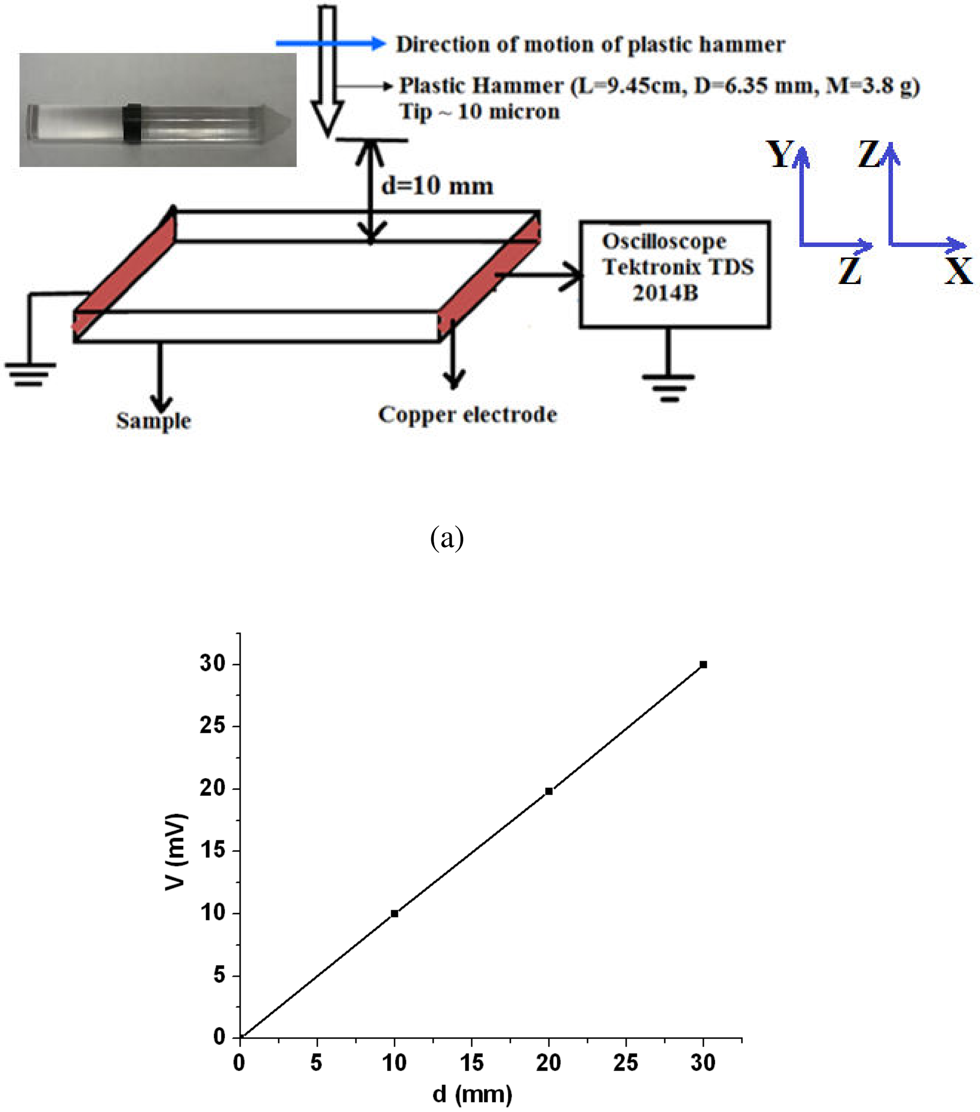

(a)

(b)

Figure 2-14.(a) Experimental setup to observe electromechanical transformation from LN. The inset to the left shows a picture of the plastic hammer. L, D and M represent the length, diameter and mass of the hammer respectively. The arrows to the right represent the orientation of the sample YZ-LNO-Plate and ZX-LNO-Wafer-1, (b) plot of the voltage (V) generated versus the distance (d) through which the tip of the hammer falls before it makes an impact with the sample.

In order to calibrate the instrument, a glass plate of dimensions (76 mm x 25 mm x 1 mm) was used instead of LN. Since glass is an amorphous material, it is not piezoelectric. So it is expected that the impact between the hammer and glass will not generate a signal on the screen of the oscilloscope. The result is shown in figure 2.15.

M Pos: 60.00µs

TRIGGER

Type Edge

Source CH2

Slope Rising

Mode Normal

Coupling AC

CH1 20.0mV CH2 10.0mV M 250µs CH2 ∕ -16.0mV

Figure 2.15. Oscillogram showing impact of the hammer with glass. No signal is generated. Data is recorded in steps of 0.5 mm for a total length of 5 mm. The signal does not change. This is because glass is not piezoelectric.

2.8 Experimental Method to Measure Radio-Frequency (r-f) Admittance of Lithium niobate

The experimental setup to measure the r-f admittance is shown in Figure 2-16. The admittance Y is proportional to V_{PP}^{out}/V_{PP}^{in} , where V_{PP}^{out} is the peak to peak output voltage and V_{PP}^{in} is the peak to peak input voltage. V_{PP}^{in} is a swept sine function fixed at 15 V throughout the experiment. The sample used for this investigation was YZ-LNO-Plate. In order to measure the admittance, one must know the comples amplitude of the current I through the sample, for a complex voltage V across the sample. However, the oscilloscpe shown in Figure 2-16 can only measure voltages. This problem is avoided by measuring the input and output voltages simultaneaouly, with respect to the ground.

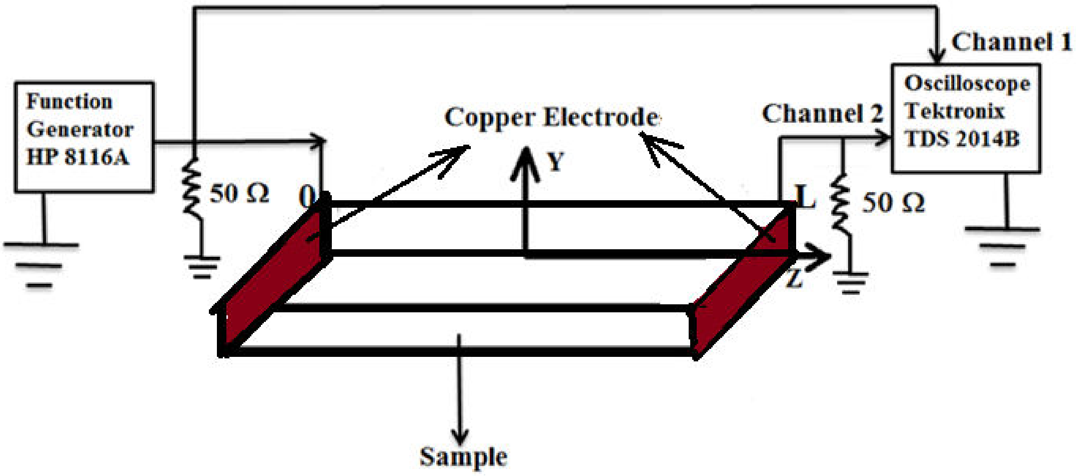

Figure 2-16. Experimental setup to measure r-f admittance of LN

2.9 Experimental Setup to Observe Nonclassical Nonlinearity from Lithium niobate

Figure 2.17 shows the experimental setup to observe nonclassical nonlinearity from Lithium niobate. The sample used was YZ-LNO-Plate. Copper electrodes strips of width 2 mm are attached to the ends of the sample. The adhesive between the electrode and the sample is epoxy, which overcomes the Schottky barrier formed at the junction of the metal electrode and the dielectric. The input burst is provided by an HP 8116A function generator. The input burst consists of 10 cycles. The amplitude of the input signal was fixed at 5 V. The duty cycle of the function generator was 50 percent, at this duty cycle the function generator can producea frequency upto 40 MHz. The output is observed on the screen of a TDS 2014B digital oscilloscope. The digital oscilloscope is triggered externally by the function generator.

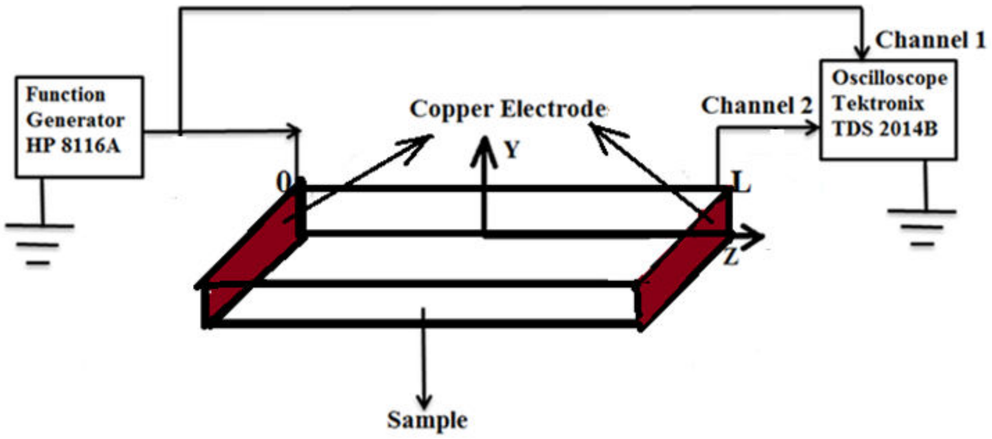

Figure 2-17. Experimental setup to observe nonclassical nonlinearity from LN.

CHAPTER III

INVESTIGATION OF IMPURITIES AND DEFECTS IN LITHIUM NIOBATE

3.1 Spectra of Photoluminescence from Single Crystal Lithium niobate

In this section the impurities and defects in LN will be investigated by studying the spectra of PL from bulk, wafer and plate single crystal LN samples. The impurities will be identified by recording the PL spectra by the experimental setup shown in Figure 2.8, and also by computer simulations of the spectral lines for direct and indirect bandgap LN samples.

3.1.1 Spectra of Excitation of Impurities in Lithium niobate

The purpose of monochromators in luminescence spectroscopy is, on one hand, to observe the spectral content of luminescence emission, and, on the other hand they can be applied to select a suitable excitation wavelength from an optical excitation source. When the luminescence signal is measured as a function of the excitation wavelength at a fixed emission wavelength, one speaks of the excitation spectra. The PL excitation spectrum is a plot of the PL intensity I_{PL} (at a fixed emission frequency $\nu_{em} = \frac{c}{\lambda_{em}}$) as a function of the excitation photon energy $h\nu_{ex}$:

$$I_{PL}(\nu_{em}) = f(h\nu_{ex}); \nu_{em} = constant \text{.................................} (3.1)$$

The motivation for measuring excitation spectra is purely practical. Luminescence radiation is generally very weak[112]. Hence all means of optimizing the luminescence signal should be used. In this sense, the excitation spectrum gives a clear hint about the choice of an optimum excitation wavelength – this is a wavelength (or excitation photon energy) at which the emission spectrum is peaked.

The different point defects in LN have different excitation wavelengths. Figure 3.1 (a) shows the spectra of excitation for the F-center defect, Ba and Ar impurities, and the antisite (Nb_{Li}^{4+}) defect. It can be observed that the excitation peaks are sharp. These different excitation wavelengths, produces a very bright emission line for its corresponding defect. However it suppresses many of the other defects. The excitation that produced well resolved peaks for most impurities is 310.00 nm, which is the excitation wavelength for the F-center defect. Thus all measurements were made by fixing the excitation monochromator at 310.00 nm, unless otherwise specified. Figure 3.1 (b) shows the excitation spectrum for the Fe^{+} impurity. It can be observed that the spectrum consista of a broad region between 345 nm and 370 nm with several peaks. This broad region has been observed in the excitation spectrum of quartz and has been attributed to the onset of direct and indirect absorption[112]. A sharp excitation peak appears at 370.91 nm. This is the wavelength that was used to excite the Fe^{+} impurity im LN.

Figure 3.2 shows the emission peak of the antisite defect at its excitation wavelength of 402.98 nm. The emission spectrum consists of a sharp peak which is about 4 times lower in intensity than the excitation peak in Figure 3 (a). The peak of the emission spectrum is red-shifted from the peak of the excitation spectrum by 0.70 eV. Such a red shift between excitation and emission peaks is called Stoke's shift. A sizeable Stoke's shift of a few electron-volts as in quartz indicates low power efficiency of luminescence, and most likely also the occurrence of a complicated mechanism of excitation energy transfer from a light-absorbing system to luminescence centers[112]. That is not the case in LN for which the Stoke's shift for antisite defects is less than 1 eV.

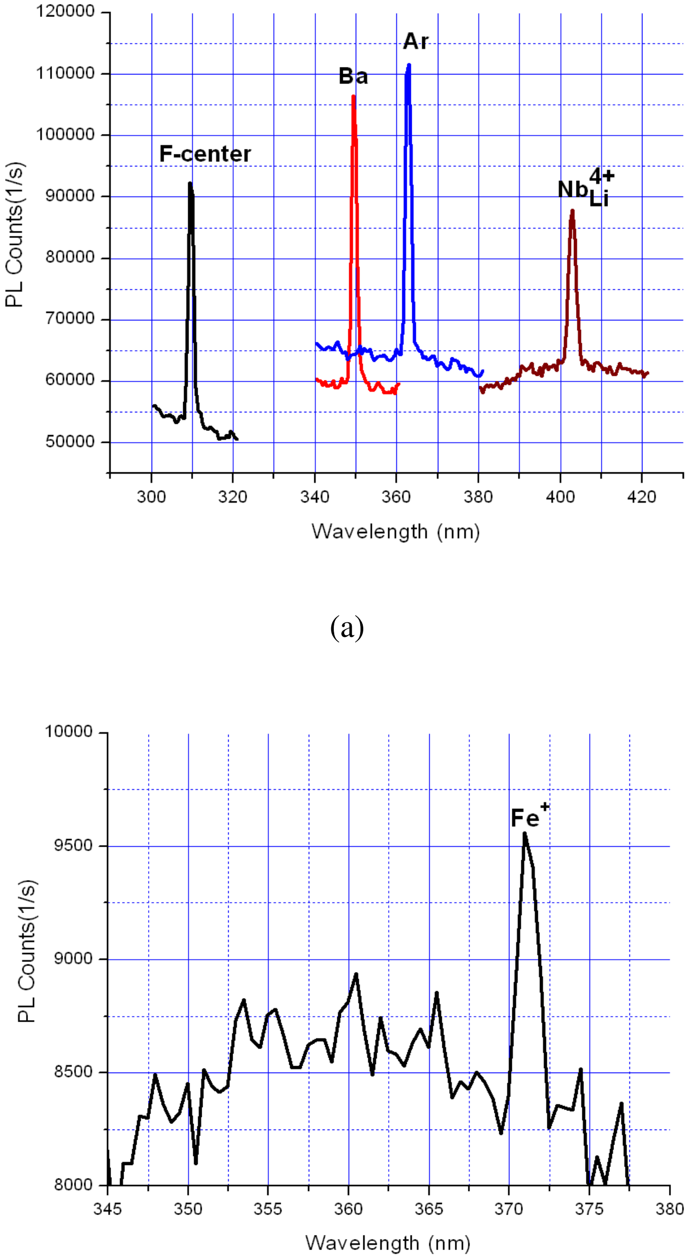

(a)

(b)

Figure 3-1. Spectra of excitation for: (a) F-center defect at 310.00 nm, Ba impurity at 349.00 nm, Ar at 363.00 nm and antisite (Nb_{Li}^{4+}) defect at 402.98 nm, (b) Fe^+ impurity, the sharpest excitation line is found at 370.91 nm.

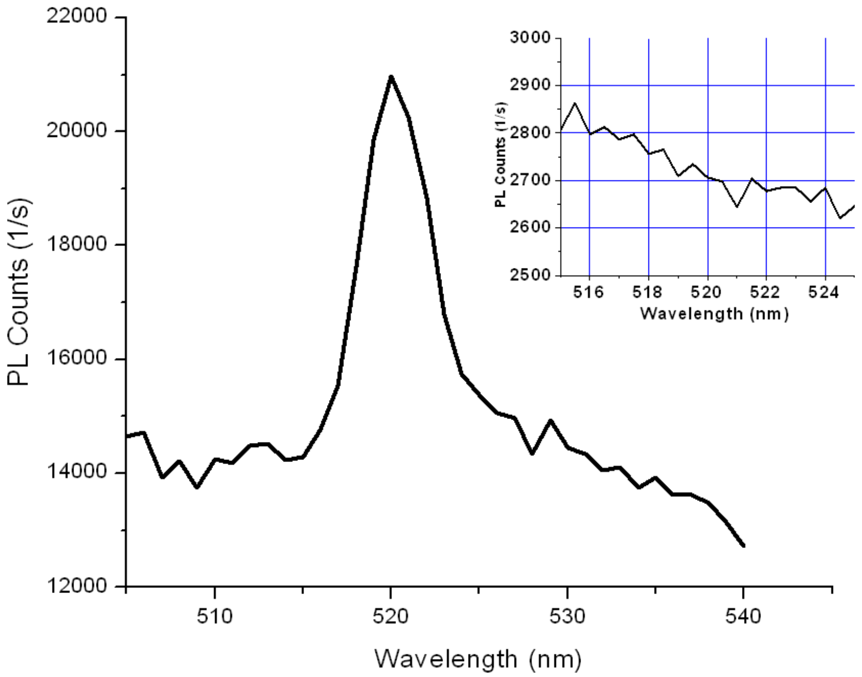

Figure 3-2. PL spectrum of the antisite defect at excitation wavelength of 402.98 nm. A sharp emission peak appears at 520.14 nm. The inset shows the PL spectrum at excitation of 310.00 nm, the peak due to the antisite defect does not appear at this wavelength.

It was observed that the host atoms Li and Nb produced prominent peaks at their excitation wavelengths. However the PL counts produced were very high and reached the saturation point of the instrument. This can be observed in Figure 3-3 (b) where the top of the peak for Li PL counts is flat. This happens because the density of host atoms is several orders of magnitude higher than the impurities. The Nb PL peak at 684.94 nm also exhibits similar behavior, at excitation wavelength of 342.33 nm. Thus the spectra of excitation helps to differentiate between the impurities and host atoms in LN.

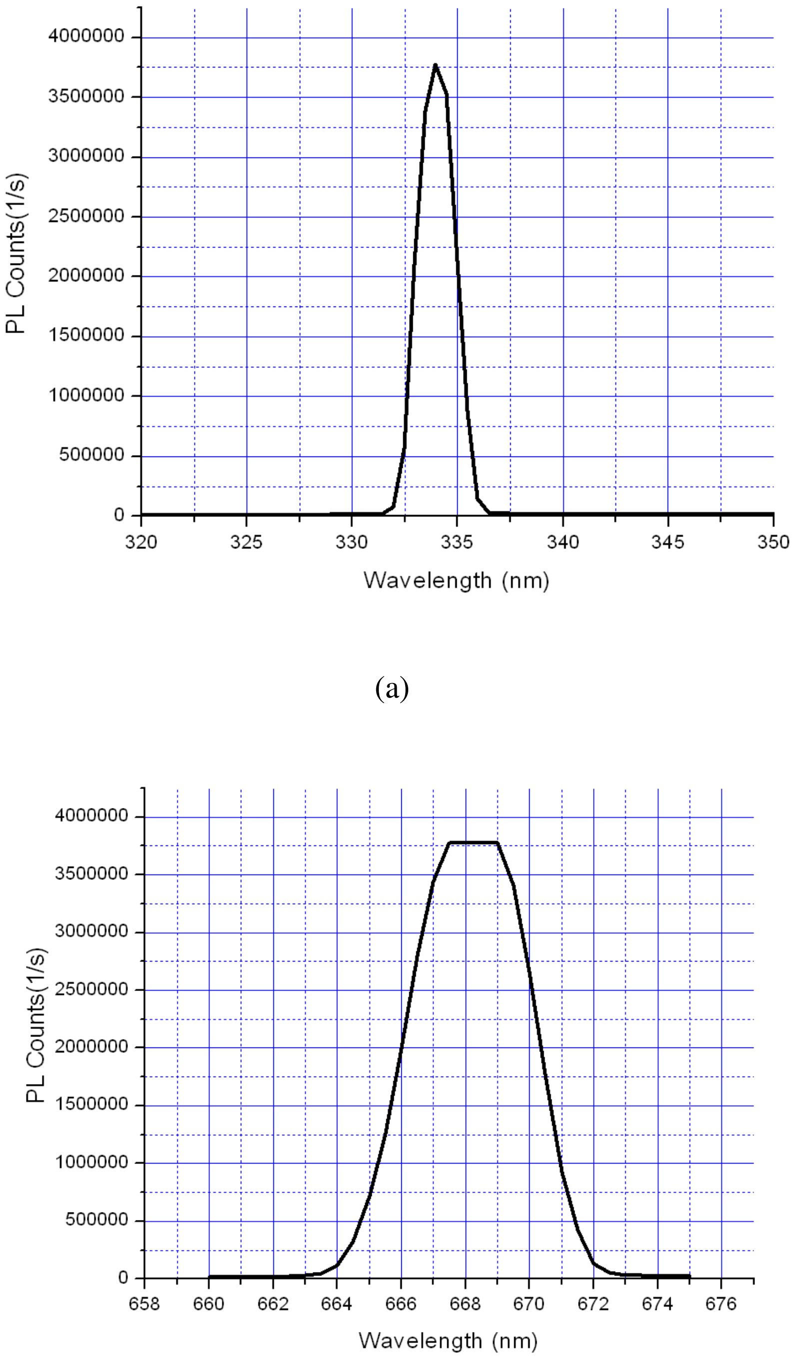

(a)

(b)

Figure 3-3. Excitation and emission PL peaks for Li. (a) Excitation peak for at 333.75 nm. (b) Emission PL peak for Li host atom at 668.73 nm show saturation in PL counts.The high number of emission PL counts imply that the detected Li atoms are the host atoms.

3.1.2 Spectra of Emission from Lithium niobate

Solid state luminescence can be divided into two basic types: intrinsic and extrinsic. Intrinsic luminescence originates in an ideal, pure and defect free crystalline lattice, while extrinsic luminescence has its origin in lattice-defects or impurities. A luminescence-active impurity atom, ion or molecule is frequently called an impurity luminescence center.

Now, a natural question arises. If, in the extrinsic case, the luminescence radiation originates in a microscopic impurity center, what then is the role of the host solid itself, i.e. the crystalline matrix? This matrix fulfills multiple funstions: (i) First of all, it represents a host medium inside which the luminescence centers are fixed, statistically dispersed, and mechanically isolated. (ii) The matrix also serves as an 'antenna' capturing the excitation energy and transferring it very efficiently to the luminescence centers. Next, (iii) owing to the interaction of the impurity electronic system with the matrix vibrations, the electron energy levels undergo important modifications which leads to substantial alterations of the optical spectra of the center[112].

Figure 3-4 shows the spectra of emission of LN with excitation of 310 nm. The spectrum is recorded from 320 nm to 900 nm. The specifications of the instrument required that the difference in wavelength between the excitation and emission are at least 10 nm apart. The region AB of the plot is the tail of the strong excitation line that should be present at 310 nm. A large peak C is observed at 620 nm, which is formed due to second order reflection of the exciting radiation from the monochromator grating. The presence of the large peak suppresses the peaks due to the defects. Hence the spectra was divided into two parts, the blue-green region and the near-infrared region as shown in Figure 3-5.

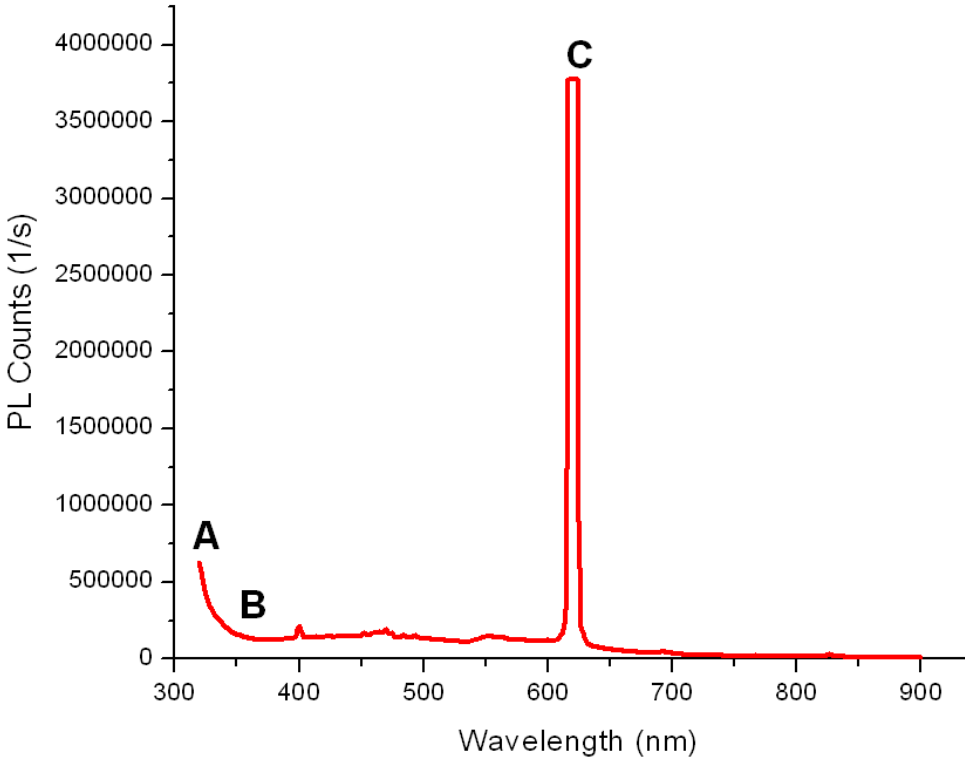

Figure 3-4. Emission spectrum of LN at excitation of 310 nm. AB represents the tail of the excitation line. The sharp peak C is formed at twice the excitation wavelength may suppress the peaks due to the impurities and point defects in this region. Therefore, the emission spectra were divided into two parts: the blue-green part extending from 350 nm to 590 nm, and the near-infrared part extending from 650 nm to 890 nm.

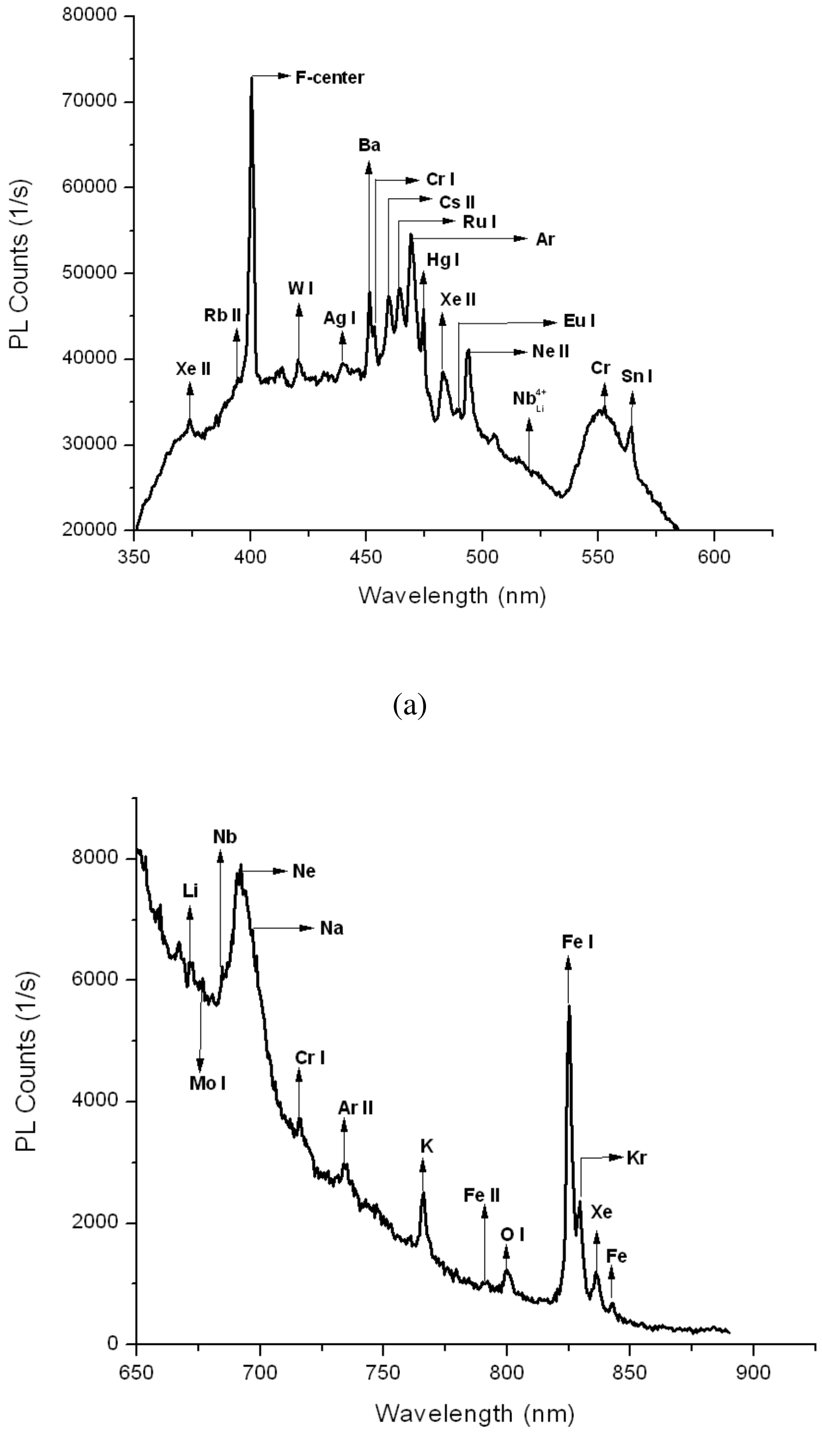

(a)

(b)

Figure 3-5. PL spectra from the sample YZ-LNO-Wafer-2. (a) Blue-green part of the spectrum, (b) near-infrared part of the spectrum. The number of averages performed is 3. The best time of integration is 0.5 sec.

The typical spectra of PL are shown in Figure 3-5, where panel (a) presents the blue-green part and the panel (b) presents the near-infrared part of PL. The highest line at 400.50 nm in the fig. 1(a) corresponds to the F-center[113] or color center. The presence of noble gases such as Xe, Ar, Ne and Kr are observed[114] as well. Several heavy metals such as Rb, W, Ba, Cs, Ru, Hg, Fe etc. are also observed[114]. Alkali metals like Na and K are observed in the near-infrared part of the spectrum[114]. The host atoms Li, Nb and O[114] are located in the near-infrared part of the spectrum, while an antisite defect (Nb_{Li}^{4+})[115] is detected in the blue part of the spectrum. Other than point defects, linear defects such as dislocations are expected to be present in LN. This is the cause for the presence of the background in the PL spectra.

Figure 3-6 shows the evolution of the dislocation in LN when the excitation is changed from 310 nm to 349 nm. When the excitation wavelength is 310 nm, the dislocation is best approximated by a Lorentzian function. The peak of the dislocation is at 449.24 nm. The intensity of the dislocation band at excitation with 310 nm is about four times higher than excitation with 349 nm. The dislocation at 349 nm excitation wavelength is best approximated with a Voigt function. The voigt profile results from the convolution of two broadening mechanisms: one would produce the Gaussian profile due to Doppler broadening, the other is the Lorentzian profile. The peak of the voigt dislocation band lies at 490.40 nm. Thus when the excitation wavelength increases from 310 nm to 349 nm, the peak of the dislocation band is red-shifted by 0.23 eV. The red shift of dislocations have been observed in ZnS and CdS, when excited with microwave radiation[116]. The presence of dislocations create additional energy states in the valence and conduction bands in LN. The transition of electrons between these energy states is observed as light emission. It may be noted that the highest line in Figure 3-6, when excited with 349 nm is due to the impurity Ba. This is because 349 nm is the excitation wavelength for Ba as already discussed in Figure 3-1 (a).

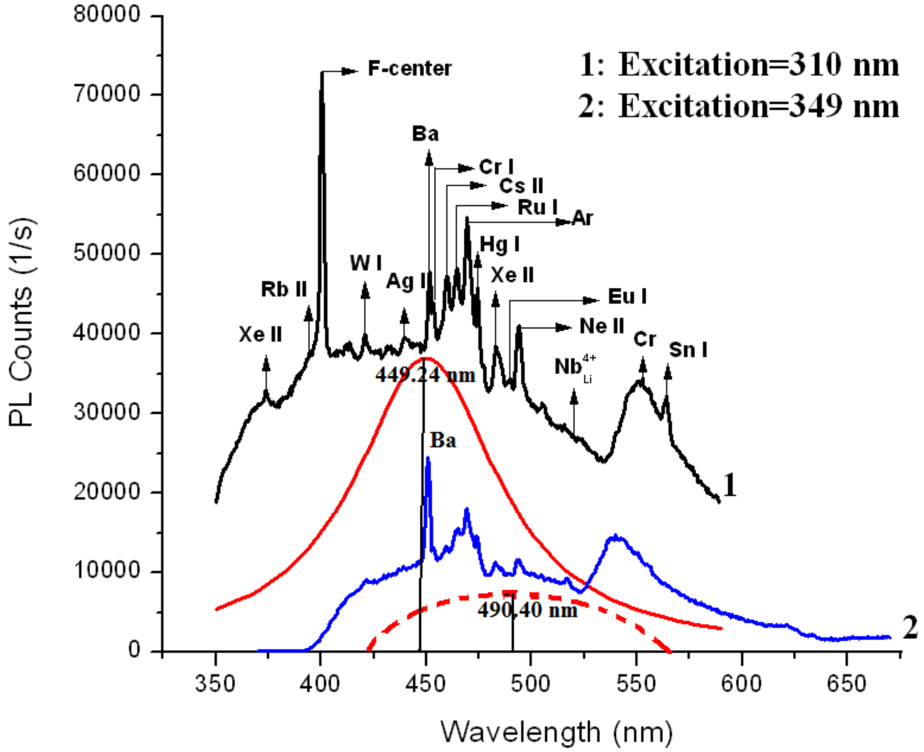

Figure 3-6. Emission spectra of LN at excitation wavelength of 310 nm (plot 1) and 349 nm (plot 2). The dislocation for plot 1 is centered at 449.24 nm and the best fit is a Lorentzian function, represented by the solid red line. The dislocation for plot 2 is centered at 490.40 nm and the best fit is a Voigt function, represented by the dashed red line. Therefore, it can be concluded that when the excitation wavelength is increased, the dislocation is red shifted.

3.2 Recombination of Free Carriers in Direct and Indirect Bandgap

A fundamental difference between the recombination of electron-hole pairs in a semiconductor with a direct and indirect bandgap is shown in Figure 3-7[112]. In a direct bandgap material, the recombination takes place between electrons and holes with the same wavevector k_0, where as in an indirect bandgap material, an excited electron with energy E_2 can recombine with any hole with energy E_1 and varying values of k, as long as the energy conservation rule $E_2 - E_1 = h\nu \pm \hbar\omega$ is fulfilled. The energy $\hbar\omega$ then denotes the conservation of quasi-momentum: $k_{\hbar\omega} = |k(E_2) - k(E_1)|$. Considering the fact that phonon dispersion relations are defined for any k from the first Brillouin zone, it is obvious that an appropriate phonon can always be found, unless the transition is forbidden due to symmetry of electron and/or phonon states. The recombination process is accompanied by the emission of a photon and the emission of a phonon, i.e. the electron excitation energy is released both in the form of luminescence and as an additional vibration energy of the lattice: $E_2 - E_1 = h\nu - \hbar\omega$.

An impurity atom in a semiconductor, whose valence is smaller (larger) by one electron than the main constituent of the crystal lattice, is referred to as a shallow acceptor (donor). Classic examples of a shallow acceptor (donor) are boron (phosphorous) atoms in silicon. The impurity atoms replace the host atoms creatind additional holes or electrons that are loosely bound. The loosely bound carriers can be thermally excited into the valence (conduction) band, thus boosting the electrical conductivity of the material. The corresponding amount of energy needed for the release of the hole or electron is referred to as the ionization (binding) energy of the acceptor E_A or donor E_D. The difference in

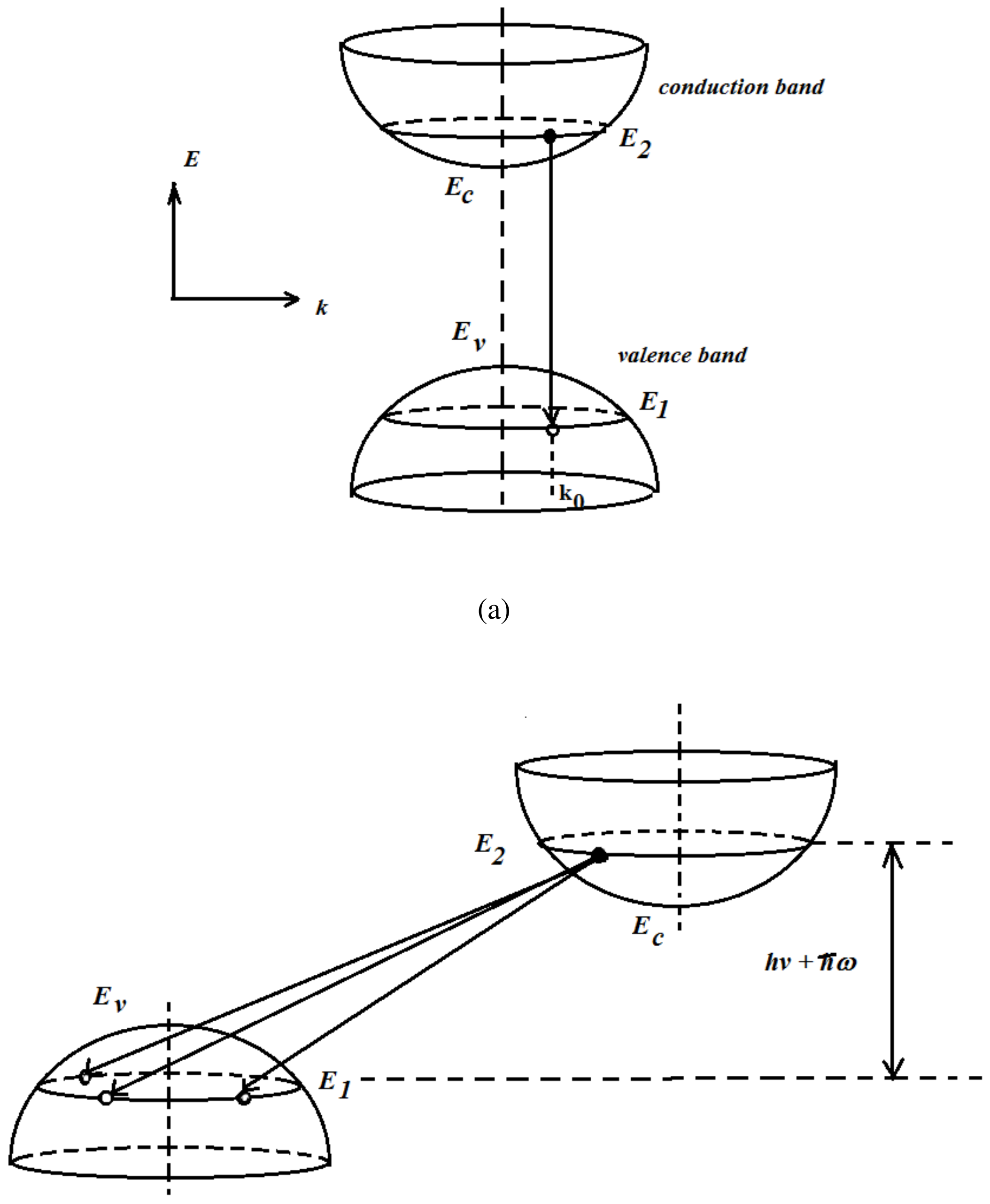

(a)

(b)

Figure 3-7. Schematic drawing of radiative recombination of electron-hole pairs in the energy band structure diagram $E(k)$ for a material with: (a) a direct and (b) an indirect bandgap. $h\nu$ stands for the energy of the emitted photon, $\hbar\omega$ for the energy of the emitted phonon. An excited electron with energy E_2 can recombine with any hole of energy E_1 as long as the conservation of energy is fulfilled. The three arrows in (b) denote that the electron in energy level E_2 can recombine with any of the holes present in E_1[112].

energy between the acceptor (donor) level and the extreme of the valence band equals E_{A} (or E_{D} in the case of the conduction band).

It is estimated that the vacant 4d energy states of Nb form the conduction band while the filled 2p energy states of O make up the valence band in LN. A free electron (*e*) present at the bottom of the conduction band can recombine with an acceptor (*A*). This leads to the emission of a luminescence photon with approximate energy $h\nu \approx E_g - E_A$ [112]. The spectral line shape of luminescence for a direct bandgap transition is given by[112]

$$I_{sp}^{(e-A)} \approx [h\nu - (E_g - E_A)]^{1/2} \exp(-\frac{h\nu-(E_g-E_A)}{k_B T}) \text{ .... } (3.2)$$

where $I_{sp}^{(e-A)}$ is the intensity of the spectral line due to the electron-acceptor recombination, E_g is the band gap of LN, E_A is the energy of the acceptor level, k_B is the Boltzmann constant and T is the room temperature. The spectral line shape of luminescence due to recombination of a hole (*h*) with a donor (*D*) is given by[112]

$$I_{sp}^{(h-D)} \approx [h\nu - (E_g - E_D)]^{1/2} \exp(-\frac{h\nu-(E_g-E_D)}{k_B T}) \text{ .... } (3.3)$$

where $I_{sp}^{(h-D)}$ is the intensity of the spectral line due to the hole-donor recombination and E_D is the energy of the donor level.

The shape of the spectral lines of the defects for direct bandgap LN was plotted, and the energy of the acceptor / donor level was computed using equations (3.2) and (3.3). The plots are presented in Figure 3-9 (a), (b) and (c). The computer code in Mathematica used to develop the theoretical spectral line is in the Appendix. It is observed that the position of the peaks between the experiment and theory are in good agreement. The experimentally observed Xe II line in

Figure 3.9 (a) is blended with another line, which results in a shoulder near 484.50 nm. This blended line appears in air at 483.108 nm according to the NIST database, while it appears at 483.05 nm in LN. Thus the spectral line shifts by 0.012 % in LN. Similar calculations can be performed for the other defects that are identified from the NIST Database, such as the Fe I defect. The Fe I defect is observed in the spectra of PL at 824.86 nm, while it is reported for air at 824.81304 nm[114]. Thus the Fe I spectral line shifts by 0.006 % in LN. The small shift between theory and experiment validates the identification of spectral lines in LN using the NIST database.

Figures 3.9 (b) and (c) show the experimental and theoretical peaks due to the F-center defect and the antisite defect respectively. The peaks of the theoretical and experimental plot coincides for the F-center defect. For the antisite defect, the position of the peaks between theory and experiment vary by 0.067 %. Figure 3.8 demonstrates that the theory and experiment are in good agreement. However, the theoretical plot shows a steep decay on the low energy side, while the experimental plot does not. This difference can be due to several factors including the influence of the slit of the monochromator, which smears the luminescence spectrum. Another possible reason is the broadening of the spectral lines due to thermal collisions of the carriers at room temperature. Thus photons with higher energy are generated by these higher energy electron-hole pairs, while the low-energy onset of the spectral line is determined by E_g and its position remains fixed.

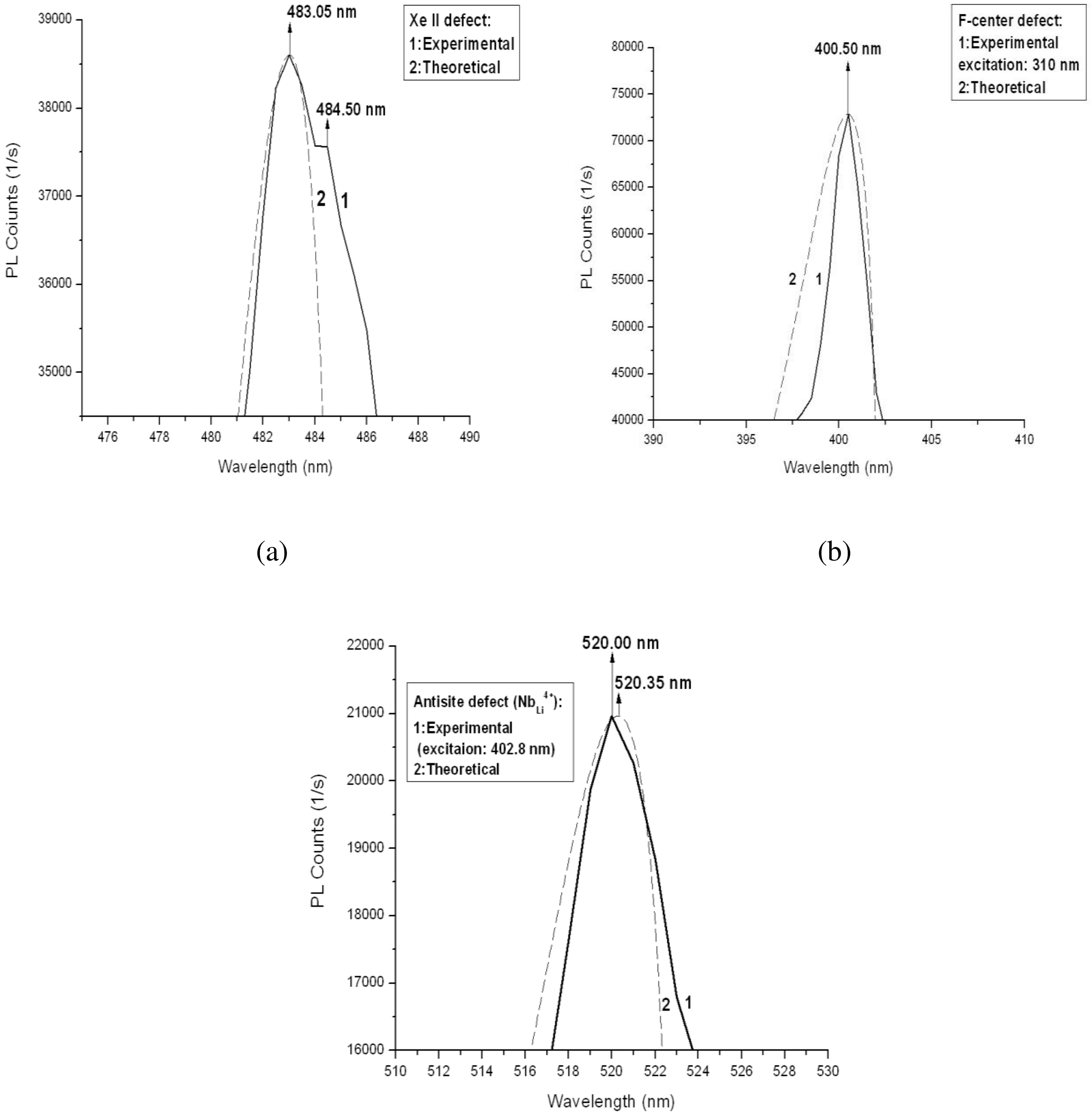

(a)

(b)

(c)

Figure 3-8. Plot of experimentally observed and theoretically computed PL spectral line for (a) Xe II, (b) F-center, and (c) antisite defects in direct bandgap LN. The PL counts of the theoretically computed peaks are matched with the experimentally obtained peaks.

For indirect transitions, the line shape is given by[112]

$$I_{sp}^{ID(e-A)} \approx [h\nu - \big((E_g - \hbar\omega) - E_A\big)]^2 \exp(-\frac{h\nu - \big((E_g - \hbar\omega) - E_A\big)}{k_B T}) \quad \text{........(3.4)}$$

Where $I_{sp}^{ID(e-A)}$ is the intensity of the spectral line due to the electron-acceptor recombination in the indirect band gap, $\hbar\omega$ is the energy of the mediating phonon. It can be calculated from reference 82 that the difference in the direct and indirect band gap in near stoichiometric LN (nsLN) differs by not more than 5 %. So the PL peaks of the defects due to indirect transitions, should lie within 5 % of the peaks due to direct transitions .

Equation (3.4) is not very different from equation (3.2). The first difference is represented by the red shift of the low-energy side of the spectrum by $\hbar\omega$. The second difference is the replacement of the square-root dependence of the pre-exponential factor in equation (3.2) by a quadratic dependence in equation (3.4). The change in the pre-exponential factor modifies the low-energy onset of the spectrum, which is also influenced by spectral broadening due to dispersion by the slits. The shape of the high energy tail is most significantly influenced by the exponential factor. Figure 3-9 shows the emission lines due to direct and indirect transitions in nsLN. These spectral line are plotted using a computer code in Mathematica, shown in the Appendix. For the Xe II defect in Figure 3-9 (a), the difference in the position of the peaks due to direct and indirect transitions, vary by 1.42 %. For the F-center defect in Figure 3-9 (b), the difference in the position of the peaks due to direct and indirect transitions, vary by 3.18 %. There is significant broadening of the lineshape for indirect transitions in both the Xe II and F-center defects. This is due to the the fact that the excited electrons and holes in an indirect bandgap material, live much longer than in direct bandgap materials. Thus at room temperature, the thermal collisions between the particles are manifested in the broad spectral line.

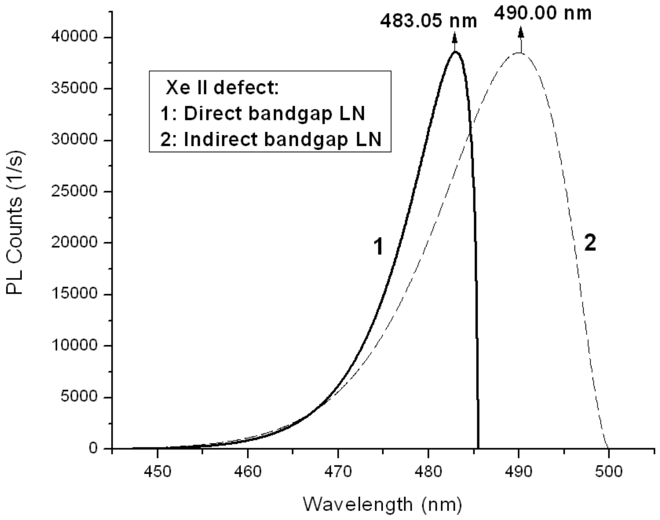

(a)

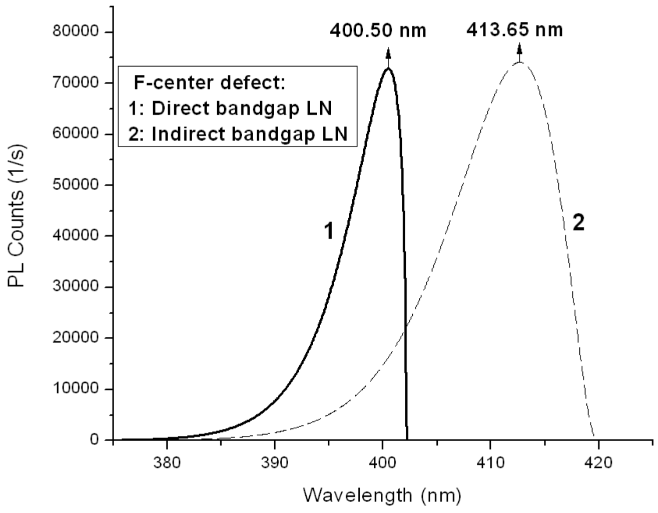

(b)

Figure 3-9. Comparison of emission lineshapes of the recombination of free electron-hole pairs for (a) Xe II, and (b) F-center defects; under direct (plot 1) or indirect (plot 2) optical transition.

As discussed earlier, the steep decline of the PL line in the low energy side of a direct bandgap material is attributed to the bandgap E_g, which remains constant in the theoretical model. In reality, the valence and conduction bands form a tail due to the presence of density of states due to the crystal defects. In a real crystal, the low energy onset of PL is governed by the presence of structural defects and disorder present in the medium. The presence of these defects affect the PL spectral lines and optical absorption processes near the band edge. An exponential fit called the Urbach tail describes the photon absorption processes in direct bandgap semiconductors[117]. The Urbach's rule states that the frequency dependence of the absorption for $\hbar\omega < (E_g - E_A)$ is given by:

$$\alpha(h\nu) \propto \exp(\frac{\sigma(h\nu-(E_g-E_A))}{k_B T}) \ldots\ldots\ldots\ldots\ldots\ldots\ldots\ldots\ldots\ldots\ldots(3.5)$$

An impurity that forms a donor level will replace E_A with E_D in equation (3.5). The Urbach tail is modelled for the Xe II and antisite defects using a Mathematica code shown in the Appendix. Figure 3-10 shows the Urbach tail for the defects in LN. The addition of the Urbach tail to the direct bandgap PL lines reduces the sharp fall at the lower energy side. The tail extends for about 25 nm for both defects. The Urbach tail is associated with the width of the tail states in the bandgap and is related with the structural defects and disorder within the crystal[17]. The disorder that gives rise to exponential band tail is attributed to lattice vibration (phonons), impurities, and other deviations from perfect periodicity of the lattice. The presence of lattice imperfections distorts the NbO_6 octahedron in $LiNbO_3$, which affects the lowest point of the conduction band and highest point of the valence band[118].

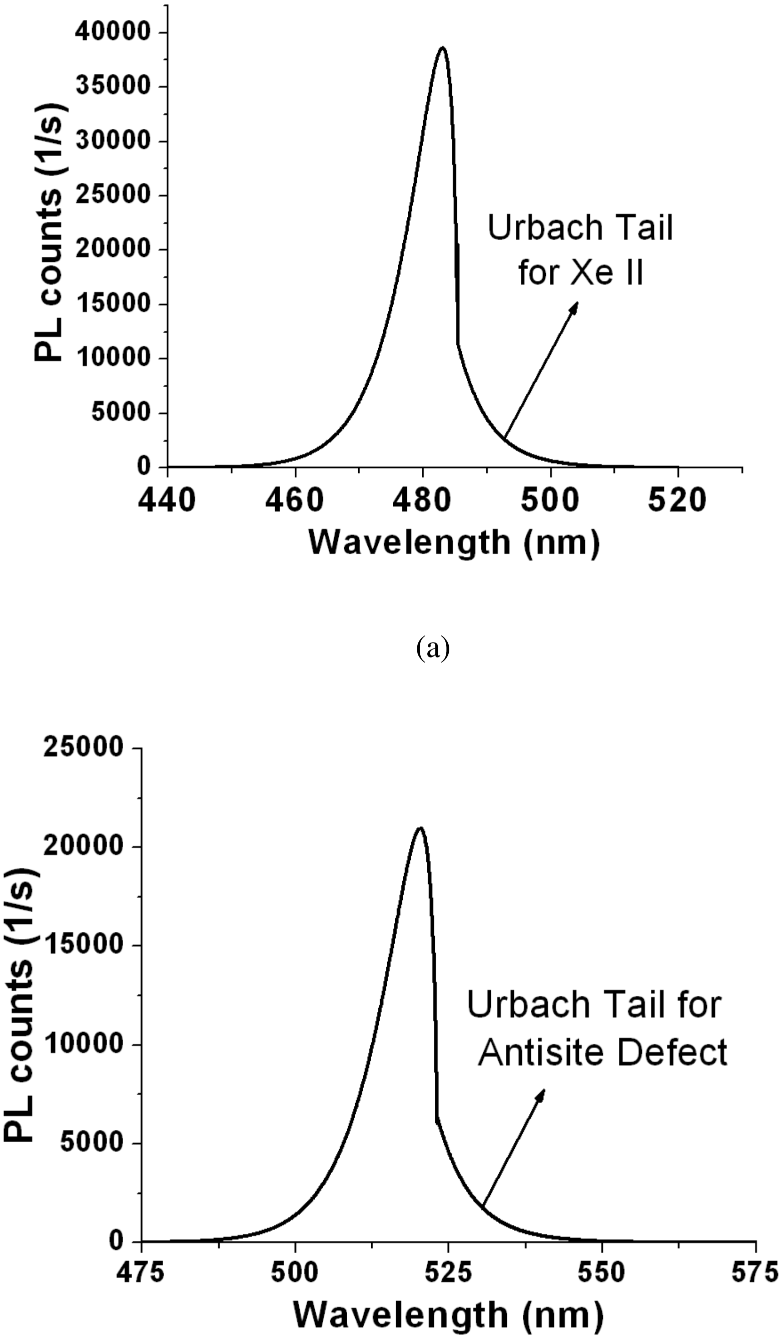

(a)

(b)

Figure 3-10. Plot of the Urbach tail that was computed for (a) Xe II and (b) antisite defect. The addition of the Urbach tail reduces the steep fall at the lower energy side of the PL spectra.

3.3 Spectra of Photoluminescence under Polarization from Lithium niobate

The z-axis in LN is the direction of the optic axis *c*. We are interested in the polarization of the luminescence light from the defects, either parallel to z or perpendicular to z. Figure 3-11 shows the polarization of the photoluminescence spectra of LN. The polarizer was used in two settings as shown in Figure 2-12; when the electric field vector $\overrightarrow{\boldsymbol{E_{PL}}}$ of the incident light was parallel to the *c* axis, and when $\overrightarrow{\boldsymbol{E_{PL}}}$ was perpendicular to the *c* axis.

The spectra of polarization reveals a preferred polarization directions of the luminescence light , which is parallel to the optical crystallographic axis *c*. It is observed from figure 3.11 that the luminescence light from the F-center, Ba, Fe^+ and noble gas impurities have a preferred polarization direction parallel to the *c* axis. Since the z-axis is the piezoelectrically active direction in LN, the impurities may influence the piezoelectric properties in the crystals.

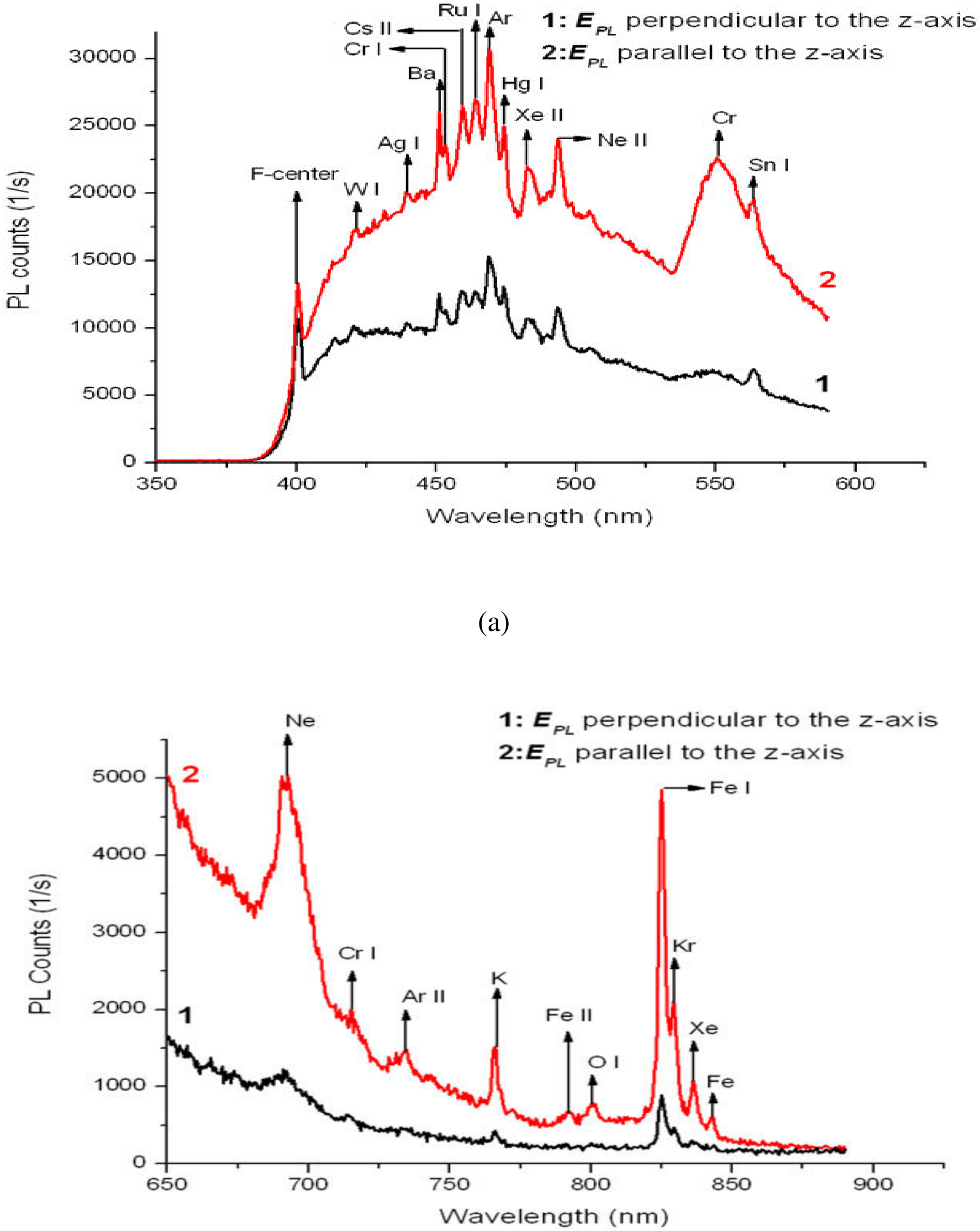

(a)

(b)

Figure 3-11. Polarizationion of PL from YZ-LNO-Wafer-2, under excitation by unpolarized light: (a) blue-green spectrum, (b) near-infrared spectrum.

3.4 Spectra of Transmission and Intraband Energy Levels in Lithium niobate

PL usually originates near the surface of a material. PL is an important tool in the characterization of surfaces[119]. However, in order to understand the phenomenon of nonclassical nonlinearity in detail, it is important to observe the impurities in the bulk of the material. Thus transmission spectroscopy of LN was performed. Figure 3-12 (a) shows the transmission spectrum of ZX-LNO-Wafer-1. The transmission spectrum of LN is observed using the "Perkin Elmer Lambda 18 Ultraviolet / Visible Spectrometer." The transmission edge is at 312.37 nm. Thus, the band gap Eg is equal to 3.97 eV. The presence of defects such as a bipolaron (Nb_{Li}^{4+}-Nb_{Nb}^{4+}) at 500.0 nm[120], Fe I at 562.0 nm, a small polaron (Nb_{Li}^{4+}) at 774.9 nm[82], noble gases like Xe at 885.6 nm and Ne at 892.0 nm[114], are revealed. The atoms Li and Nb[23] are observed as well. It is to be noted that although the antisite defect and the small polaron are both connected to Nb_{Li}^{4+}, they are different defects. The antisite defect is caused by the exchange in position of the Nb and Li atoms in the crystal lattice. The small polaron is formed when an electron gets trapped at a Nb_{Li}^{5+} site, thereby distorting of the oxygen octahedron around it. Figure 3-12 (b) shows the peak the small polaron, which is enlarged from the transmission spectrum. The different impurities in LN form intraband acceptor and donor energy levels.

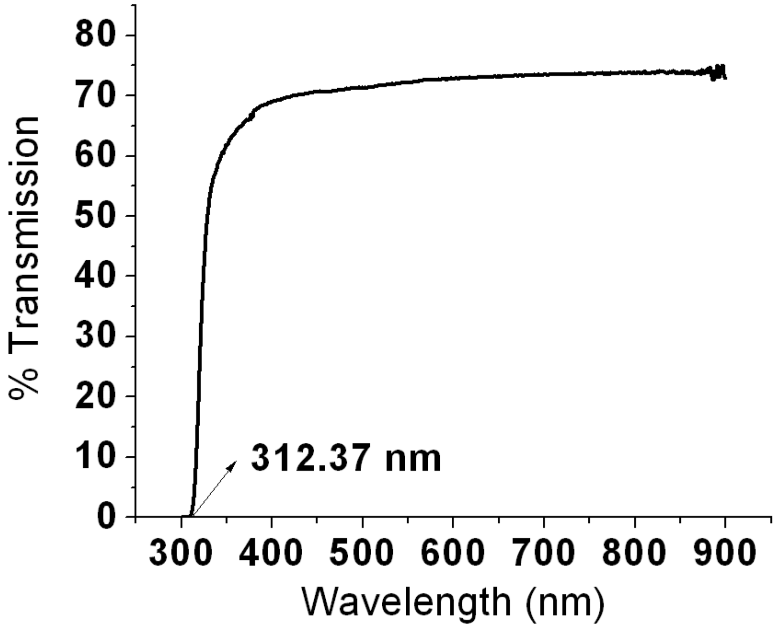

(a)

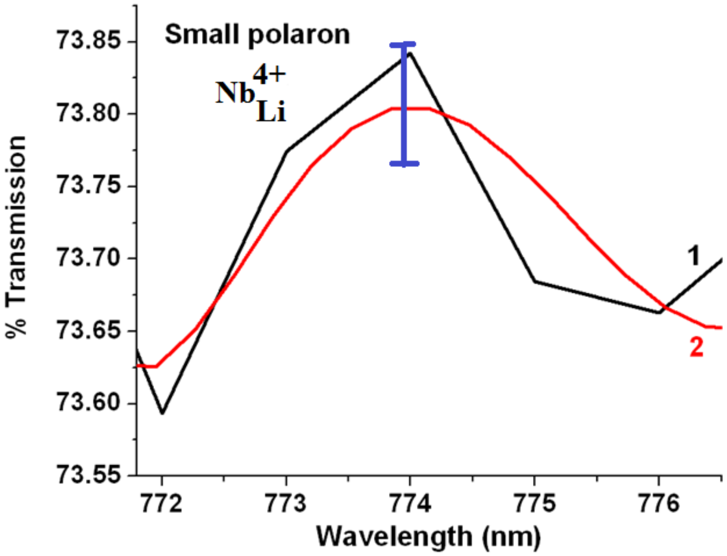

(b)

Figure 3-12. (a) Transmission spectrum of LN recorded from the sample ZX-LNO-Wafer-1. The peaks due to the defects are not resolved at this scale. (b) Enlarged peak due to the small polaron. The experimentally obtained plot 1 is smoothened using the software Origin 7 to create the plot 2.

Figure 3-13 shows a sketch of the energy band scheme of LN with intraband donor levels (D) and acceptor levels (A). The 4d energy levels of Nb form the conduction band (CB) while the 2p energy levels of O form the valence band (VB). The band is bending at the line defect and is dominated by the dislocation charge. The light emission process with the energy hν arises in the electron (e^-) transition shown the the figure. The depth of the dislocation line is calculated from the shift in position of the dislocation peak, when the excitation wavelength is changed from 310 nm to 349 nm. The metals form donor levels as they readily give up electrons. Due to low ionization energy, small fluctuations in temperature and other parametes may be sufficient to move the outer electrons to the conduction band. The F-center forms a donor level, the F-center is formed when an electron is trapped at the site of a Li vacancy in LN. The electron is loosely bound and easily moves to the conduction band thereby contributing to the electrical conductivity of LN. The Ne and Xe impurities are noble gases with very high first ionization potentials (21.56 eV for Ne and 12.13 eV for Xe)[121]. Thus these impurities are unable to easily donate electrons to the conduction band, it is unlikely that these impurities will form donor levels. Hence in the energy band scheme, the noble gas impurities are shown to form acceptor levels. The antisite defect (Nb_{Li}^{4+}) carries a high positive charge and readily accepts electrons from the valence band. It is shown as an acceptor level, the oxygen octahedra around the antisite defect becomes distorted. The distortion moves under the application of an external electric field, thus giving rise to the small polaron (Nb_{Li}^{4+}). The bipolaron (Nb_{Li}^{4+}-Nb_{Nb}^{4+}) transmission line is observed at 2.48 eV, so it is expected that it will form an acceptor level. However, the expected acceptor level at 2.48 eV is much closer to the conduction band than the valence band. In the energy band scheme, instead of placing the bipolaron at 2.48 eV as acceptor level, it has been placed at 1.49 eV (= 3.97 eV – 2.48 eV) as a donor level. This makes sense due to the fact that the bipolaron has a very big size as it is formed by the attaraction between two polarons. This creates many loosely bound electrons which easily make a transition to the valence band.

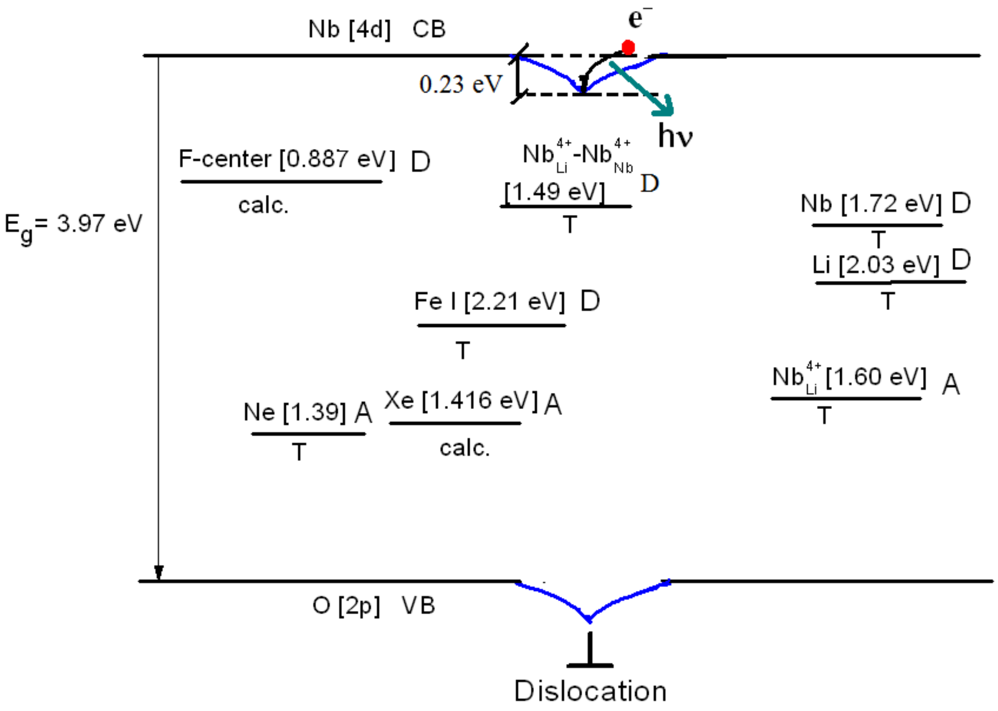

Figure 3-13. Energy band scheme of LN at room temperature. The band scheme shows intraband defect energy levels F-center, Fe I, Xe, Ne, small polaron Nb_{Li}^{4+} , bipolaron Nb_{Li}^{4+}-Nb_{Nb}^{4+},Li and Nb. The abbreviation calc. implies that the energy level was calculated from equations (3.2) and (3.3), T implies that it was observed in the spectra of transmission.

3.5 Distribution of Impurities in Lithium niobate in a Direction Parallel to the z-axis

The samples were moved in small steps during the experiment. The spectra were recorded at intervals of tens of microns. The aim was to find the distribution of the defects along the optical crystallographic z-axis. This optical scanning allows to find a distribution of the impurities in the samples. The photon counts changes with crystal position for some impurities. The distribution of these defects is observed as peaks and valleys when the samples are scanned parallel to the z axis.

Figure 3-14 and Figure 3-15 shows the distribution of Fe I impurities in the bulk samples, when scanned parallel to the z-axis. The outer curved faces of the samples exhibit swirl defects shown in Figure 2-4. The swirl defects are manifested in the PL counts for the bulk samples. This is shown in Figures 3-14 (a) and (b). The distance between consecutive peaks, named as the periodicity (*P*) for the Fe I swirl defects, lies between 360 μm and 560 μm in the sample LNO-P. *P* lies between 160 μm and 220 μm in LNO-U. The swirl defects suppress the contribution of the native point defects. A portion of the outer surface of the crystals was polished (Figure 2.4), the results are shown in Figures 3-15 (a) and (b). The periodicity of native Fe I impurities lies between 280 μm and 360 μm for LNO-P, and between 520 μm and 800 μm in LNO-U.

Figure 3-16 (a) and (b) shows the distribution of Fe-I impurities in the samples YZ-LNO-Plate and YZ-LNO-Wafer-2, when scanned parallel to the z-axis. The distribution reveals peaks and valleys. *P* lies roughly between 0.50 mm to 2.50 mm in YZ-LNO-Plate. In YZ-LNO-Wafer-2, the magnitude of *P* shows the presence of a microstructure and a macrostructure. The microstructure lies between 80 μm to 200 μm, while the macrostructure is close to 1.00 mm.

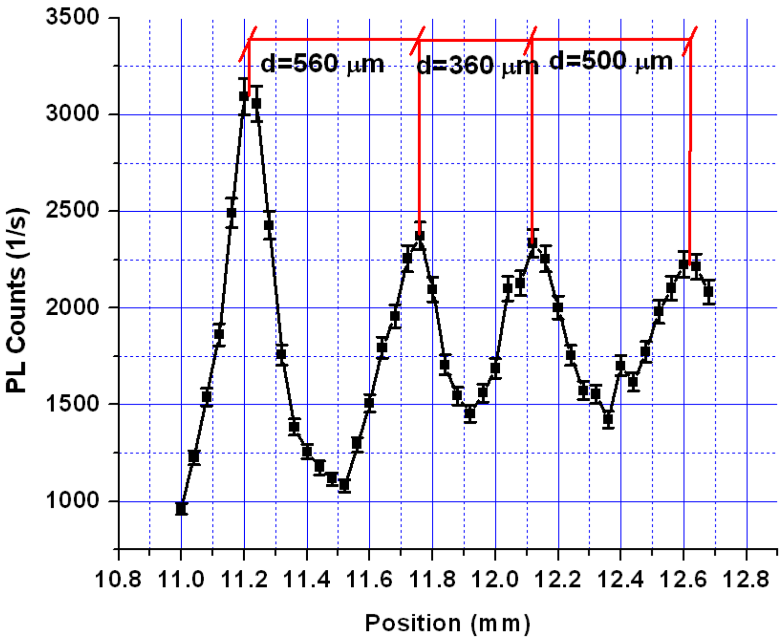

(a)

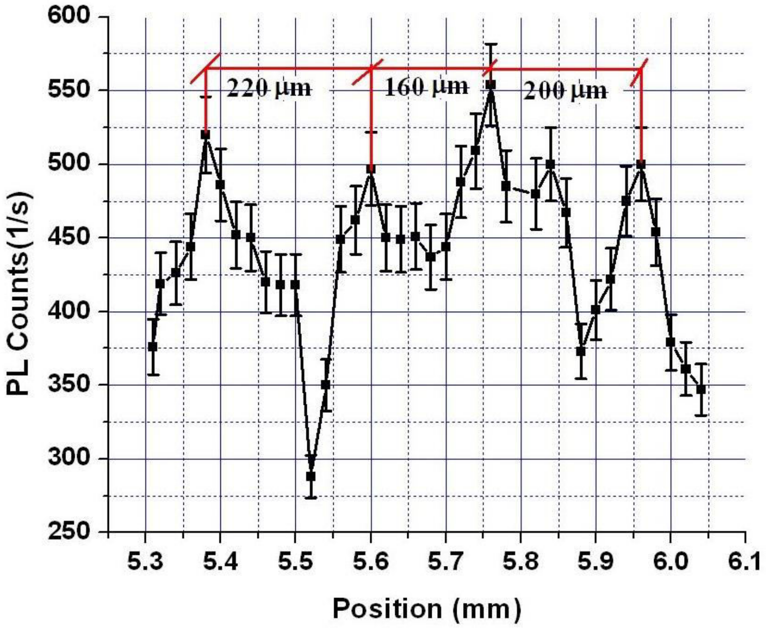

(b)

Figure 3-14. Distribution of Fe^+ impurities in unpolished bulk samples: (a) polarized LNO-P, and (b) unpolarized LNO-U. The swirl defects shown in figure 2-4 are reveal themselves in the PL spectra. The periodicity in LNO-P lies between 360 μm and 560 μm. The periodicity in LNO-U lies between 160 μm and 220 μm.

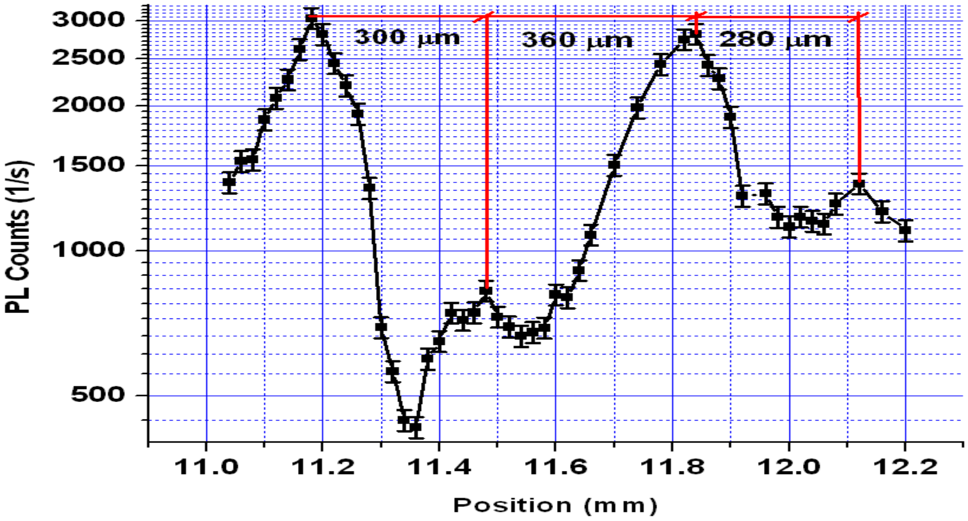

(a)

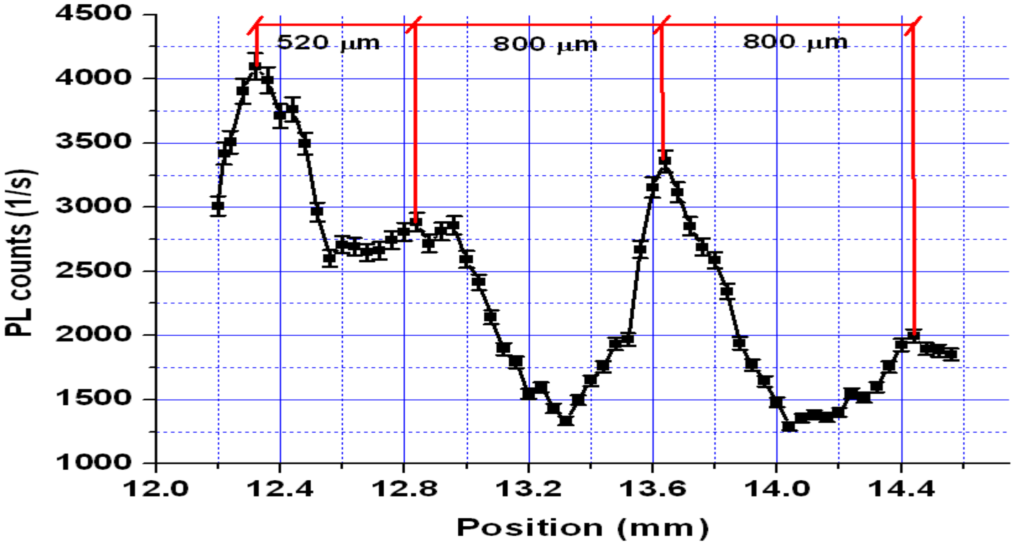

(b)

Figure 3-15. Distribution of Fe^+ impurities in the polished bulk samples (a) polarized LNO-P, and (b) unpolarized LNO-U. The periodicity in LNO-P lies between 280 μm and 360 μm. The periodicity in LNO-U lies between 520 μm and 800 μm.

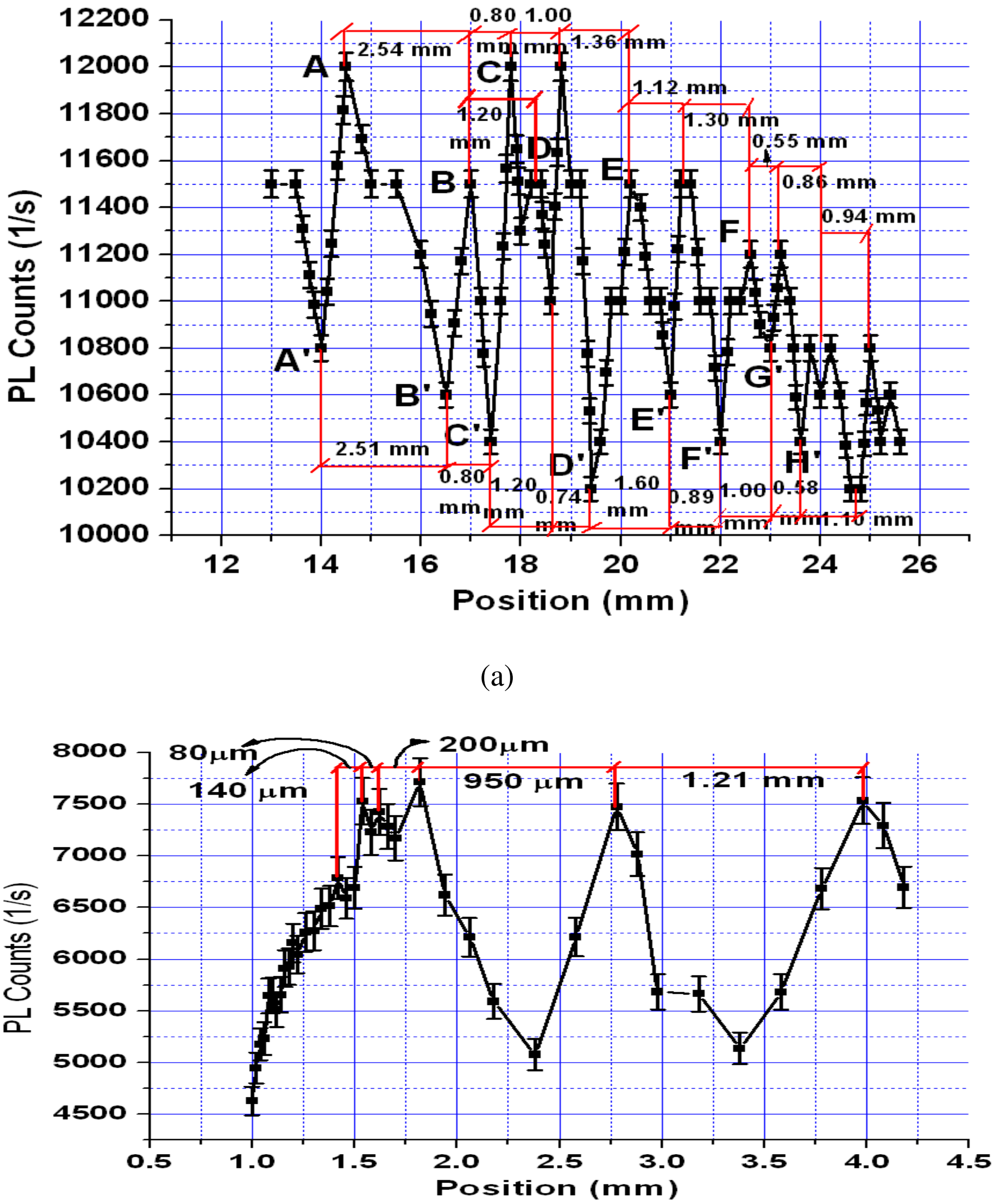

(a)

(b)

Figure 3-16. Distribution of Fe$^+$ impurities in (a) YZ-LNO-Plate. The points A, B…, A', B'…,1, 2,…1',2'.. will be compared with the electromechanical transformation in Section 4-1. (b) YZ-LNO-Wafer-2. Both YZ-cut wafer samples exhibit periodicity (*P*) of the order of a few mm, unlike the bulk samples where *P* is of the order of hundred microns.

Table 3-1: Maximum and minimum values of the periodicity (*P*), for Fe I defects in different LN samples. The range of *P* values are used to calculate the range of frequencies where LN exhibits nonclassical nonlinear behaviour.

Sample Used	Maximum value of *P*	Minimum value of *P*
LNO-P	360 μm	280 μm
LNO-U	800 μm	520 μm
YZLNO-Wafer-2	1.21 mm	0.95 mm
YZLNO-Plate	2.54 mm	0.55 mm

The defects in LN possibly affect the piezoelectric properties of the crystals. This has been observed in another piezoelectric material (K,Na)NbO$_3$-LiSbO$_3$, abbreviated as KNN-LS. It is observed that the piezoelectric constants of this material have a strong dependence on the microstructure [122]. When KNN-LS is doped with FeO, it changes the piezoelectric constant d_{33}. It is observed that an increase in the FeO doping content leads to a decrease in d_{33} [121]. The presence of Fe in LN may affect the piezoelectric properties.

The distance (*P*) between two consecutive peaks may be used to predict the frequency (*F*) range of possible influence of the defects on acousto-electric properties. The relationship between *P* and *f* may be written as

$$F \approx \frac{V}{P} \tag{3.6}$$

where *V* is the velocity of the acoustical wave. Let us consider the bulk crystals. Two consecutive peaks for the Fe I defect vary between 520 μm to 800 μm in the unpolarized bulk crystal (LNO-U). In the polarized bulk crystal (LNO-P), two consecutive Fe I defect peaks vary between to 280 μm to 360 μm. Thus nonclassical nonlinearity should be observed in LNO-U in the frequency range between 9.12 MHz to 14.03 MHz. In LNO-P, nonclassical nonlinearity should be observed in the frequency range between 20.28 MHz to 26.07 MHz. The frequencies calculated are in agreement with the frequencies at which AM was observed from these samples in reference 21.

The F-center is a crystallographic defect which is formed when a vacant crystallographic site is occupied by one or more unpaired electrons. It is observed that when the PL of the F-center has a maximum intensity in Figure 3-17(a), the PL of Li has a minimum intensity in Figure 3-17 (b), and vice-versa. This is shown by the circled points in Figures 3-17(a) and (b). Thus the F-center is formed at the site of a Li vacancy. Figure 3.17 (b) shows the distribution of the host atoms Li and Nb in the sample YZLNO-Wafer-2K. The excitation used was 333.75 nm for Li and 342.33 nm for Nb, which are the excitation wavelengths for these defects. The excitation wavelengths produce very high peaks with PL counts of the order of a million, thus Li and Nb are the host atoms and not point defects. This is discussed in Figure 3-3. It is observed that the periodicity of these defects is roughly 100 μm. This periodicity is close to the size of a domain in LN which varies between tens of microns to a few hundred microns[123, 124]. Figure 3-18 (a) and (b) show the distribution of F-center for the bulk samples, when the spectra are recorded in a direction parallel to the z-axis. The periodicity *P* lies between 280 μm and 360 μm for LNO-P, and between 500 μm and 810 μm in LNO-U. This is almost the same periodicity for Fe^+ impurities in bulk samples. The charged F-center and the antisite (Nb_{Li}^{4+}) defects contribute to the electrical conduction of LN by the mechanisms discussed in Section 1.12. Figure 3.19 shows the distribution of the antisite defect in LN, when the spectra are recorded parallel to the z-axis. For the antisite defect, *P* lies between 70 μm and 200 μm.

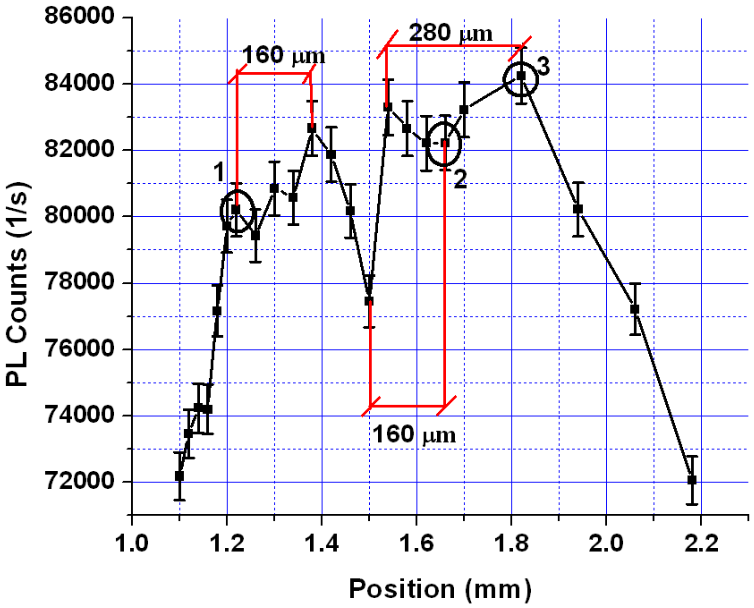

(a)

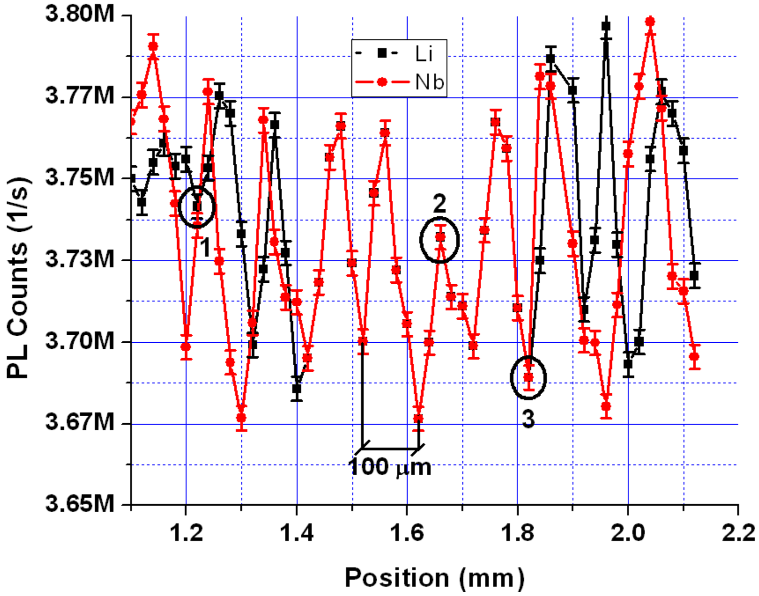

(b)

Figure 3-17. Distribution of: (a) F-center defects in YZ-LNO-Wafer-2 at an excitation of 310 nm, (b) Li and Nb host atoms at excitations of 333.75 nm and 342.33 nm respectively. The points 1, 2 and 3 show that when the PL counts for Li are minimum, the PL counts for the F-center are maximum, and vice-versa. This leads to the conclusion that the F-center is formed at the location of Li vacancies.

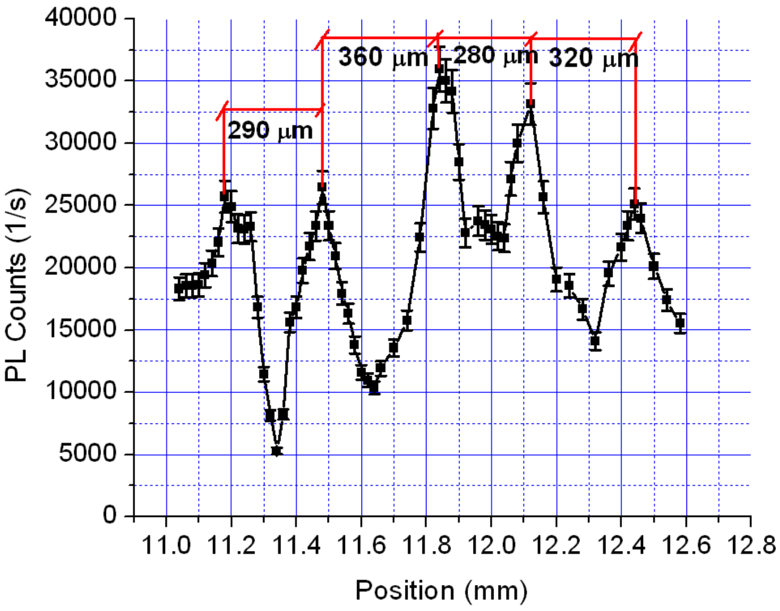

(a)

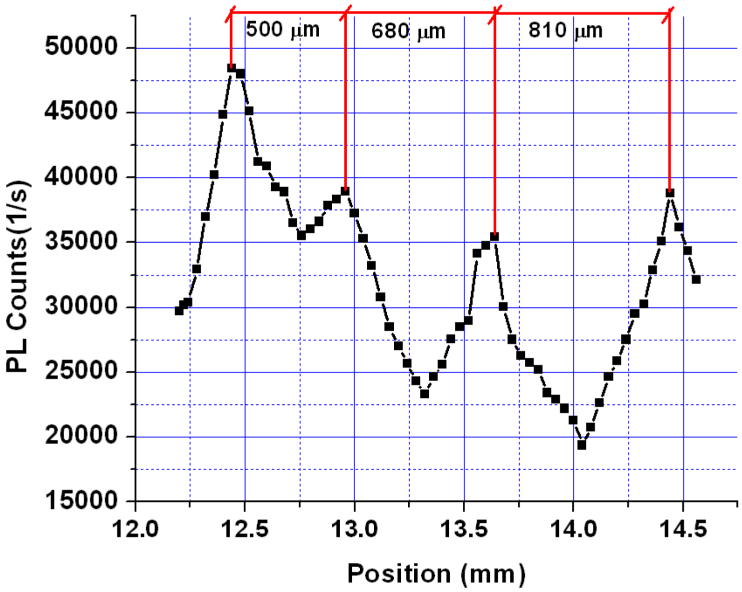

(b)

Figure 3-18. Distribution of charged F-center defects in the bulk samples: (a) polarized LNO-P, and (b) unpolarized LNO-U. The PL spectra are recorded parallel to the z-axis. The periodicity in LNO-P lies between 280 μm and 360 μm. The periodicity in LNO-U lies between 500 μm and 810 μm.

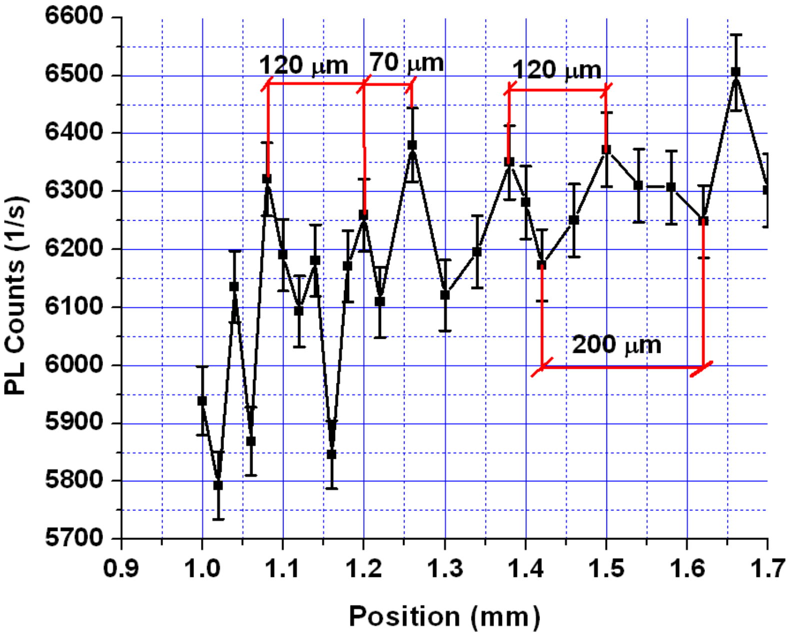

Figure 3-19. Distribution of the antisite (Nb_{Li}^{4+}) point defects in the sample YZ-LNO-Wafer-2. The PL spectra are recorded in a direction parallel to the z-axis. The periodicity is a few hundred microns.

Another impurity that exhibits significant peaks and valleys is Ba. Although Ba is a neutral atom, it is big in size with an atomic number 56. Thus the outer electrons are loosely bound and can easily contribute to electrical conduction on application of an electric field. The presence of Ba have been found to affect the electrical conductivity of the perovskite $LaInO_3$[125] and the double perovskite Sr_2TiMoO_6[126]. Due to its large size, the presence of Ba impurities also create local strains in LN which may influence acoustical propagation through the crystal. Figure 3.20 (a) and (b) show the distribution of Ba impurities in the bulk samples. Figure 3-21 shows the distribution of Ba impurities in YZ-LNO-Plate. The priodicity *P* for Ba is similar to the periodicity of Fe^+ and F-center defects.

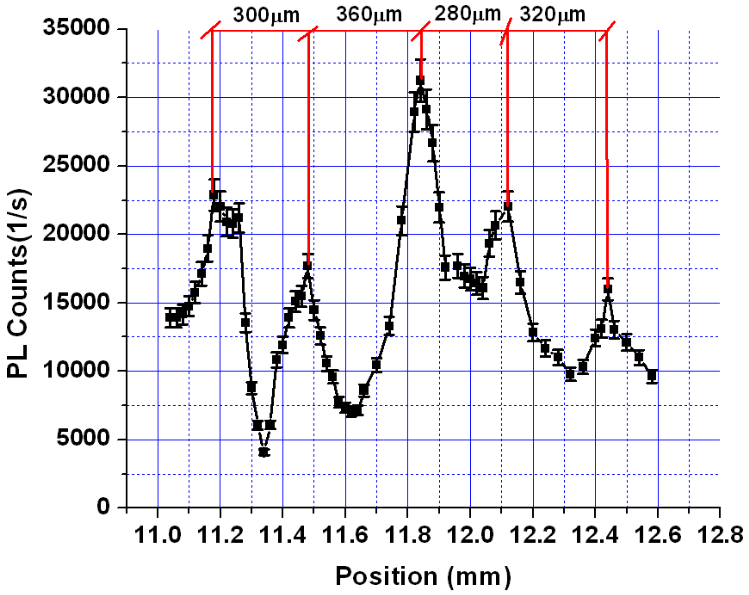

(a)

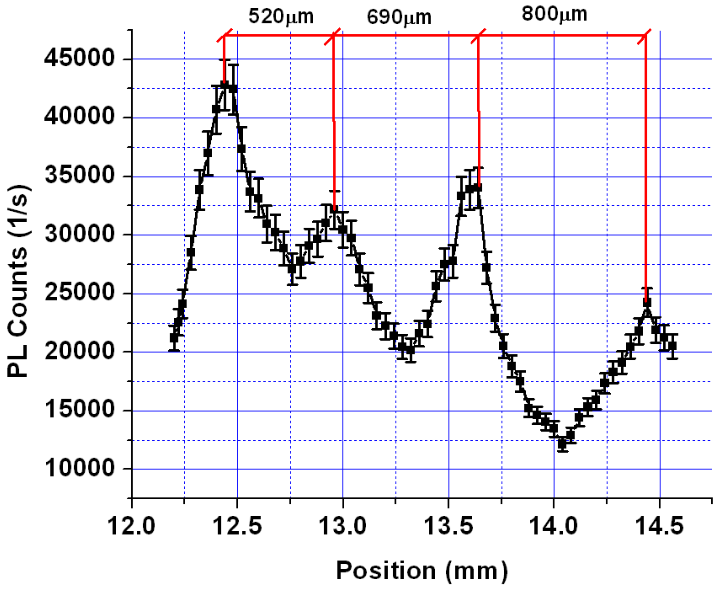

(b)

Figure 3-20. Distribution of Ba impurities in the bulk samples: (a) polarized LNO-P, and (b) unpolarized LNO-U. The spectra are recorded in a direction parallel to the z-axis. The periodicity in LNO-P lies between 280 μm and 360 μm. The periodicity in LNO-U lies between 520 μm and 800 μm.

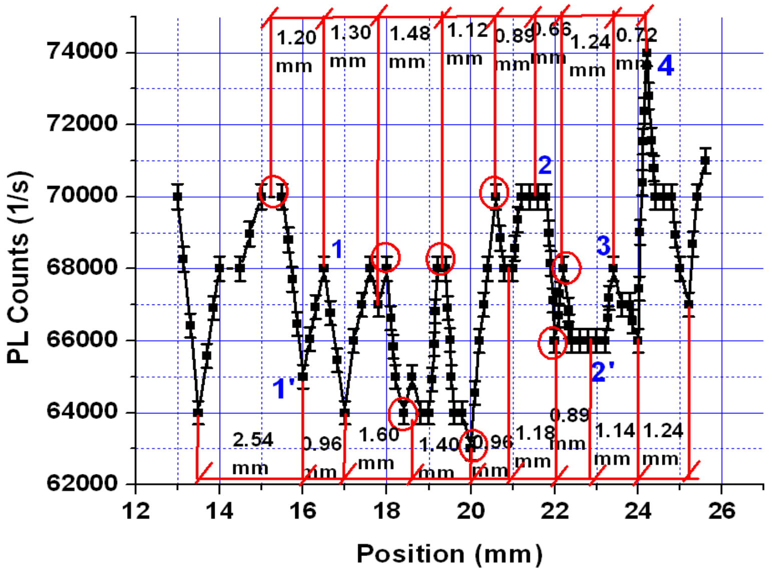

Figure 3-21. Distribution of Ba impurities in YZ-LNO-Plate, when the spectra are recorded in a direction parallel to the z-axis. The points 1, 2…1',2' and the points circled in red with be compared with the electromechanical transformation of LN in Section 4-1.

3.6 Distribution of Impurities in Lithium niobate in a Direction Perpendicular to the z-axis

The spectra of PL were recorded at intervals of tens of microns in a direction perpendicular to the optical crystallographic z-axis. This optical scanning allows to find a distribution of the impurities in the samples. The sample used was a ZX-PPLN, the measurements were made at room temperature. The electrically active defects such as F-center and Fe^+ are expected to be sensitive on a local electric polarization. PPLN is a ferroelectric phononic crystal (FPC) in which the ferroelectric neighboring domains are inversely poled and have an opposite electric polarization. The change from polarization "up" to polarization "down" happens across so called interdomain wall. The point defect concentrations along the neighboring domains are researched by PL-scanning, consisting of taking PL-spectra from narrow zones across the domain structure along the x-axis. The data from the PPLN is compared with a single crystal (SC) ZX-LNO-Wafer-1. The distribution of Ne impurities in ZX-LNO-Wafer-1 is already shown in Figure 2-11. It is observed that the PL distribution along the sample is not periodic, but stochastic. The spread in PL intensity is low, equal to ±1.9% from the average PL intensity (I_{avg}(Ne)). Figure 3-22 shows the distribution of noble gas impurities in ZX-PPLN. The distribution of Ne defects in ZX-PPLN exhibits peaks and valleys. The PL distribution along the sample is periodic and coincides with the domain length of 0.45 mm. The spread in PL intensity for Ne defect in the periodically poled crystal is ±45.3% from the average ($I_{PP,avg}$(Ne)). Thus the change in PL intensity in ZX-PPLN is about 24 times higher than the single crystal.

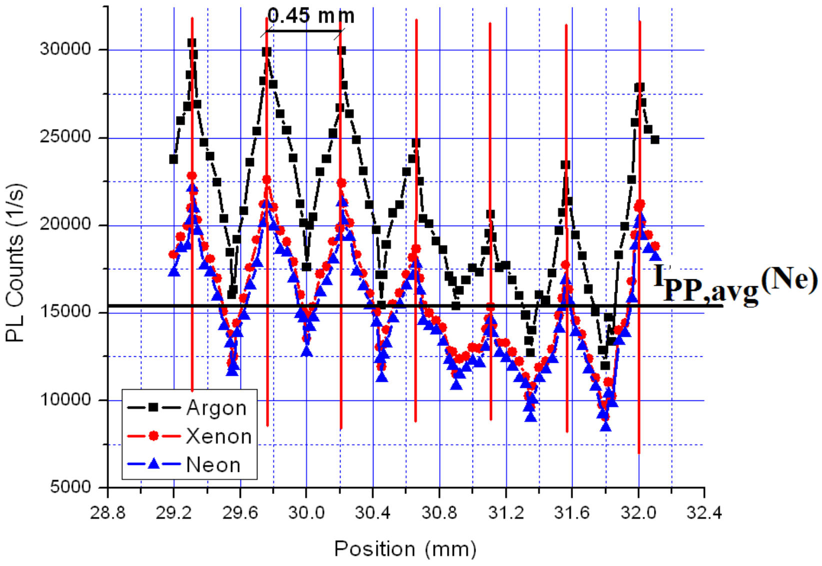

Figure 3-22. Distribution of noble gas Ar, Xe and Ne impurities in ZX-PPLN. The periodicity is 0.45 mm which is the length of a domain in PPLN. The vertical red lines show the position of the inter-domain walls.

The distribution of the charged Fe^+ defect in SC ZX-LNO-Wafer-1 is presented in Figure 3-23 (a). The PL distribution is stochastic along the sample. The spread in PL intensity is ±7.1%

from the average PL intensity (I_{SC},avg(Fe^+)). The distribution of Fe^+ defects in ZX-PPLN exhibits peaks and valleys as shown in Figure 3-23 (b). The PL distribution along the sample is periodic and coincides with the domain length of 0.45 mm. The spread in PL intensity is ±47.8% from the average (I_{PP},avg(Fe^+)), which is about 7 times higher than the single crystal. It can also be observed that the peaks due to the Fe^+ defects in PPLN are very sharp. This is because the internal dipole moments in the domains repel the charged Fe^+ defects, which are localized mainly near the interdomain walls. Thus the peaks represent the location of the interdomain walls. Therefore it can be concluded that there exists a distribution of charged Fe^+ defects on the interdomain walls. The distribution of the the Ba defect in the single crystal is presented in Figure 3-24 (a). The PL distribution is stochastic along the sample. The spread in PL intensity is ±3.2% from the average PL intensity (I_{SC},avg(Ba)). The distribution of the Ba defect in ZX-PPLN exhibits peaks and valleys as shown in Figure 3-24 (b). The PL distribution along the sample is periodic and coincides with the domain length of 0.45 mm. The spread in PL intensity in ZX-PPLN is ±45.2% from the average (I_{PP},avg(Ba)), which is about 14 times higher than the single crystal. The neutral Ba defects are localized mainly near the interdomain walls. The distribution of the F-center defects in the single crystal is presented in Figure 3-25 (a). The PL distribution is stochastic along the sample. The spread in PL intensity for the single crystal is ±8.6% from the average (I_{SC},avg(F)). The distribution of the F-center defect in ZX-PPLN exhibits peaks and valleys as shown in Figure 3-25 (b). The PL distribution along the sample is periodic and coincides with the domain length of 0.45 mm. The spread in PL intensity is ±49.0% from the average (I_{PP},avg(F)), which is about 6 times higher than single crystal. The F-center defects are localized near the interdomain walls.

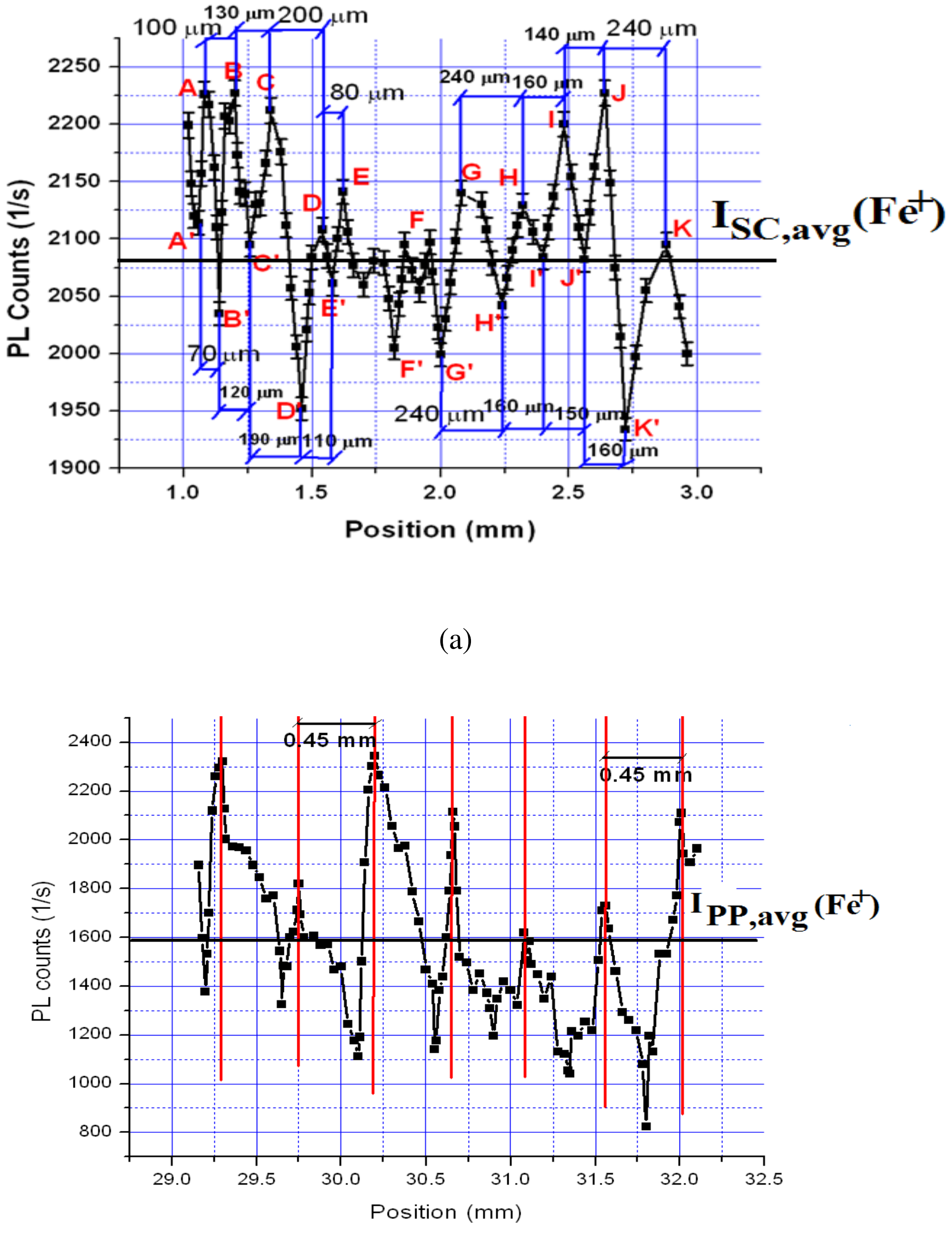

(a)

(b)

Figure 3-23. Distribution of charged Fe^+ impurities in: (a) single crystal ZX-LNO-Wafer-1. Thepoints A, B,…A', B',… will be compared with the electromechanical transformation in Section4-1. (b) ZX-PPLN. The vertical red lines represent the position of the interdomain walls.

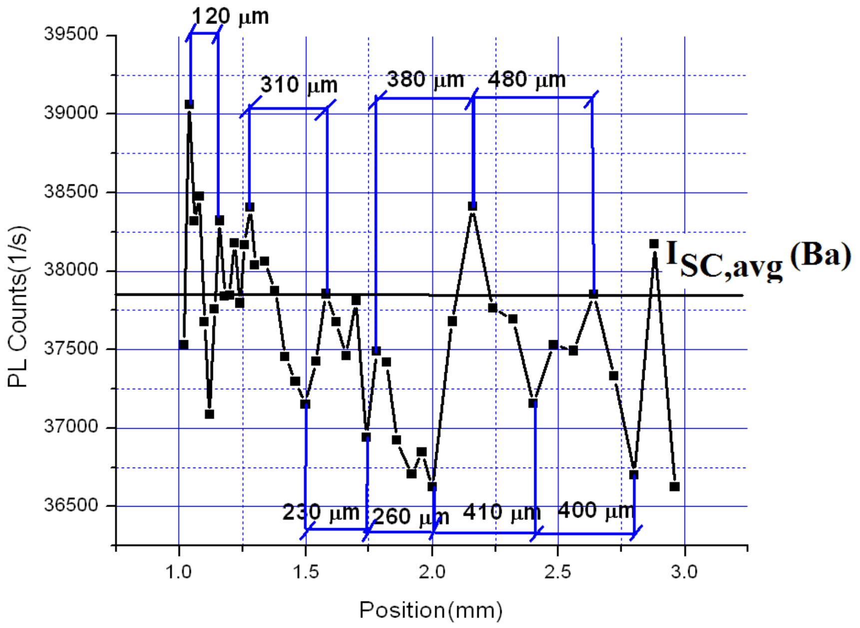

(a)

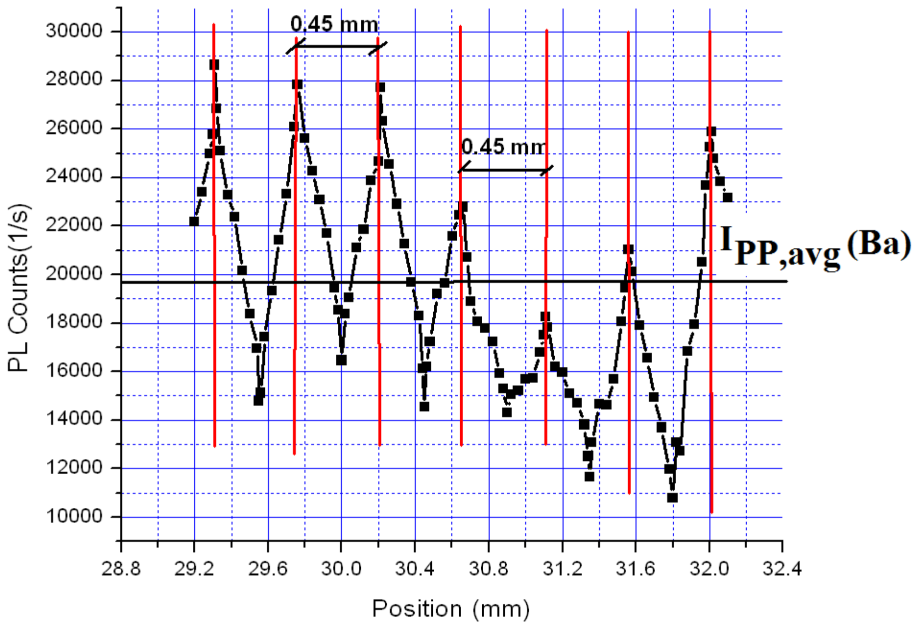

(b)

Figure 3-24. Distribution of Ba impurities in: (a) Single crystal ZX-LNO-Wafer-1, (b) ZX-PPLN. The periodicity is 0.45 mm which is the length of a domain in PPLN. The vertical red lines represent the position of the interdomain walls.

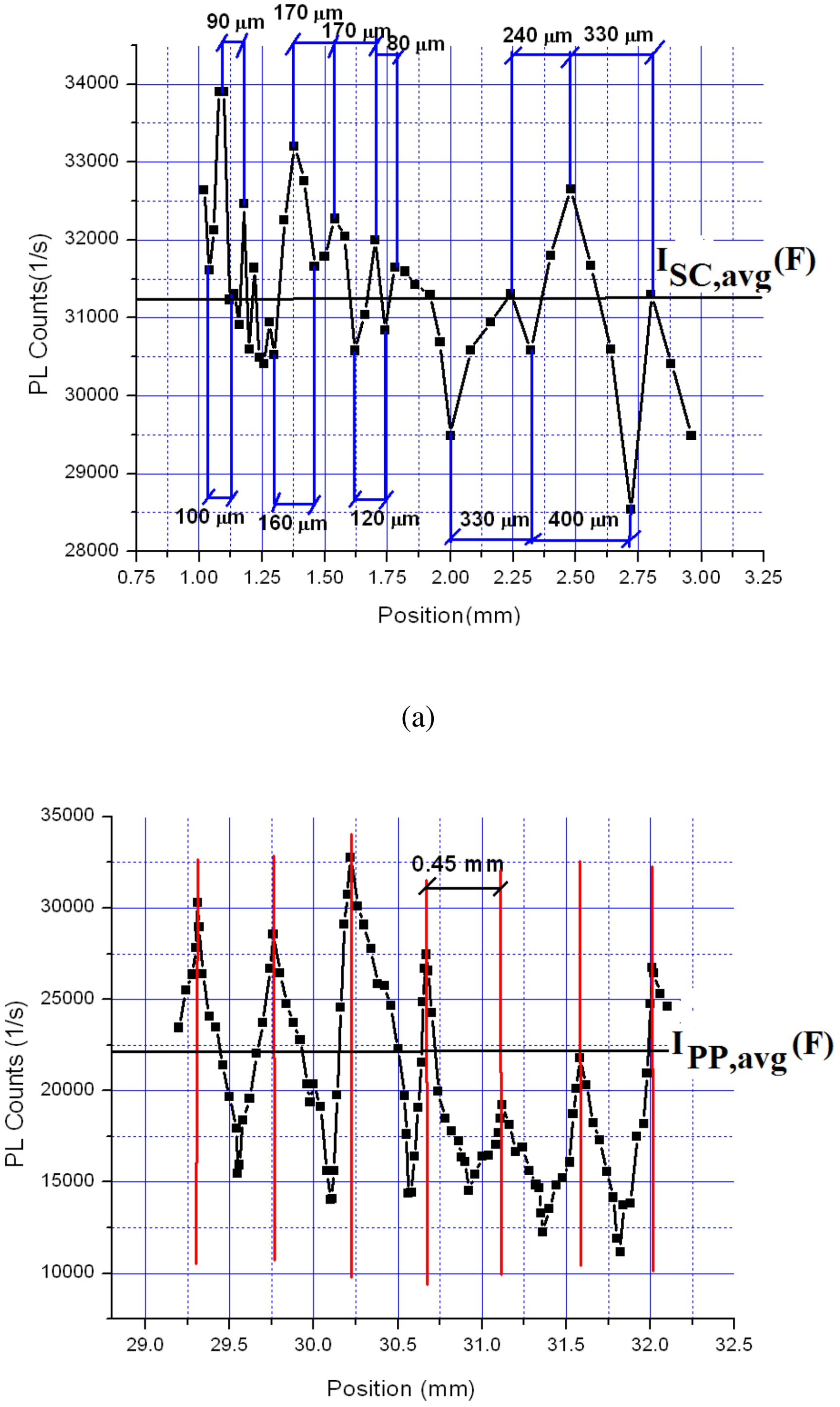

(a)

(b)

Figure 3-25. Distribution of F-center defects in: (a) Single crystal ZX-LNO-Wafer-1, (b) ZX-PPLN. The periodicity is 0.45 mm which is the length of a domain in PPLN.The vertical red lines represent the position of the interdomain walls.

It can be concluded that the distribution of point defects is nonuniform in both PPLN and SCLN; it reveals maxima and minima. The distribution of point defects in PPLN has a periodicity equal to the domain length. The point defects are localized mainly near the interdomain walls, the distribution of defects at these locations show maxima. Change in PL intensity in PPLN is much higher than SCLN, 24 times higher for noble gas defects. Overall, the distribution of point defects in PPLN is a periodic one and in SCLN it is a pure stochastic. The engineering applications of these findings may be non-destructive characterization of the phononic crystals.

3.7 Identification and Distribution of Impurities in Lithium tantalate

Lithium tantalate ($LiTaO_3$, abbreviated as LT) is a perovskite crystal with a similar structure to LN. It has unique piezoelectric and ferroelectric properties with applications in nonlinear optics[127], infrared sensors[128], terahertz detectors[129], cell phones[130], optical waveguides[131] and SAW substrates[132], and others. LT, like LN grown by the Czochralski method. Some advantages of using LT over LN is that it exhibits chemical and mechanical stability over a wider range of temperature than LN (melting point of LT = 1650^0C[133], melting point of LN = 1250^0C). Due to the similarity in growth technology, both crystals contain impurities and point defects. Figure 3-26 shows the PL spectra for LT at an excitation wavelength of 310 nm. The sample used was a Z-cut single crystal LT wafer (SC-Z-LT) with dimensions 10 mm x 10 mm x 0.5 mm. It is observed that the excitation of 310 nm excites the maximum number of impurities. Besides, the PL peaks of the excited impurities are well resolved at this excitation wavelength. The impurities are identified using reference 114, and are grouped as noble gases (Xe I, Ar I, Ne II and Ar II), non-metals (N I and S I) and (Th I, Fe II and Fe I). The presence of radioactive Th may be attributed to the use of LT in pyroelectric nuclear fusion[134]. The distribution of impurities in LT was investigated using SC-Z-LT and a periodically poled sample ZX-PPLT. Figure 3-27 schematically represents the sample ZX-PPLT.

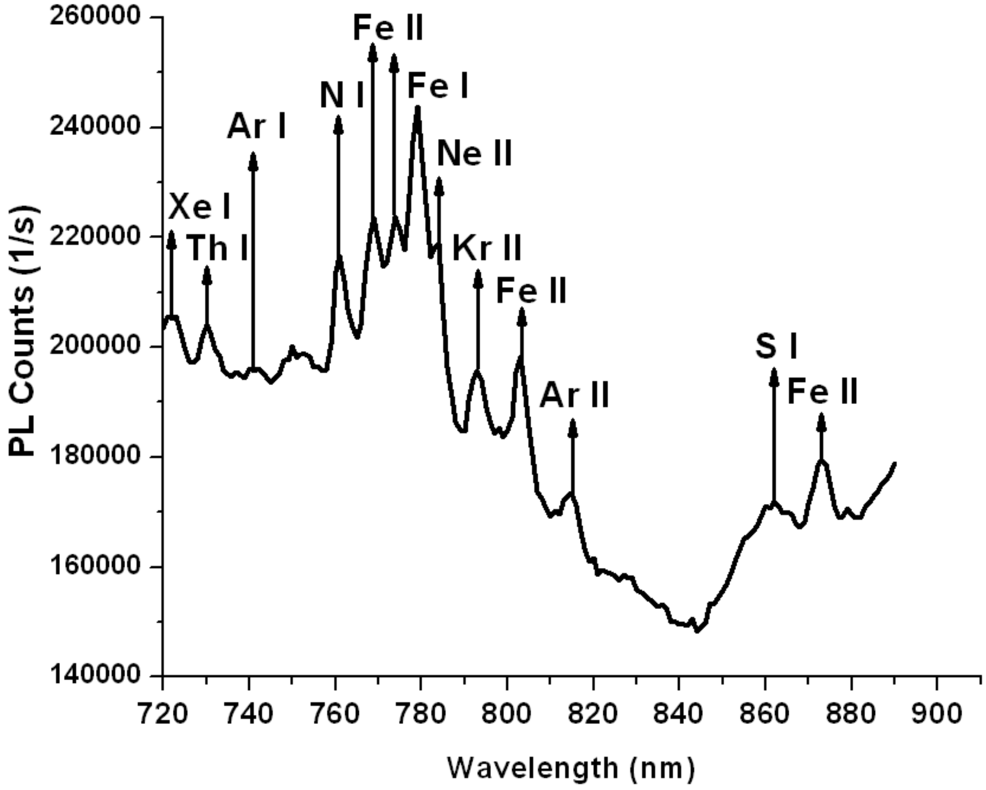

Figure 3-26. PL emission spectrum of single crystal Lithium tantalate (SC-Z-LT) at an excitation wavelength of 310 nm. The slit widths were fixed at 0.5 nm.

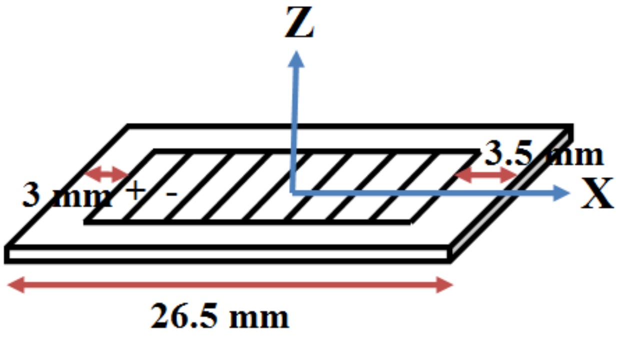

Figure 3-27. Schematic diagram of the sample ZX-PPLT. The inversely poled domains are shown as + and -. Each domain (+ or -) has a width of 1 mm.

As the sample (ZX-PPLT) is moved in steps of a hundred microns, it is observed that the PL counts for the noble gas impurity change by several times in comparison to SC-Z-LT. Figure 3-28 shows the distribution of Kr impurities in SC-Z-LT and ZX-PPLT. The PL distribution along the single crystal sample is stochastic. The spread in PL intensity for SC-Z-LT is ±0.12% from the average (I_{SC},avg(Kr)), as shown in Figure 3-28 (a). The spread in PL intensity in SC-Z-LT is about 16 times less than SC-Z-LN (which is discussed in section 3.6). The distribution of Kr impurities in ZX-PPLT reveals peaks and valleys as shown in Figure 3-28 (b). The PL distribution along the sample is periodic and coincides with the domain length of 1.00 mm. The spread in PL intensity for Kr impurity in the periodically poled crystal is ±15.79% from the average (I_{PP},avg(Kr)). The spread in PL intensity in ZX-PPLT is about 3 times less than SC-Z-LN for Kr(which is discussed in section 3.6). The change in PL intensity in ZX-PPLT is about 132 times higher than SC-Z-LT.

Figure 3-29 shows the distribution of Fe^+ impurities in SC-Z-LT and ZX-PPLT. Unlike the Kr distribution in Figure 3-28 (a), the PL distribution along the single crystal sample is not stochastic. The distribution reveals prominent peaks and valleys with periodicity ranging between 120 μm to 240 μm, this is one point of difference between the Kr and Fe^+ impurities in SC-Z-LT. The spread in PL intensity for SC-Z-LT is ±18.03% from the average (I_{SC},avg(Fe^+)), as shown in Figure 3-29 (a). The spread in PL intensity in SC-Z-LT is about 3 times more than SC-Z-LN (which is discussed in section 3.6), this is a second point of difference between Kr and Fe^+ impurities in SC-Z-LT. The distribution of Fe^+ impurities in ZX-PPLT reveals peaks and valleys as shown in Figure 3-29 (b). The PL distribution along the sample is periodic and coincides with the domain length of 1.00 mm. The spread in PL intensity for the Fe^+ impurity in the periodically poled crystal is ±12.79% from the average (I_{PP},avg(Fe^+)). The spread in PL intensity in ZX-PPLT is about 3.7 times less than SC-Z-LN, for Fe^+ (which is discussed in section 3.6). The change in PL intensity in ZX-PPLT is about 1.4 times lower than SC-Z-LT, which is a point of difference between ZX-PPLN and ZX-PPLT crystals.

A crucial point of difference between ZX-PPLT and ZX-PPLN is the position of the domain walls. While in PPLN, domain walls are located at the location of the peaks in the distribution of point defects (figures 3-23, 3-24 (b), 3-25 (b), 3-26 (b)), in PPLT thy are slightly displaced from the valleys by a hundred micron. The bold blue lines show the location of the domain walls in Figures 3-28 (b) and 3-29 (b). The Ta atom (atomic number 73) in LT is heavier than the Nb atom (atomic atom: 41) in LN, it has 28 more electrons than Nb. So it repels the the impurity atoms, which are pushed away from the ferroelectric domain walls. Thus unlike LN, the domain walls in LT are found near regions where the concentration of impurities are a minimum. The shift in position of the wall from the exact minima may be caused by distortion of the O octahedron by the large Ta atom, which may attract a few charged point defects.

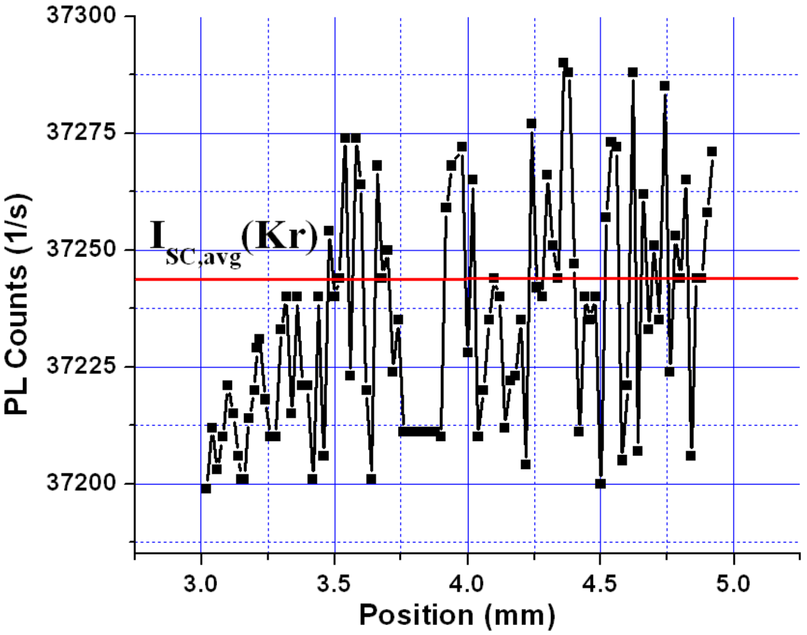

(a)

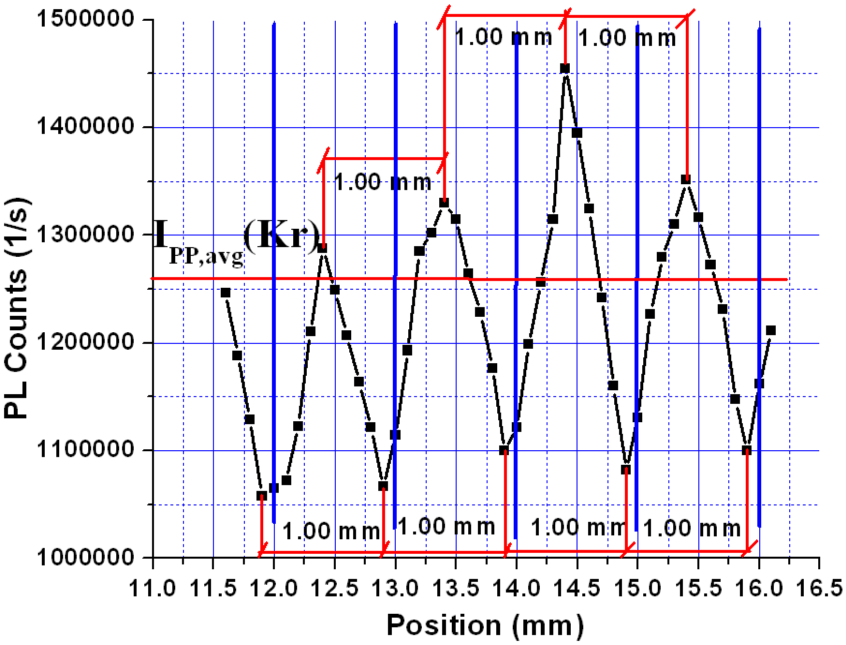

(b)

Figure 3-28. Distribution of Kr noble gas impurities in (a) SC-Z-LT, (b) ZX-PPLT. The vertical blue lines in bold, represent the position of the interdomain walls. The periodicity is 1.00 mm which is the domain length in PPLT. However the location of the domain wall is near a valley, unlike PPLN.

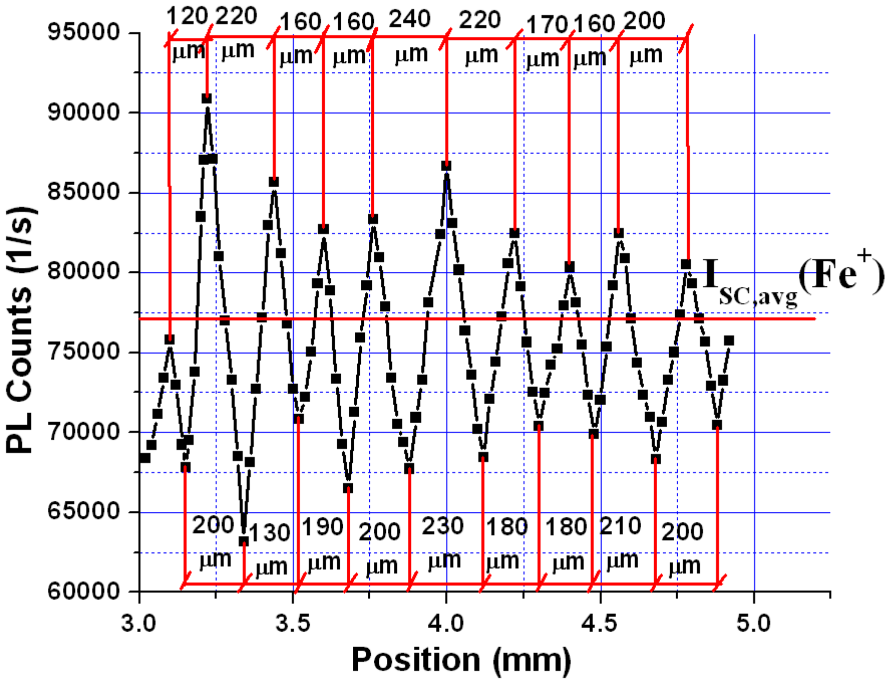

(a)

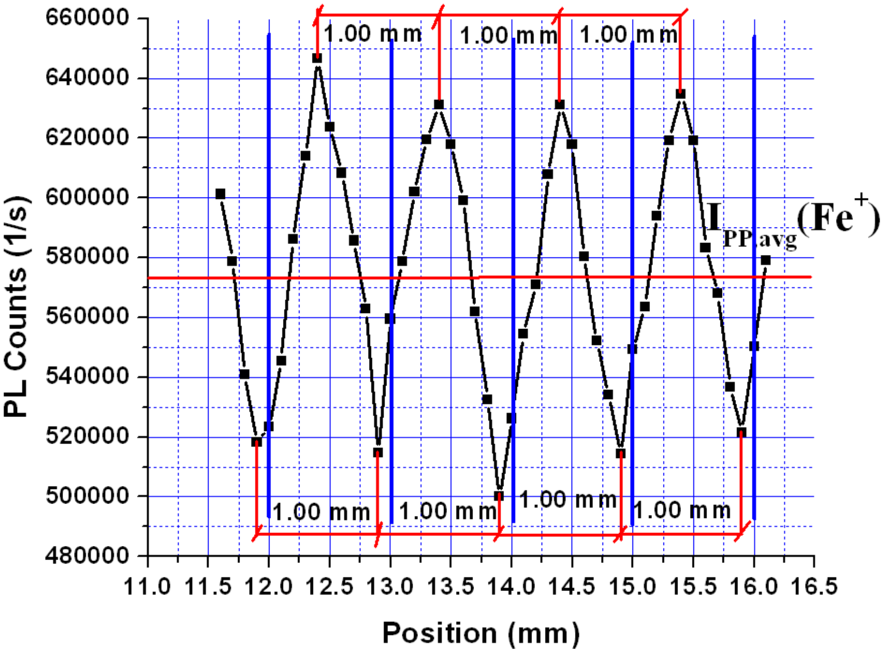

(b)

Figure 3-29. Distribution of charged Fe^+ impurities in (a) SC-Z-LT, (b) ZX-PPLT. The vertical blue lines in bold, represent the position of the interdomain walls.The periodicity is 1.00 mm which is the domain length in PPLT. However the location of the domain wall is near a valley, unlike PPLN.

CHAPTER IV

EFFECT OF IMPURITIES ON ACOUSTO-ELECTRIC PROPERTIES OF LITHIUM NIOBATE

This chapter investigates the effect of the impurities on the acousto electric properties of LN. The electromechanical transformation (EMT) of LN is studied and its distribution in the crystal is plotted. The relationship between the EMT and distribution of impurities (DI) is explained. The acousto-electric admittance is investigated and the connection between the admittance and the periodicity of the impurities is established. The revealed correlation between the DI and EME along with their nonuniform distribution forms the physical basis of nonlinear phenomena involving piezoelectriciry including nonclassical nonlinearity, acoustical memory etc.

4.1 Nonuniform Distribution of Electremechanical Transformation from Lithium niobate

The distribution of EMT parallel to the z-axis is shown in Figure 4-1, for the sample YZ-LNO-Plate. A constant mechanical force is applied to different points on the crystal as discussed in Section 2.7. The EMT reveals a nonuniform distribution with peaks and valleys. The location of the peaks and valleys are in agreement between the distribution of EMT and the DI. For instance, the peaks labelled as A, B, C …F in the EMT distribution in Figure 4-1, coincide with the position of the peaks in the distribution of Fe^{+} defects as shown in Figure 3-16 (a). The valleys labelled as A’, B’, C’ …H’ in the EMT distribution in Figure 4-1, coincide with the position of the valleys in the distribution of Fe^+ defects as shown in Figure 3-16 (a). The peaks 1,2, 3 and 4, and the valleys 1' and 2' in the EMT distribution coincide with the position of the peaks and valleys in the distribution of Ba defects, as shown in Figure 3-21. Thus higher the concentration of point defects, higher is the EMT, and lower the concentration of point defects, lower is the EMT, in a direction parallel to the z-axis. The distance between consecutive peaks and valleys in the EMT distribution lie within 0.66 mm and 2.72 mm, which is similar to the range of periodicities in the DI.

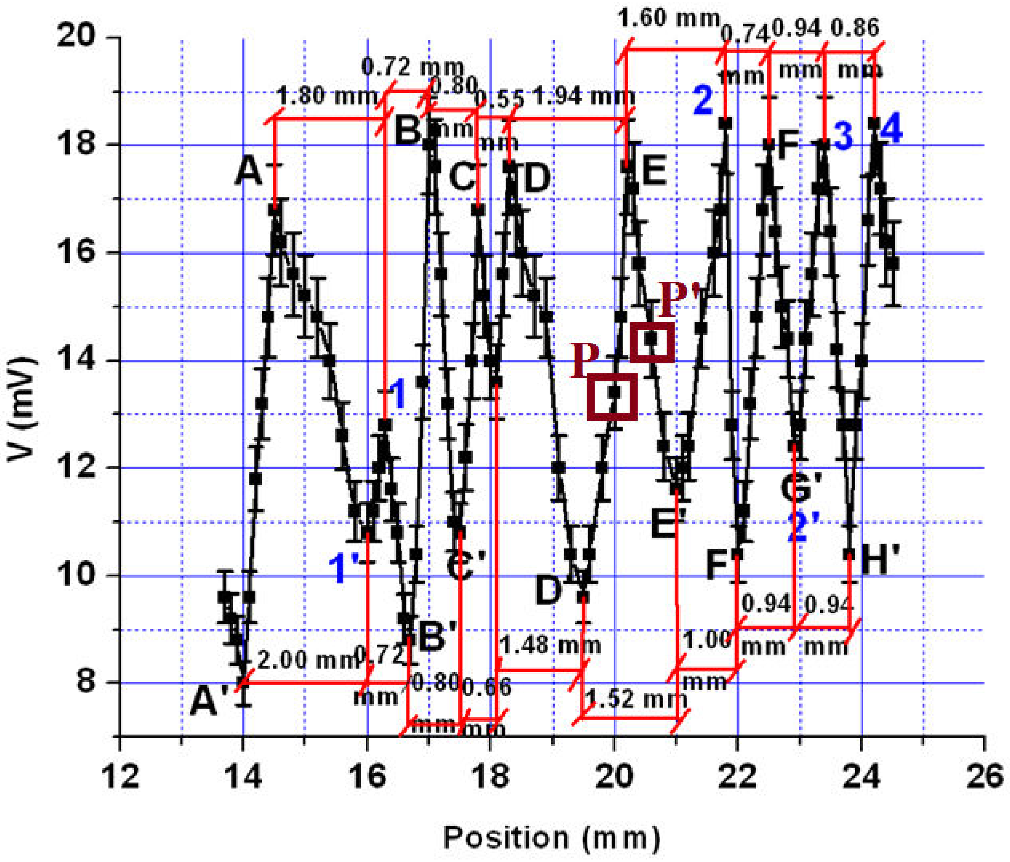

Figure 4-1. Distribution of EMT in YZ-LNO-Plate in a direction parallel to the z-axis, at room temperature. The distribution is nonuniform and reveals peaks and valleys. The points A, B, C...... and A', B', C'......... coincide with the exact location of the peaks and valleys of the Fe^+ distribution in Figure 3-16 (a), while the points 1, 2, 3, 4 and 1', 2' coincide with the exact location of the peaks and valleys of the Ba distribution in Figure 3-21.

Figure 4-2 shows the distribution of EMT in the sample ZX-LNO-Wafer-1. It can be observed that the peaks denoted by A, B, C, D….K coincide with the exact location of the peaks in the Fe^+ DI in Figure 3-23 (a). The valleys A', B'…..K' coincide with the exact location of the valleys in the Fe^+ DI in Figure 3-23 (a). Thus higher the concentration of point defects, higher is the EMT, and lower the concentration of point defects, lower is the EMT, in a direction normal to the z-axis. The distance between consecutive peaks and valleys in the EMT distribution lie within 70 μm and 240 μm, which is similar to the range of periodicities in the Fe^+ DI in Figure 3-23 (a).

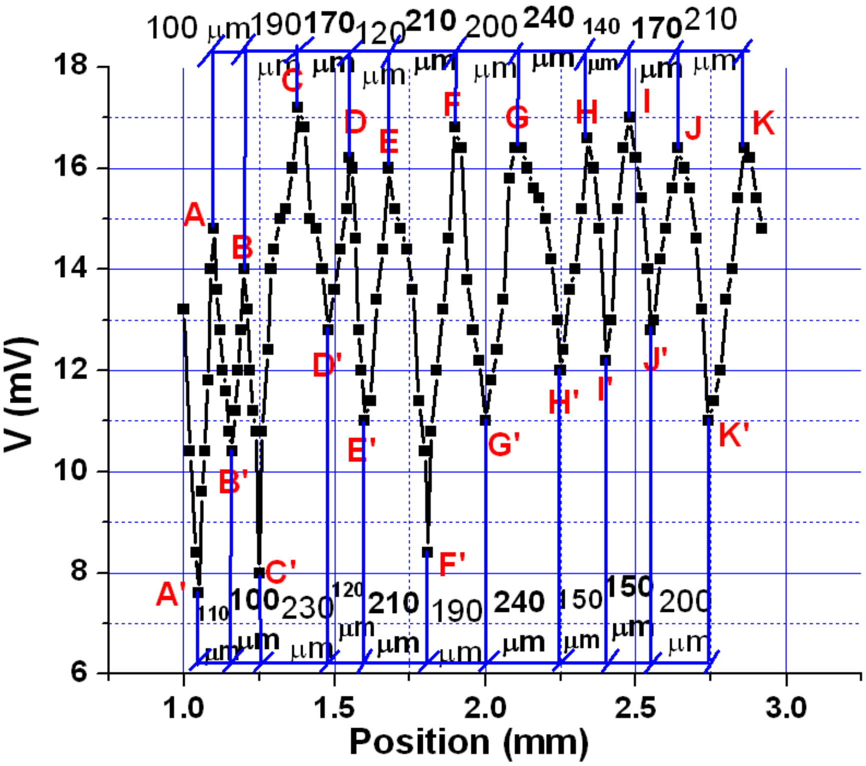

Figure 4-2. Distribution of EMT in ZX-LNO-Wafer-1 in a direction normal to the z-axis, at room temperature. The points A, B, C...... and A', B', C'......... coincide with the exact location of the peaks and valleys of the Fe^+ distribution in Figure 3-23 (a).

Figure 4-3 shows a typical output signal generated, when the hammer makes an impact with YZ-LNO-Plate. The oscillogram is generated at the point A in Figure 4-1. In Figure 4-3, the time difference (Δt) between the first two peaks is equal to 64 μs. The frequency $F = \frac{1}{\Delta t} =$ 15.62 KHz, the velocity of the mode excited is $v = F.P$ =15.62 KHz x 2.54 mm= 39.67 m/s. The ratio $\frac{v}{v_T} = 0.011$, where the velocity (v_T) of the transverse acoustical wave in LN is 3590 m/s. The mode excited is the plate A_0 mode. Therefore, it may be concluded that electromechanical transformation by mechanical impact to ultrasonic mode generates electrical voltage. Moreover, time difference between the first two peaks of the oscillogram is directly connected to the periodicity of the point defects and impurities.

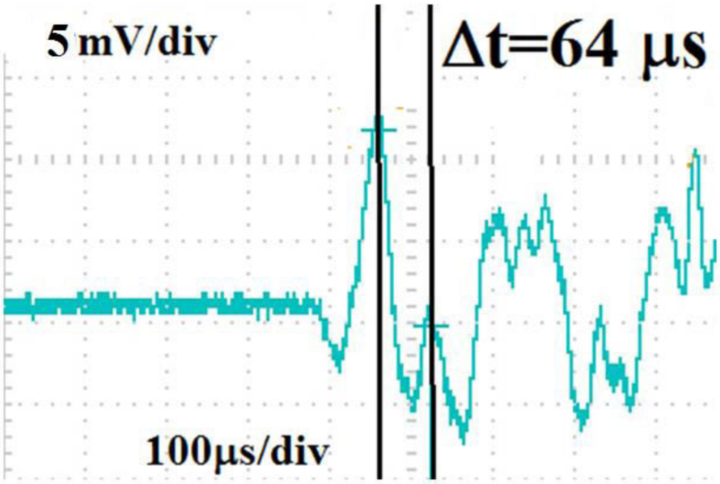

Figure 4-3. Oscillogram generated due to impact of the plastic hammer with the crystal YZ-LNO-Plate, at room temperature.

The impact of the plastic hammer with the sample generates a signal. It is observed that when V rises from a valley to a peak (DE in Figure 4-1), the first signal of the oscillogram is a peak, as shown in Figure 4-4 (a). When V drops from the peak to a valley (EE' in Figure 4-1), the first signal of the oscillogram is a valley, as shown in Figure 4-4 (b).

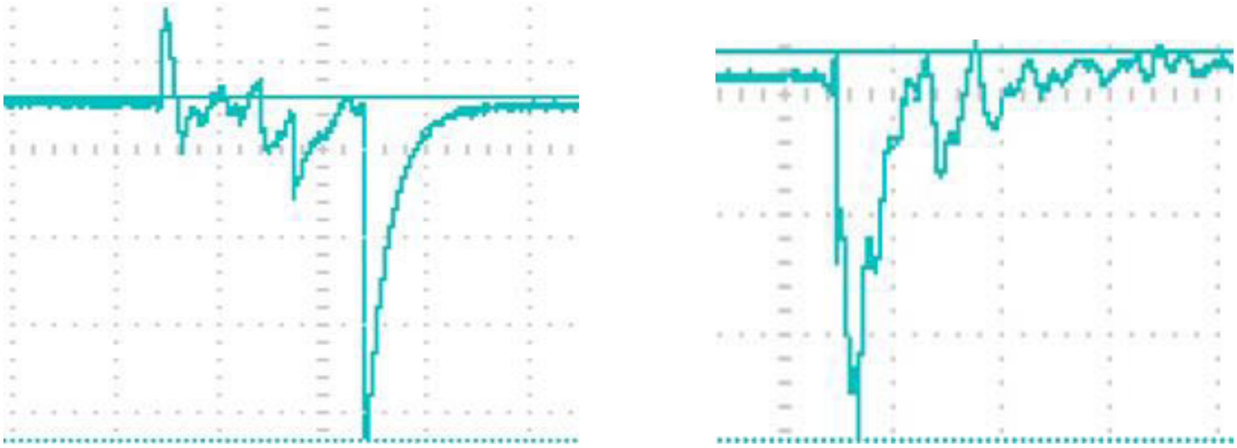

(a) (b)

Figure 4-4. Oscillograms generated by impact of plastic hammer with YZ-LNO-Plate. (a) Oscillogram generated at the point P of Figure 4-1, (b) oscillogram generated at the point P' of Figure 4-1.

LN belongs to the points group 3m. The non-zero components (ij) of the piezoelectric tensor for point group 3m is given by

$$e = \begin{bmatrix} 00 & 00 & 00 & 00 & 15 & -22 \\ -22 & 22 & 00 & 15 & 00 & 00 \\ 31 = 32 & 32 = 31 & 33 & 00 & 00 & 00 \end{bmatrix} \qquad (4.1)$$

In order to determine the distribution of EMT in YZ-LNO-Plate for instance, a stress is applied parallel to the y-axis, while the DPD is measured parallel to the z-axis. The electromechanical coupling coefficient related to the experimental configuration is k_{32}, where $k_{32} = 2.21\%$ [135]. k_{32} is related to the piezoelectric tensor by the equation

$$k_{32}^2 = \frac{e_{32}^2}{\varepsilon_{33} c_{22}} \tag{4.2}$$

where ε_{33} is the component of the dielectric permittivity tensor and c_{22} is the component of the elastic modulus tensor. The electromechanical coupling coefficient (k) is assumed to be constant throughout the length of the crystal, the influence of the DPD on k has not yet been investigated. k is modelled by the following function:

$$k = k_0 + k_d \cos(\frac{2\pi.z}{P}) \tag{4.3}$$

where k_0 is the part of the electromechanical coupling coefficient without the influence of point defects and is a constant. k_d is the part of the electromechanical coupling coefficient influenced by the DPD. The peak and valley nature of the DPD along the z-axis is taken into account by the cosine function. The different periodicities of the point defects (P) superpose to generate a distribution of k parallel to the z-axis. Figure 4-5 shows a plot of k for the Fe^+ and Ba point defects using equation (4.3). The peaks A, B, and F, and the valleys A' through G' in Figure 4-5(a) coincide with the exact locations of the peaks and valleys in the Fe^+ DI in Figure 3-16(a). The peaks 1, 2, 3, the valleys 1', 2', along with those that are encircled in red, coincide with the exact locations of the peaks and valleys of the Ba DI in Figure 3-21. Thus higher concentration of point defects leads to higher values of k and vice-versa. It may be observed that k_{Ba} shows more coincidence with the peaks of the DPD than k_{Fe^+}, in the region between 18 mm to 21.5 mm. This is related to the polarizability of the oxygen atom[136]. Since Ba is more than two times heavier than Fe, it would polarize the O atoms around it to a greater extent than Fe^+. The O octahedron around Ba is more distorted than around Fe^+, higher the concentration of Ba, more is the distortion.

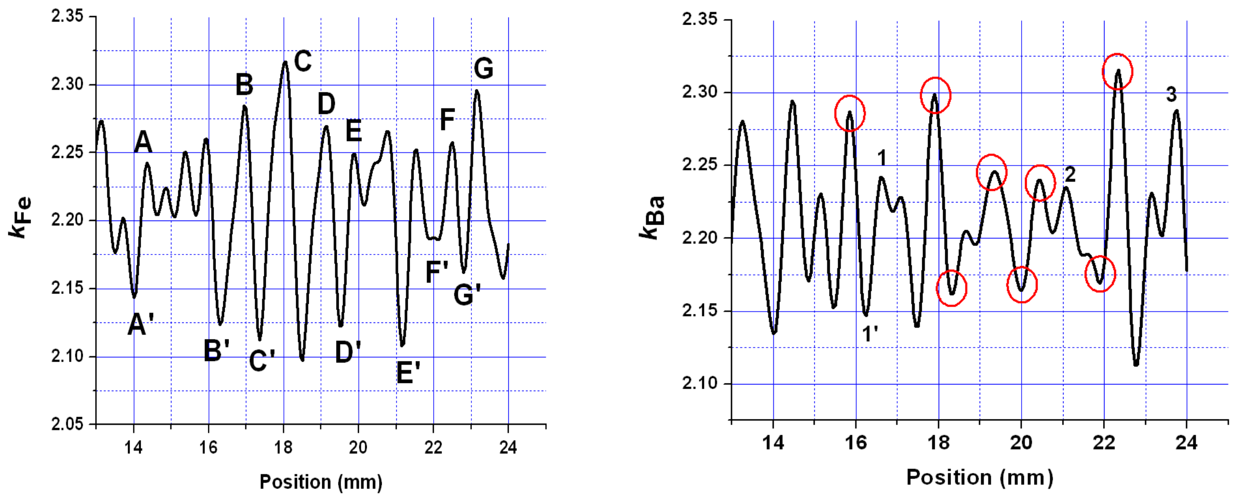

(a) (b)

Figure 4-5. Correlation between the electromechanical efficiency and the impurities (a) Fe^+ and (b) Ba, in YZ-LNO-Plate.

4.2 Investigation of Radio frequency (r-f)Admittance of Lithium niobate

The ferroelectric crystals particularly those fabricated from LN and Lithium tantalate (LT) are widely used for applications telecommunications, ultrasonics, acousto-optics for laser technology and others[137]. The megahertz and higher frequency ranges are usually used in telecommunications including cell phones. That is why one needs to investigate the properties of LN at those frequencies. For LN samples in the form of plates, ususally one dominant acoustic displacement is considered along a certain crystallographic axis. However, in real applications such as ultrasonic transducers, electromechanical actuators, radio-frequency filters, acousto-optic devides and others, none of the dimensions are of infinite order. Thus for theoretical and experimental research, it is recommended that all three directions are taken into account so that the results are closest to real applications[137]. One of the reasons is a high Poisson's ratio for solids varying between 0.2 to 0.4 for different materials[137]. LN has a Poisson's ratio of 0.25, which implies a displacement of 25% in the normal directions with respect to an original axis along which a 100% displacement is introduced. The important consequence of such vibrations is actually a three dimensional character of the acoustical displacement in LN. The three dimensional vibrational components with all three amplitude components in the X, Y and Z axes may in turn be a basis for new solid state devices. For instance, one can point in the direction of a new ultrasonic transducer with variable direction and polarization of the mechanical dispacements.

In piezoelectric materials, there is a strong coupling between electrical and mechanical fields. Therefore, mechanical, electrical and piezoelectric components of energy losses should be included in the characterization. The acousto-electric admittance is sensitive to crystal parameters including electromechanical coupling coefficient (*K*), the phase velocity of the acoustical wave and others. The presence of impurities point defects and their distribution alters some of the parameters including *K*, as discussed in section 4.1. Due to the presence of defects, the relationship between stress and strain is no longer linear. The presence of point defects introduce stress in the crystal which affect the r-f admittance of LN. Section 4.2.1 is dedicated to the theoretical development, of the influence of the microstructure on the r-f admittance. Section 4.2.2 is dedicated to the experimental investigation of the r-f admittance.

4.2.1 Influence of Impurities on the Radio-frequency (r-f) Admittance of Lithium niobate

A YZ-cut piezoelectric LN plate is considered with the electric field paralle to the z-axis, as shown in Figure 4-15. The experimental setup shown in Figure 2-16 is similar to this condition, with the length parallel to the z-direction and the end faces electroded. If the permittivity ε of the bar is sufficiently greater than that of its surroundings to prevent fringing electric fields, electric flux lines will also be parallel to its length, and therefore $D_1 = D_2 = 0$ and $\partial D_3/\partial z = 0$, where D_1, D_2 and D_3 are the three components of the electric displacement vector. The piezoelectric equations for the setup in Figure 4-15 are:

$$S_3 = s_{33}^D T_3 + g_{33} D_3 \tag{4.4a}$$

$$E_3 = -g_{33} T_3 + \beta_{33}^T D_3 \tag{4.4b}$$

The exciting electric voltage is applied along the z-axis. Newton's equation of motion for piezoelectric media describe the motion of the acoustical vibration.

$$\rho \frac{\partial^2 \xi_3}{\partial t^2} = \frac{\partial T_3}{\partial z} \tag{4.5}$$

Substituting equation (4.4a) and recalling that $S_3 = \frac{\partial \xi_3}{\partial z}$, Newton’s equation of motion becomes

$$\rho \frac{\partial^2 \xi_3}{\partial t^2} = \frac{1}{s_{33}^D} \frac{\partial^2 \xi_3}{\partial z^2} \tag{4.6}$$

where ρ is the density of the ceramic. The solution to the wave equation gives particle displacement of the form

$$\xi_3 = \left[A\sin\frac{\omega.z}{v^D} + B\cos\frac{\omega.z}{v^D} \right] \exp(j\omega t) \tag{4.7}$$

where v^D is the velocity of the propagating elastic wave, $v^D = (1/\rho s_{33}^D)^{1/2}$. At the free ends of the bar $(z = 0, L)$ the stress $T_3 = 0$, which is used to evaluate A and B.

$$\xi_3 = \frac{v^D g_{33} D_3}{\omega}[\sin\frac{\omega.z}{v^D} - \tan\frac{\omega.L}{2v^D}\cos\frac{\omega.z}{v^D}] \tag{4.8}$$

where $D_3 = D_0.\exp(j\omega t)$. For convenience, equations (4.4a) and (4.4b) are rewritten as:

$$T_3 = \frac{S_3}{s_{33}^D} - \frac{g_{33}}{s_{33}^D} D_3 \tag{4.9a}$$

$$E_3 = -\frac{g_{33}}{s_{33}^D} S_3 + (\frac{g_{33}^2}{s_{33}^D} + \beta_{33}^T) D_3 \tag{4.9b}$$

Substituting $S_3 = \frac{\partial \xi_3}{\partial z}$

$$E_3 = -\frac{g_{33}^2}{s_{33}^D} D_3[\cos\frac{\omega.z}{v^D} + \tan\frac{\omega.L}{2v^D}.\sin\frac{\omega.z}{v^D}] + (\frac{g_{33}^2}{s_{33}^D} + \beta_{33}^T) D_3 \tag{4.10}$$

Algebraic manipulations of equation (4.10) give

$$\frac{g_{33}^2}{s_{33}^D} + \beta_{33}^T = \beta_{33}^T[1 + \frac{g_{33}^2}{s_{33}^D \beta_{33}^T}] = \frac{1}{\varepsilon_{33}^T}[1 + \frac{k_{33}^2}{1 - k_{33}^2}] \approx \frac{1}{\varepsilon_{33}^T}[1 + k_{33}^2] \tag{4.11}$$

where $\beta_{33}^T = \frac{1}{\varepsilon_{33}^T}$, electromechanical coupling coefficient (ECC) $k_{33}^2 = \frac{g_{33}^2 \varepsilon_{33}^T}{s_{33}^E}$ and $s_{33}^D = s_{33}^E(1 - k_{33}^2)$. The distribution of impurities discussed in section 3.1.6 shows peaks and valleys. The ECC is described by the function:

$$k_{33} = k_0 + k_d . \cos(\frac{2\pi.z}{P}) \tag{4.12}$$

where k_0 is the constant part of the ECC without the influence of point defects and k_d is due to the contricution of the point defects. The peak and valley nature of the distribution of point defects is approximated by the cosine function, where *P* is the periodicity of defects. Substituting equations (4.11) and (4.12) in equation (4.10), gives

$$E_3 = -\frac{D_3 k_0^2}{\varepsilon_{33}^T}[1 + 2\frac{k_d}{k_0}\cos\frac{2\pi.z}{P}].[\cos\frac{\omega.z}{v^D} + \tan\frac{\omega L}{2v^D}.\sin\frac{\omega.z}{v^D}] + \frac{D_3}{\varepsilon_{33}^T}[1 + 2k_0 k_d \cos\frac{2\pi.z}{P} + k_0^2] \tag{4.13}$$

The voltage across the bar is:

$$V = \int_0^L E_3\, dz \tag{4.14}$$

Substituting equation (4.13) in (4.14) gives

$$\begin{aligned} V = &-\frac{D_3 k_0^2}{\varepsilon_{33}^T}[\int_0^L \cos(\frac{\omega.z}{v^D})dz + \tan(\frac{\omega L}{2v^D})\int_0^L \sin(\frac{\omega.z}{v^D})dz + 2\frac{k_d}{k_0}\int_0^L \cos(\frac{2\pi.z}{P}).\cos(\frac{\omega.z}{v^D})dz \\ &+ 2\frac{k_d}{k_0}\tan(\frac{\omega L}{2v^D})\int_0^L \cos(\frac{2\pi.z}{P}).\sin(\frac{\omega.z}{v^D})dz] + \frac{D_3}{\varepsilon_{33}^T}[\int_0^L dz + 2k_0 k_d \int_0^L \cos(\frac{2\pi.z}{P})dz + \int_0^L k_0^2 dz] \end{aligned} \tag{4.15}$$

After evaluating the integrals in equation (4.15)

$$V = \frac{D_3}{\varepsilon_{33}^T}[F_{DF} + F_D] \tag{4.16}$$

where F_{DF} is the defects free function given by

$$F_{DF} = \frac{L}{\varepsilon_{33}^T}(1 + k_0^2) - \frac{k_0^2 v^D}{\omega}[\sin(\frac{\omega L}{v^D}) + \tan(\frac{\omega L}{2v^D}).\{1 - \cos(\frac{\omega L}{v^D})\}] \tag{4.17}$$

It can be observed from equation (4.17) that F_{DF} depends on k_0, which is the defect free part of the electromechanical coupling coefficient. F_D in equation (4.16) contains the influence of the point defects.

$$
\begin{aligned}
F_D = k_0 k_d [\frac{P}{\pi}\sin(\frac{2\pi L}{P}) - 2\left\{ \frac{\sin(\frac{\omega L}{v^D} - \frac{2\pi L}{P})}{2(\frac{\omega}{v^D} - \frac{2\pi}{P})} + \frac{\sin(\frac{\omega L}{v^D} + \frac{2\pi L}{P})}{2(\frac{\omega}{v^D} + \frac{2\pi}{P})} \right\} \\
- 2\tan(\frac{\omega L}{2v^D})\left\{ \frac{2(\frac{\omega}{v^D})}{(\frac{\omega}{v^D})^2 - (\frac{2\pi}{P})^2} - \frac{\cos(\frac{\omega L}{v^D} - \frac{2\pi L}{P})}{2(\frac{\omega}{v^D} - \frac{2\pi}{P})} - \frac{\cos(\frac{\omega L}{v^D} + \frac{2\pi L}{P})}{2(\frac{\omega}{v^D} + \frac{2\pi}{P})} \right\}]
\end{aligned}
\tag{4.18}
$$

The function F_D contains the influence of the point defects and impurities. It is dependent on k_d, the part of the electromechanical coupling coefficient dependent on defects and it depends on P, the periodicity of the point defects and impurities. Equation (4.16) can be re-arranged to obtain an expression for D_3.

$$
D_3 = \frac{V_0 \exp(i\omega t).\varepsilon_{33}^T}{F_{DF} + F_D} \tag{4.19}
$$

where $V = V_0 \exp(i\omega t)$. The r-f current I flowing through the dielectric material is

$$
I = A\frac{\partial D_3}{\partial t} \tag{4.20}
$$

where $A = hw$, A is the area of the capacitor, h is the height of the capacitor and w is the width of the capacitor. The r-f admittance $Y = \frac{I}{V}$ which may be written as

$$Y = \frac{i\omega.hw\,\varepsilon_{33}^{T}}{F_{DF} + F_{D}} \tag{4.21}$$

It can be observed fromequation (4.21) that the denominator contains the sum of the defect free function F_{DF} and the function independent of the influence of point defects and impurities F_D.

When $\frac{L}{P} = n,\ n = 0,1,2,3........$; the first term in equation (4.18) is equal to zero. The second term $(F_D)_2$ in equation (4.18) is simplified as follows:

$$(F_D)_2 = \frac{\sin(\frac{\omega L}{v^D} - 2\pi n)}{2(\frac{\omega}{v^D} - \frac{2\pi n}{L})} + \frac{\sin(\frac{\omega L}{v^D} + 2\pi n)}{2(\frac{\omega}{v^D} + \frac{2\pi n}{L})} \tag{4.22}$$

$$(F_D)_2 = \sin(\frac{\omega L}{v^D}).\left[\frac{1}{2\left(\frac{\omega}{v^D} - \frac{2\pi n}{L}\right)} + \frac{1}{2\left(\frac{\omega}{v^D} + \frac{2\pi n}{L}\right)}\right] \tag{4.23}$$

$$(F_D)_2 = \sin(\frac{\omega L}{v^D}).\left[\frac{\left(\frac{\omega}{v^D}\right)}{\left(\frac{\omega}{v^D}\right)^2 - \left(\frac{2\pi n}{L}\right)^2}\right] \tag{4.24}$$

The third term $(F_D)_3$ in equaion (4.18) is simplified as follows:

$$(F_D)_3 = \frac{2\frac{\omega}{v^D}}{(\frac{\omega}{v^D})^2 - (\frac{2\pi n}{L})^2} - \cos(\frac{\omega L}{v^D}).\left[\frac{1}{2\left(\frac{\omega}{v^D} - \frac{2\pi n}{L}\right)} - \frac{1}{2\left(\frac{\omega}{v^D} + \frac{2\pi n}{L}\right)}\right] \tag{4.25}$$

$$(F_D)_3 = \frac{2\frac{\omega}{v^D}}{(\frac{\omega}{v^D})^2 - (\frac{2\pi n}{L})^2} - \cos(\frac{\omega L}{v^D}).\left[\frac{\left(\frac{2\pi n}{L}\right)}{\left(\frac{\omega}{v^D}\right)^2 - \left(\frac{2\pi n}{L}\right)^2}\right] \tag{4.26}$$

Therefore, when $\frac{L}{P} = n, n = 0,1,2,3.....$

$$F_D = k_0 k_d [-2\frac{\omega}{v^D}.\frac{\sin(\frac{\omega L}{v^D})}{\left(\frac{\omega}{v^D}\right)^2 - \left(\frac{2\pi n}{L}\right)^2}] - 2\tan(\frac{\omega L}{2v^D}).\{\frac{2\frac{\omega}{v^D}}{(\frac{\omega}{v^D})^2 - (\frac{2\pi n}{L})^2} - \frac{2\pi n}{L}.\frac{\cos(\frac{\omega L}{v^D})}{\left(\frac{\omega}{v^D}\right)^2 - \left(\frac{2\pi n}{L}\right)^2}\}$$

(4.27)

It can be observed from equation (4.27) that F_D is independent of the periodicity of point defects and impurities, as shown in Figure 4-6. The frequency dependence of r-f admittance will exhibit point defects with periodicity *P,* such that $\frac{L}{P} \neq n;\ n = 0,1,2\ ....$. This should be demonstrated in experimental measurements of the r-f admittance of LN.

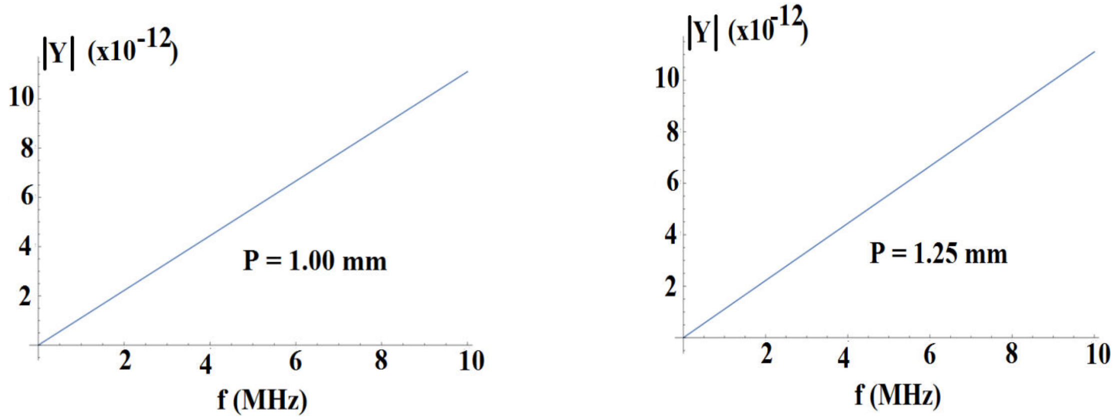

(a) (b)

Figure 4-6. Plot of r-f admittance (Y) versus frequency (f) when the ratio L/P equals an integer n. The length (L) of the sample is 5 cm. So n equals (a) 50 and (b) 40 in the plots.

4.2.2 Experimental Investigation of Radio-frequency Admittance of Lithium niobate

The point defects influence the r-f admittance of YZ-LNO-Plate. Figure 4-7 shows the frequency dependence of the admittance Y as an estimate of the ratio of the peak-to-peak output and input voltages, from 500 KHz to 5.5 MHz. Beyond this region, the r-f admittance increases linearly with the frequency. A resonance-antiresonance curve denoted with 1 is observed at a frequency (F) of 1.76 MHz. The acoustical mode excited has a velocity v, where

$$v = F.2t \tag{4.28}$$

t being the thickness of the plate. The mode excited has a velocity of 6.36 km/s and is identified as the plate S_0 mode. This implies that the strain is non-zero in a direction parallel to the y-axis, leading to a non-zero value of the electromechanical coupling coefficient k_{32}.

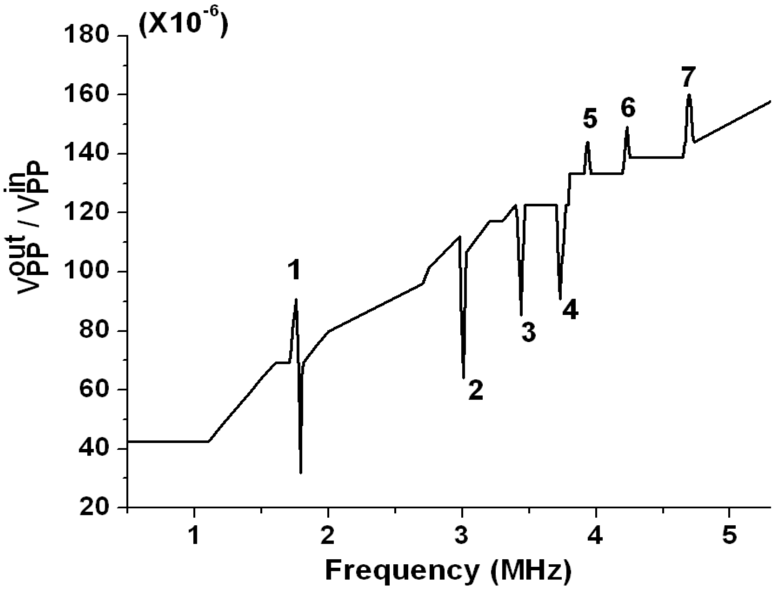

Figure 4-7. Plot of the ratio of the output to input voltage versus frequency. The peak-to-peak input voltage is fixed at 15 V throughout the experiment. Resonance-antiresonance 1 is due to S_0-plate-mode vibrations along plate thickness. The region between 2 to 3 MHz correspond to impurities for which L/P is an integer. The valleys and peaks 2 through 7 are due to impurities and point defects for which L/P is not an integer.

In addition to the acoustical mode, a few valleys and peaks are observed which are formed due to the presence of point defects in LN. The point defects form stresses inside the crystal, the distribution of point defects form a distribution of stresses. Upon r-f excitation, phonons are excited which travel through the stress distribution. The moving phonons constitute the acoustical modes. Table 4-1 provides the information about the valleys and peaks from 2 through 7. The first valley is denoted by 2, it is formed by the plate A_0 mode; the periodicity of impurities corresponding to this valley is 1.12 mm. The valley 3 is formed by the S_0 mode and the periodicity of impurities corresponding to this valley is 1.20 mm. The valley 4 is formed by the A_0 mode and the periodicity of impurities corresponding to this valley is 0.89 mm. It is interesting to note that the valleys in the admittance curve are formed, when the periodicities correspond to two peaks in the PL spectra (Figure 3-17(a) and 3-22). This is because as the r-f current propagates, the higher concentration of impurities absorbs the current and the energy spikes down. The plate S_0 mode forms the peak 5 and the periodicity of impurities corresponding to this peak is 0.89 mm. The plate A_0 mode forms the peaks 6 and 7, and the periodicities of impurities corresponding to these peaks are 0.80 mm and 0.74 mm. The peaks in the admittance curve are formed, when the periodicities correspond to two valleys in the PL spectra (Figure 3-17(a) and 3-22). This is because when the concentration of the impurities is minimum, the r-f current propagates more freely and the energy spikes up. Table 4-1. Information about the valleys and peaks of Figure 4-7.

Table 4-1. Information about the peaks and valleys of Figure 4-7.

Number	Frequency F (MHz)	Periodicity of impurity P(mm)	L/P	Impurity	Velocity (km/s) =F.*P*	Mode
Valley 2	3.00	1.12 Peak	44.6	Fe^{+}, Ba	3.36	A_0
Valley 3	3.40	1.20 Peak	41.7	Fe^{+}	4.80	S_0
Valley 4	3.73	0.89 Peak	56.2	Ba	3.32	A_0
Peak 5	3.93	0.89 Valley	56.2	Fe^{+}, Ba	3.49	S_0
Peak 6	4.23	0.80 Valley	62.5	Fe^{+}	3.38	A_0
Peak 7	4.70	0.74 Valley	67.6	Fe^{+}	3.48	A_0

4.3 Nonclassical Nonlinearity of Lithium niobate

The nonclassical nonlinearity (NN) was observed in LN at room temperature, the experimental details are discussed in section 2.9. The NN is observed between frequencies 1 MHz to 4 MHz. It is observed that in addition to the main bursts A1, A2,…. there are additional secondary signals S1, S2,….. which are not expected, as shown in Figure 4.8. The signal A1 is dispersive and is observed at a time delay of 13.6 µs, A1 is identified as the plate A0 mode. The second echo A2 is formed after three round trips of the sample at 40.8 µs. The signal between A1 and A2 is expected to be at the level of noise. This is not observed, secondary signals S1, S2 and more show up between the main bursts. The secondary signals are nondispersive in nature. In this section the first two main bursts A1 and A2, and the first two secondary signals S1 and S2 will be considered.

The non-exponential nature of the echo pattern is explained by the microstructure of ferroelectric LN, including impurities and point defects. When crystals are grown from a melt by the Czochralski method, they are multidomain ferroelectrics consisting of many 180^0 micro-domains along the z-axis, which is a consequence of internal energy minimization while the crystal solidifies[138]. To fabricate a single crystal, an external electric field or current is applied to a solid boule along the z-axis. However, there is always a certain concentration of residual micro-domains. The solid boule cannot be made into an ideal single crystal because of the crystal defects already present near the interdomain walls, during the first order solid-liquid transition. In other words, during solidification the interdomain walls attract the charged point defects and their complexes. In addition, linear defects including dislocations are formed near the interdomain walls as well. Practically not all of the inversely poled domains are 100% inverted by the external electric field. The second source of crystal inhomogeneity is a structure defect component near the original interdomain walls due to the presence of dislocations and clusters of point defects associated with them, which cannot be removed by an external electric current. The existence of the residual micro domains in LN was expreimentally observed using Transmission electron microscopy[139]. It was shown that the poling field usually applied after crystal growth is not sufficient to fabricate an ideal single-domain boule of LN. This fact is explained by the interactions of the internal electric fields due to dislocations with interdomain walls[139, 140]. These residual micro domains were named as “pre-existing domain nuclei” in theoretically single domain crystals[141, 142]. They are called “pre-existing” to separate the original micro domains from those created in subsequent experiments on polarization inversion.

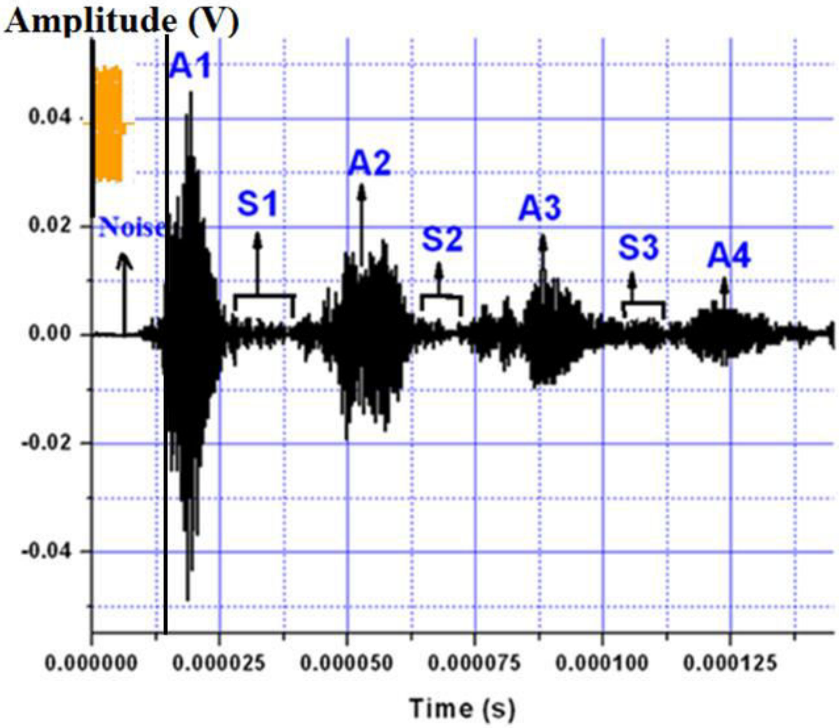

Figure 4-8. Acoustical wave propagation in YZ-LNO-Plate at r-f 1.60 MHz. Main bursts are denoted with A1, A2, A3, A4 and secondary signals are denoted by S1, S2, S3. The secondary signals arise due to the microstructure of LN. The input burst is shown in yellow and had 10 cycles.

The Fast Fourier Transform (FFT) of the main bursts and secondary nonlinear signals at an r-f of 1.60 MHz is shown in Figures 4-9 (a) and (b). The first excitation burst A1 reveals a peak at 1.61 MHz, as shown in Figure 4-9 (a). The secondary signal S1 (Figure 4-9 (b)) contains the peaks I1, which is also present in A1. S1 exhibits additional peaks at 1.13 MHz, 2.47 MHz, 2.93 MHz and 3.29 MHz, which are caused due to point defects and impurities. These signals are responsible for NN. It can be observed from Figure 4-9 (b) that the intensity of the NN peaks are lower in decibels than I1. The second main burst A2 contains two peaks at 1.48M Hz to 3.07 MHz, as shown in Figure 4-10 (a). The secondary signal S2 reveals peaks between 1.26 MHz to 3.66 MHz (Figure 4-10 (b). None of these peaks exactly coincide with the peaks in A2, these peaks are due to the presence of crystal defects. Thus at larger time delays, more and more crystal defects are manifested in the FFT.

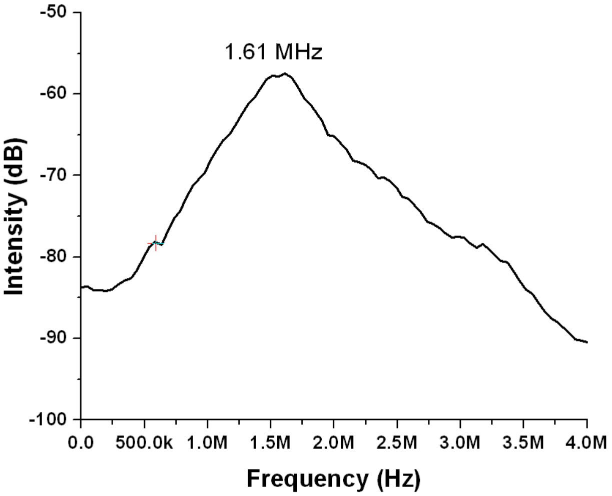

(a)

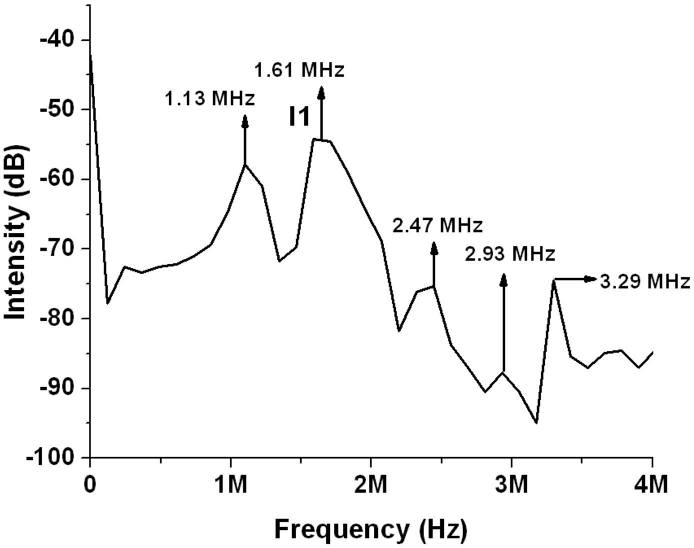

(b)

Figure 4-9. Fast fourier transform of (a) main excitation burst A1, and (b) fist nonclassical nonlinear signal S1, at r-f 1.60 MHz. The peak I1 at 1.61 MHz is present in A1. The other peaks at 1.13 MHz, 2.47 MHz, 2.93 MHz and 3.29 MHz are produced due to impurities and point defects.

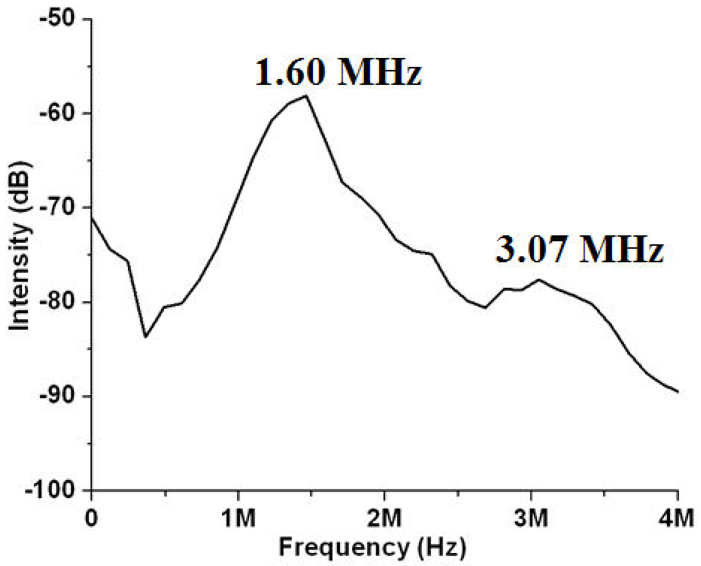

(a)

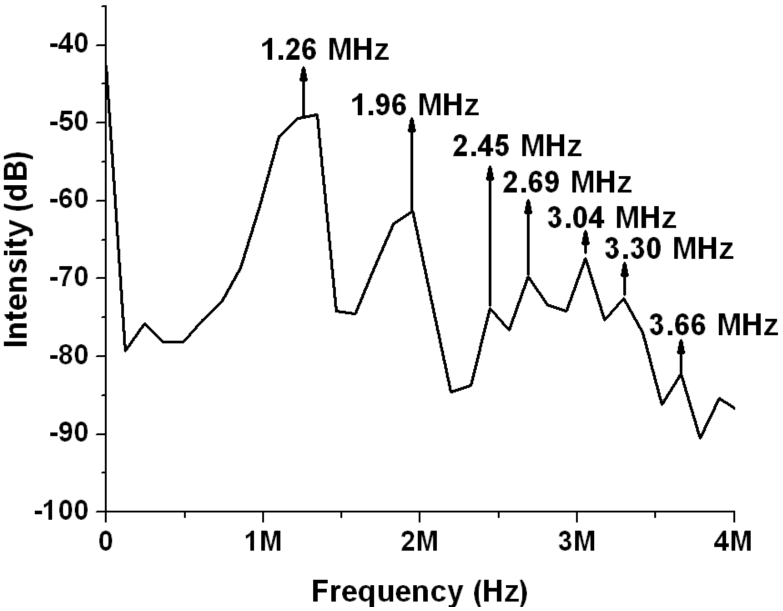

(b)

Figure 4-10. Fast fourier transform of (a) main burst A3, and (b) second secondary signal S3, at r-f 1.60 MHz. The frequencies present in A3 are 1.48 MHz and 3.07 MHz. These frequencies are absent in the FFT of S3. Therefore, all the peaks in S3 are produced due to the point defects and impurities.

The nonlinear signals are observed in PPLN, a plot of the echo amplitude versus delay time is shown in figure 4-11. The echoes exponentially fall to zero. However, two groups of nonlinear signals M1 and M2 appear after the main excitation has decayed. These groups of signals are called Acoustical Memory (AM), which arises due to structural inhomogeneity of LN.The AM was observed in the PPLN crystal with 1 mm copper electrodes bonded on either side of the periodicaly poled zone. The AM signal was observed when the input frequency was 3.27 MHz with a burst of 20 cycles. The echo train dies down to the level of noise after a few round trips through the sample. After a brief "dead time" the signal is seen to be restored, the restored signals are the AM signals M1 and M2.

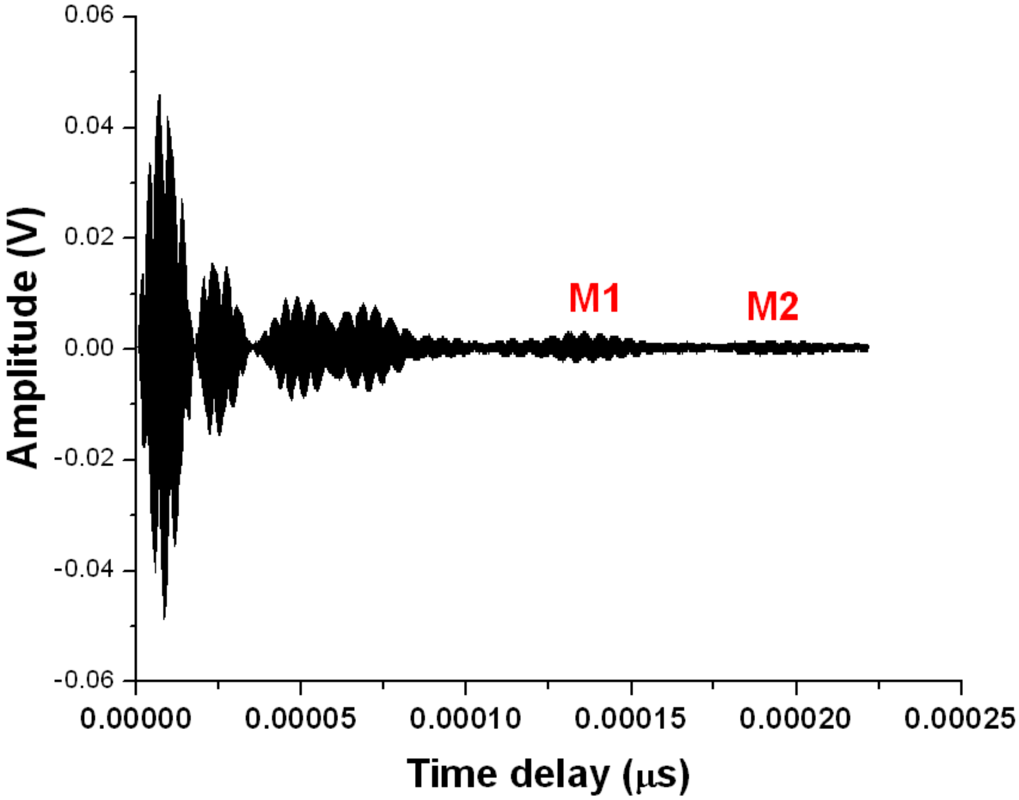

Figure 4-11. Acoustical propagation observed in PPLN crystal with domain length of 0.45 mm. M1 and M2 are the two groups of acoustical memory signals, at an input frequency of 3.27 MHz.

The AM is tied to the pinning and relaxation of domain walls within the crystal[21],the point defects are located near the domain walls. The distribution of point defects and impurities generate a distribution of stresses. The excitation burst produces acoustical phonons which travel through the periodic structure of stresses or "stress comb", there must be a delay time for which the domain walls within the crystal remain deformed. This delay time results from the electrical forces due to the piezoelectric effect within the crystal[21]. While stressed, the piezoelectrically induced electric fields can cause a redistribution of electrical charges within the domains. The subsequent motion of the domain wall motion results in the AM signal. The vibration of the ferroelectric domains and defects, which arises from the piezoelectric effect, still remains after the phonons have travelled through the distribution of stresses. This kind of behavior occurs in ferroelectric crystals, other media do not contain the domain structures[19]. Figure 4-12 shows the fast fourier transform (FFT) of the main burst of echoes. It can be observed that the central maxima mainly contains four frequencies 3.14 MHz, 3.22 MHz, 3.25 MHz and 3.27 MHz. The periodicity of impurities in PPLN is 0.45 mm as shown in section 3.1.7. The velocity of the acoustical wave at these fequencies are 1.41 km/s, 1.45 km/s, 1.46 km/s and 1.47 km/s. The propagating mode, due to the travelleing phonons through the stress comb, is identified as the plate A_0 mode. Figure 4-13 shows the FFT analysis of the memory signals M1and M2. The dominant frequency present is 3.27 MHz, which corresponds to the plate A_0 mode. The applications of AM include nondestructive microstructure analysis, that allows revealing those specific frequencies at which a particular LN crystal will demonstrate a nonclassical nonlinear behavior. Since PPLN is made from a crystal of superior quality, the defects do not reveal themselves at lower propagation times of the acoustical wave. The defects reveal themselves after the acoustical wave has made a few rounds trips. This is not the case in for nonclassical nonlinear behavior in single crystals where the nonlinear secondary crystaks show up between the main acoustical burst. Thus the type of nonlinearity observed can serve as a guideline to the nondestructive characterization of LN.

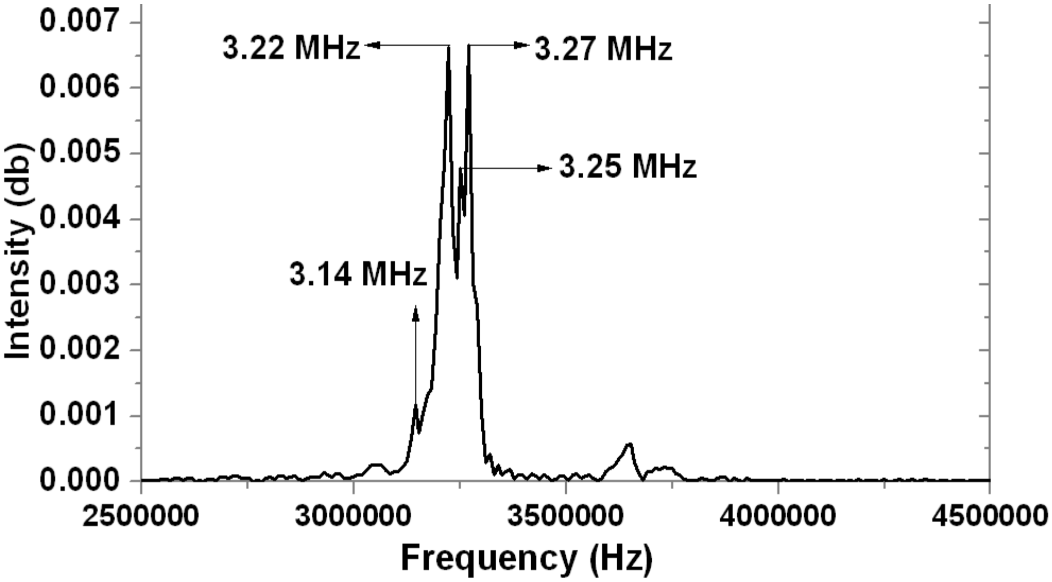

Figure 4-12. Fast fourier transform of exponentially decaying main burst of echoes (corresponding to Figure 4-10) through PPLN. Sharp peaks appear at 3.14 MHz, 3.22 MHz, 3.25 MHz and 3.27 MHz.

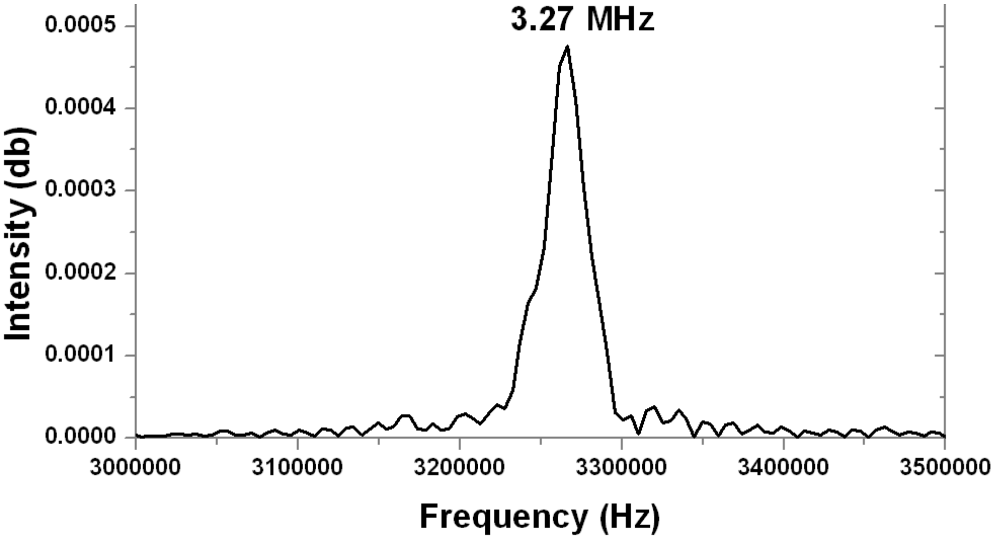

(a)

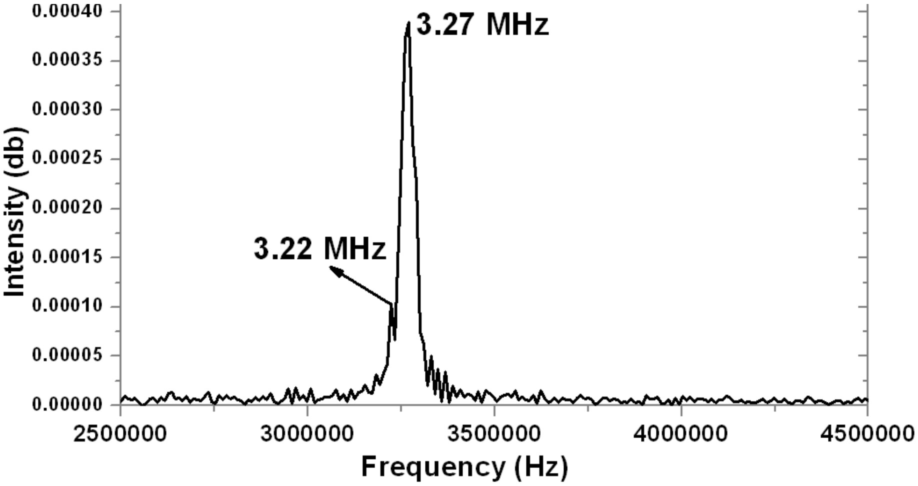

(b)

Figure 4-13. Fast fourier transform of acoustical memory signals (corresponding to Figure 4-10): (a) M1, a sharp peak is observed at 3.27 MHz. (b) M2, a sharp peak is observed at 3.27 MHz. A smaller peak is observed at 3.22 MHz.

CHAPTER V

CONCLUSIONS

1) PL spectra of LN shows several impurities. These can be categorized as: metals: Rb,W, Ag, Ba, Cr, Cs, Ru, Hg, Eu, Sn, Fe, Na; noble gases: Xe, Ne, Ar, Kr; host atoms: Li, Nb, O; F-center and Antisite defect (Nb_{Li}^{4+}). The PL is excited by 310 nm ultraviolet light, this excitation wavelength produces well resolved peaks for most of the impurities. 310 nm is the excitation wavelength for the F-center, which is the highest line in the emission spectrum.

2) The emission spectrum recorded between 350 nm and 890 nm consists of two parts, the blue-green spectrum and the near-infrared spectrum. The PL emission spectrum reveals the presence of dislocations. When the excitation wavelength is changed from 310 nm to 349 nm, the dislocation peak is red shifted by 0.23 eV. The presence of dislocations create additional energy states in the valence and conduction bands in LN. The transition of electrons between these energy states is observed as light emission.

3) The experimentally obtained peaks due to the impurities are mostly identified from the NIST database. The theoretical spectral line shape of luminescence, due to recombination of a hole with a donor or an electron with an acceptor is plotted. The position of theoretical peaks are in very good agreement with the experimental peaks. For example, the difference between the theory and experiment varies by 0.012% for the Xe II impurities. The theoretical plot due to direct bandgap transitions shows a steep decay on the low energy side, while the experimental

plot does not. This difference arises due to several factors including the influence of the slit of the monochromator, which smears the luminescence spectrum. Another reason is the broadening of the experimental spectral lines due to thermal collisions of the carriers at room temperature.

4) These theoretical PL spectral line are plotted for direct and indirect bandgap transitions in LN. For the Xe II impurity, the difference in the position of the peaks due to direct and indirect transitions, vary by 1.42 %. For the F-center defect, the difference in the position of the peaks due to direct and indirect transitions, vary by 3.18 %. There is significant broadening of the lineshape for indirect transitions in both the Xe II and F-center defects. This is due to the the fact that the excited electrons and holes in an indirect bandgap material, live much longer than in direct bandgap materials. Thus at room temperature, the thermal collisions between the particles are manifested in the broad spectral line.

5) An exponential fit called the Urbach tail, reduces the sharp fall at the lower energy side of the PL lines. The Urbach tail is theoretically plotted for the Xe II and antisite defects. The Urbach tail is associated with the width of the tail states in the bandgap and is related with the structural defects and disorder within the crystal.

6) The transmission edge of LN is observed at 312.37 nm. Thus, the band gap E_g is equal to 3.97 eV. The different impurities in LN form intraband acceptor and donor energy levels. The Ne , Xe and Nb_{Li}^{4+} form acceptor levels while the F-center, bipolaron (Nb_{Li}^{4+}-Nb_{Nb}^{4+}), Nb, Li and Fe I form donor levels. The 4d energy levels of Nb form the conduction band while the 2p energy levels of O form the valence band. The bands bend in the presence of the line defect and are dominated by the dislocation charge.

7) The samples were moved in steps of tens of microns, in order to find the distribution of the point defects and impurities parallel to the z-axis. The distribution of impurities including Fe^+, Ba and F-center is nonuniform and reveals peaks and valleys. For instance, the distance between consecutive peaks for the Fe^+ impurities, lies between 280 μm and 360 μm in the polarized bulk sample, and between 520 μm and 800 μm in the unpolarized bulk sample. For the YZ-cut wafers, the distance between consecutive peaks is not more than a few mm. The distribution of point defects with a certain periodicity, present on the host material indicates that LN is a metamaterial.

8) The PL spectra are recorded for ZX-cut single crystal LN (SCLN) and PPLN. The samples are scanned in a direction perpendicular to the z-axis. The distribution of point defects is nonuniform in both PPLN and SCLN; it reveals maxima and minima. The distribution of point defects in PPLN has a periodicity equal to the domain length. The point defects are localized mainly near the interdomain walls, the distribution of defects at these locations show maxima. Change in PL intensity in PPLN is much higher than SCLN, 24 times higher for noble gas defects. Overall, the distribution of point defects in PPLN is a periodic one and in SCLN it is a pure stochastic. The engineering applications of these findings may be non-destructive characterization of the phononic crystals.

9) The electromechanical transformation (EMT) of LN is estimated by reading an electric potential generated while applying a constant force to a local point. The distribution of EMT reveals peaks and valleys with periodicity similar to the distribution of impurities (DPI). The position of the maxima and minima of the EME distribution coincides with the DPI distribution. The charged impurities and point defects are sensitive to local electric polarization, they affect

the EME at a local point of the crystal. Higher the concentration of impurities, more is the EMT while lower the concentration of impurities, lesser is the EMT.

10) The electromechanical coupling coefficient (ECC) is modelled as a sum of two components, a constant defect free component and a defect dependent component. The defect dependent component varies as a cosine function and depends on the periodicity P. A plot of the ECC shows a nonuniform distribution with peaks and valleys. The location of the peaks and valleys in the ECC distribution coincide with the distribution of impurities and point defects.

11) Calculations show that the radio frequency admittance of Lithium niobate consists of a defect free part and a defect dependent part. The frequency dependency of the admittance exhibits those point defects with periodicity P, such that $\frac{L}{P} \neq n;\ n = 0,1,2 \ldots.$, where L is the length of the crystal.

12) The point defects and impurities form stresses inside the crystal. The distribution of point defects form a distribution of stresses with similar periodicity. On r-f excitation phonons are excited which travel through the “stress comb”. The moving phonons constitute the acoustical modes.

13) Experimental measurements of the r-f admittance reveal peaks and valleys which corresponds to specific ultrasonic modes in a plate. The valleys in the admittance plot are formed, when the periodicities correspond to two peaks in the PL spectra. This is because as the r-f current propagates, the higher concentration of impurities absorb the current and the energy spikes down. The peaks in the admittance plot are formed, when the periodicities correspond to two valleys in the PL spectra. This is because when the concentration of the impurities is minimum, the r-f current propagates more freely and the energy spikes up.

14) The nonclassical nonlinearity (NN) was observed in LN at room temperature. The main burst is identified as the plate A_0 mode. It is observed that in addition to the main bursts A1, A2, there are additional secondary signals S1, S2 which are not expected. Fast Fourier Transform of the secondary signals show that they related to the periodicity of the point defects and impurities.

15) The NN was observed in PPLN when the input frequency was 3.27 MHz with a burst of 20 cycles. The echo train dies down to the level of noise after a few round trips through the sample. After a brief "dead time" the signal is seen to be restored, the restored signals are called Acoustical Memory (AM) signals, denoted by M1 and M2. Fast fourier transform of the memory signals M1 and M2 show sharp central peaks at 3.27 MHz. The presence of internal defects generate internal stresses in the crystal. The periodicity of impurities in PPLN is 0.45 mm as shown in section 3.1.7. The propagating mode, due to the travelleing phonons through the stress comb, is identified as the plate A_0 mode. While stressed, the piezoelectrically induced electric fields can cause a redistribution of electrical charges within the domains. This results in the AM signal.

16) The NN including AM could be applied in nondestructive microstructure analysis, that allows revealing those specific frequencies at which a particular LN crystal will demonstrate a nonclassical nonlinear behavior.

BIBLIOGRAPHY

BIBLIOGRAPHY

[1]P. Mackwitz’, M. Rüsing, G. Berth, A. Widhalm, K. Müller, and A. Zrenner, “Periodic domain inversion in x-cut single crystal lithium niobate thin film”, *Applied Physics Letters* **108**,152902 (2016).

[2]J. W. Choi, DK. Ko, N. E. Yu’, K. Kitamura, and J. H. Ro’, “Domain wall kinetics of lithium niobate single crystals near the hexagonal corner”, *Applied Physics Letters* **106**, 102905 (2015).

[3]A. Guarino, G. Poberaj, D. Rezzonico, R. Degl'Innocenti and P. Günter, “Electro-optically tunable microring resonators in lithium niobate”, *Nature Photonics* **1**, 407-410 (2007).

[4]U. O. Salgeva, A. B. Volyncev, and S. B. Mendes, “Surface modification of optical materials with hydrogen plasma for fabrication of Bragg gratings”, *Applied Optics* **55**(3), 485-490 (2016).

[5]L. Cai, S. L. H. Han, and H. Hu, “Waveguides in single-crystal lithium niobate thin film by proton exchange”, *Optics Express* **23**, 1240-1248 (2015).

[6]F. S. Chen, J.T. LaMacchia, and D. B. Fraser, “Holographic Storage in Lithium niobate”, *Landmark Papers on Photorefractive Nonlinear Optics*, 33-35 (1995).

[7]N. G. R. Broderick, G. W. Ross, H. L. Offerhaus, D. J. Richardson, and D. C. Hanna, “Hexagonally Poled Lithium Niobate: A Two-Dimensional Nonlinear Photonic Crystal”, *Physical Review Letters* **84**, 4345 (2000).

[8]A. Baba, C. T. Searfass, and B. R. Tittmann, “High temperature ultrasonic transducer up to 1000^{O}C using lithium niobate single crystal”, *Applied Physics Letters* **97** (2010).

[9]M. H. Amini, A. N. Sinclair and T. W. Coyle, “A New High-Temperature Ultrasonic Transducer for Continuous Inspection”, *IEEE Transactions on Ultrasonics, Ferroelectrics, and Frequency Control* **63**(3), 448-455 (2016).

[10]J. H. Collins, H. M. Gerard, and H. J. Shaw, “High-performance lithium niobate acoustic surface wave transducers and delay lines”, *Applied Physics Letters* **13**, 312 (1968).

[11]K. G. Deshmukh and K. Singh, “Domain structure in lithium niobate single crystals”, *Journal of Physics D: Applied Physics* **5**(9), 1680 (1972).

[12]G. Malovichko, V. Grachev, and O. Schirmer, “Point Defects and Physical Properties of Ferroelectrics: Lithium Niobate”, *American Institute of Physics Conference Proc*eedings **677**, 196 (2003).

[13]V. Grachev, G. Malovichko, and O. Schirmir, “Structure of Point Defects in Lithium Niobate”, *Ukranian Journal of Phys*ics **49**(5), 438-447 (2004).

[14]F. Lhomme, P. Bourson, M. D. Fontana, G. Malovichko, M. Aillerie, and E. Kokanyan, “Luminescence of Cr^{3+} in lithium niobate: influence of the chromium concentration and crystal composition”, *Journal of Physics: Condensed Matter* **10**, 1137-1146 (1998).

[15]G. Stone, B. Knorr, V. Gopalan, and V. Dierolf, “Frequency shift of Raman modes due to an applied electric field and domain inversion in $LiNbO_3$”, *Physical Review B* **84**, 134303 (2011).

[16]MD. S. Ismom, H. H. Kusuma and M. R. Sudin, “A Study of the $LiNbO_3$ Crystal Growth Process by the Czochralski Method”, *Proceedings Science and Mathematic Simposium* (2005).

[17]R. Bhatt, I. Bhaumik, S. Ganesamoorthy, A. K. Karnal, P. K. Gupta, M. K. Swami, H. S. Patel, A. K. Sinha, and A. Upadhyay, “Study of structural defects and crystalline perfection of near stoichiometric $LiNbO_3$ crystals grown from flux and prepared by VTE technique”, *Journal of Molecular Struct*ure **1075**, 377-383 (2014).

[18]K. Lengyel, A. Peter, L. Kovacs, G. Corradi, L. Palfalvi, J. Hebling, M. Unferdorben, G. Dravecz, I. Hajdara, Zs. Szaller, and K. Polgar, “Growth, defect structure, and THz application of stoichiometric lithium niobate”, *Applied Physics Rev*iews **2**, 040601 (2015).

[19]D. Zhou, X. Liu, and X. Gong, “Experimental study of acoustical memory in lithium niobate”, *Physical Review E* **78**, 016602 (2008).

[20]M. A. Breazeale, I. V. Ostrovskii, and M. S. McPherson, “Thermal hysteresis of nonlinear ultrasonic attenuation in lithium niobate”, *Journal of Applied Physics* **96**, 2990 (2004).

[21]M. S. McPherson, I. Ostrovskii and M.A. Breazeale, “Observation of Acoustical Memory in $LiNbO_3$”, *Physical Review Letters* **89** (11)**,** 115506 (2002).

[22]M. A. Breazeale and I. V. Ostrovskii, “Fundamental and Nonclassical Nonlinearity in Crystals”, *American Institute of Physics Conference Proceedings* **838**, 11 (2006).

[23]R. Bhatt, I. Bhaumik, S. Ganesamoorthy, R. Bright, M. Soharab, A. K. Karnal, and P.K. Gupta, “Control of Intrinsic Defects in Lithium Niobate Single Crystal for Optoelectronic Applications”, *Crystals* **7**(2), 23 (2017).

[24]C. Koyama, J. Nozawa, K. Fujiwara, and S. Uda, “Effect of point defects on Curies temperature of lithium niobate”, *Journal of the American Ceramic Society* **100**(3), 1118–1124 (2017).

[25]W. Bollmann, “Stoichiometry and point defects in lithium niobate crystals”, *Crystal Research and Technol*ogy **18**(9), 1147–1149 (1983).

[26]L. Arizmendi, E. Ambite, J. L. Plaza and F. Jaque, "Point defects physics in lithium niobate related to optical damage resistance, photorefractive holographic properties and applications," *2012 IEEE International Conference on Oxide Materials for Electronic Engineering (OMEE)*, 2012, pp. 149-150, Ukraine.

[27] J. Shi and K. D. Becker, "Point defects and diffusion in oxides," *2012 IEEE International Conference on Oxide Materials for Electronic Engineering (OMEE)*, Ukraine, 2012, pp. 151-152.

[28] M. R. Hantehzadeh, *Investigation of Point Defects in Lithium niobate by Electron Spin Resonance, Electron Nuclear Double Resonance, and Optical Absorption,* PhD thesis, Oklahoma State University, 1987.

[29] S. Feng, B. Li, Z. Yang, Q. Jin, Z. Guo, and D. Ding, "Emperical Calculations of the Formation Energies of Point Defects in Lithium Niobate", *Journal of Inorganic Matererials* **18**(2), 283-288 (2003).

[30] Y. Li, W. G. Schmidt, and S. Sanna, "Defect complexes in congruent $LiNbO_3$ and their optical signatures", *Physical Review B* **91**, 174106 (2015).

[31] J. David N. Cheeke, *Fundamentals and applications of ultrasonic waves*, ISBN 0-8493-0130-0, (CRC series in pure and applied physics, 2002).

[32] A. P. Sarvazyan, M. W. Urban, and J. F. Greenleaf, "Acoustic Waves in Medical Imaging and Diagnostics", *Ultrasound in Medicine and Biology* **39**(7), 1133-46 (2013).

[33] K. L. Telschow, V. A. Deason, D. L. Cottle and J. D. Larson, "Full-field imaging of gigahertz film bulk acoustic resonator motion," in *IEEE Transactions on Ultrasonics, Ferroelectrics, and Frequency Control* **50**(10), 1279-1285 (2003).

[34] Ł. Ambrozinski, S. Song, S. J. Yoon, I. Pelivanov, D. Li, L. Gao, T. T. Shen, R. K. Wang, and M. O'Donnell, "Acoustic micro-tapping for non-contact 4D imaging of tissue elasticity", *Scientific Reports* **6**, 38967 (2016).

[35] R. Weigel *et al.*, "Microwave acoustic materials, devices, and applications," in *IEEE Transactions on Microwave Theory and Techniques* **50**(3), 738-749 (2002).

[36]M. Hribsek, “Surface Acoustic Wave Devices in Communications”, *Scientific Technical Review* **LVIII**(2), 44-49 (2008).

[37]J. M. Deacon, and J. Heighway, “Saw Filters for TV Receivers”, *IEEE Transactions on Consumer Electronics* **21**(4), 390-395 (1975).

[38] W. Shreve, "Signal processing using surface acoustic waves," in *IEEE Communications Magazine* **23**, 6-11 (1985).

[39]S. Kumar, G-H. Kim, K. Sreenivas, and R. P. Tandon, “ZnO based surface acoustic wave ultraviolet photo sensor”, *Journal of Electroceramics* **22**(1-3), 198-202 (2009).

[40]R. Stoney, B. Donohoe, D. Geraghty, and G. E. O’Donnell, “The Development of Surface Acoustic Wave Sensors (SAWs) for Process Monitoring” *Procedia CIRP* **1**, PP. 569-574 (2012).

[41]V. Polewczyk, K. Dumesnil, D. Lacour, M. Moutaouekkil, H. Mjahed, N. Tiercelin, S. Petit Watelot, H. Mishra, Y. Dusch, S. Hage-Ali, O. Elmazria, F. Montaigne, A. Talbi, O. Bou Matar, and M. Hehn, “Unipolar and Bipolar High-Magnetic-Field Sensors Based on Surface Acoustic Wave Resonators”, *Physical Review Applied* **8**, 024001 (2017).

[42]C. Viespe, and D. Miu, “Surface Acoustic Wave Sensor with Pd/ZnO Bilayer Structure for Room Temperature Hydrogen Detection”, *Sensors* **17**, 1529 (2017).

[43]K. R. Erikson, F. J. Fry and J. P. Jones, “Ultrasound in Medicine – A Review”, *IEEE Transactions on Sonics and Ultrasonics*, **53** (1974).

[44]C. A. Ozmen, D. Akin, A. H. Bayrak, S. Senturk, and H. Nazaroglu, “Ultrasound as a diagnostic tool to differentiate acute from chronic renal failure”, *Clinical Nephrology* **74**(1), 46-52 (2010).

[45]C. Boneti, M. R. Mc Vay, E. R. Kokoska, R. J. Jackson, and S. D. Smith, “Ultrasound as a

diagnostic tool used by surgeons in pyloric stenosis", *Journal of Pediatric Surgery* **43**(1), 87-91(2008).

[46]P. Zufferey, R. Valcov, I. Fabrequet, A. Dumusc, P. Omoumi, and A. So, "A prospective evaluation of ultrasound as a diagnostic tool in acute microcrystalline arthritis" *Arthritis Research and Therapy* **17**:188 (2015).

[47]V. F. M. Ramos, B. Karp, C. Lungu, K. Alter and M. Hallett, "Ultrasound as a Diagnostic Tool for Diaphragmatic Myoclonus: A Case Report (P3.015), *The Official Journal of the American Academy of* Neurology **84**(14), Supplement P3.015 (2015).

[48]L. Cartz, *Non Destructive Testing*, ISBN 978-0-87170-517-4, (ASM International, The Materials Information Society, 1995).

[49] K-Y. Jhang, "Nonlinear Ultrasonic Techniques for Non-destructive Assessment of Micro Damage in Material: A Review", *International Journal of Precision Engineering and Manufacturing*, **10** (2009).

[50]L. Brillouin, "Diffusion of light and X-rays by a Transparent Homogeneous Body", *Annales de Physique* **17** (1922).

[51]P. Debye, and F. W. Sears, "On the Scattering of Light by Supersonic Waves", *Proceedings of the National Academy of Sciences*, **18** (1932).

[52]M. Gal, "Modulation and Switching of Light", *Lecture notes on Optoelectronics*, The University of New South Wales (2005).

[53]C. B. Scruby, and L. E. Drain, *Laser Ultrasonics: Techniques and Applications*, (Taylor and Francis, 1990).

[54]S. P. Tennakoon, *Temperature and Pressure Effects on Elastic Proprties of Relaxor Ferroelectrics and Thermoelectric: A Resonant Ultrasound Spectroscopy Study*, PhD dissertation, The University of Mississippi (2016).

[55]M. Jamal, S. J. Asadabadi, I. Ahmad, and H. A. R.Aliabad, "Elastic constants of cubic crystals", *Computational Materials Science* **95**, 592-599 (2014).

[56]S. L. Shang, A. Saengdeejing, Z. G. Mei, D. E. Kim, H. Zhang, S. Ganeshan, Y. Wang, and Z. K. Liu, "First-principles calculations of pure elements: Equations of state and elastic stiffness constants", *Computational Materials Science* **48**(4), 813-826 (2010).

[57]X-Q. Chen, H. Niu, D. Li, and Y. Li, "Modeling hardness of polycrystalline materials and bulk metallic glasses", *Intermetallics* **19**(9), 1275-1281 (2011).

[58]Y-J. Hu, S-L. Shang, Y. Wang, K. A. Darling, B. G. Butler, L. J. Kecskes, and Z-K. Liu, "Effects of alloying elements and temperature on the elastic properties of W-based alloys by first-principles calculations", *Journal of Alloys and Compounds* **671,** 267-275 (2016).

[59]J. R. Rice and R. Thomson, "Ductile versus brittle behavior of crystals", *Philosophical Magazine: A Journal of Theoretical Experimental and Applied Physics* **29** (1), 73-97 (1974).

[60] D. A. Skoog, F. J. Holler, and S. R. Crouch, *Principles of Instrumental Analysis,* Chapter 1, 6th Edition, (Cengage Learning, 2007).

[61]G. Gautschi, *Piezoelectric Sensorics: Force Strain Pressure Acceleration and Acoustic Emission Sensors Materials and Amplifiers* (Springer, 2002).

[62]W.P. Mason, *Physical Acoustic* **I** (A), (Academic Press, New York, 1964).

[63]*Piezoelectric Components:Intro to Piezoelectric Transducer Crystals*, Boston Piezo Optics INC, (online available at: http://www.bostonpiezooptics.com/intro-to-transducer-crystals).

[64]J. Krautkramer and H. Krautkramer, *Ultrasonic Testing of Materials,* 4th edition, (Springer-Verlag, 1990).

[65] M. Birkholz, “Crystal-field induced dipoles in heteropolar crystals II: Physical significance”, *Zeitscrift fur Physik B Condensed Matter* **96** (1995).

[66]A. Romano, “Structure of Weiss domains in ferroelectric crystals”, *International Journal of Engineering Science*, **30** (1992).

[67]D. H. Jundt and G. Foulon, “Boules of $LiNbO_3$ congruently grown by the Czochralski technique” in *Properties of Lithium Niobate, pp*. 25-27, edited by K. K. Wong, (INSPEC, 2002).

[68]A. J. Dekker, *Solid State Physics*, Chapter 8, Ferroelectrics, (Macmillan , 2005).

[69]Ahmad Safari, *Piezoelectric and Acoustic Materials for Transducer Applications*, p.21, (Springer Science and Business Media, 2008).

[70]W.J. Merz, “Domain Formation and Domain Wall Motions in Ferroelectric $BaTiO_3$ Single Crystals”, *Physical Review* **95**, 690 (1954).

[71]T. Mitsui and J. Furuichi, “Domain Structure of Rochelle Salt and KH_2PO_4”, *Physical Review* **90**, 193 (1953).

[72] J. H. Cho, N. R. Yeom, S. J. Kwon, Y. Y. Lee, Y. H. Jeong, M. P. Chun, J. H. Nam, J. H. Paik and B. I. Kim, “Ferroelectric domain morphology and structure in Li-doped $(K,NA)NbO_3$ ceramics”, *Journal of Applied Physics* **112**, 052005 (2012).

[73]J. Schaab, I. P. Krug, F. Nickel, D. M. Gottlob, H. Doganaya, A. Cano, M. Hentschel, Z. Yan, E. Bourret, C. M. Schneider, R. Ramesh and D. Meier, “Imaging and characterization of conducting ferroelectric domain walls by photoemission electron microscopy”, *Applied Physics Letters* **104**, 232904 (2014).

[74] S. Y. Yang, J. Seidel, S. J. Byrnes, P. Shafer, C. H. Yang, M. D. Rossell, P. Yu, Y.H. Chu, J. F. Scott, J.W. Ager III, L.W. Martin and R. Ramesh, "Above-bandgap voltages from ferroelectric photovoltaic devices", *Nature Nanotechnology* **5**, 143-147 (2010).

[75] T. Sluka, A. K. Tagantsev, D. Damjanovic, M. Gureev and N. Setter, "Enhanced electromechanical response of ferroelectrics due to charged domain walls", *Nature Communications* **3**, 748 (2012).

[76] T. Sluka, A. K. Tagantsev, P. Bednyakov and N. Setter, "Free-electron gas at charged domain walls in insulating $BaTiO_3$", *Nature Communications* **4**, 1808 (2013).

[77] K. Nassau, H. J. Levinstein and G. M. Loiacono, "Ferroelectric Lithium Niobate. 1. Growth, Domain Structure, Dislocations and Etching", *Journal of Physics and Chemistry of Solids Solids* **27**(6-7), 983-988 (1966).

[78] M. Thirumavalavan, S. Sitharaman, S. Ravi, L. Durai, N. L. Jagota, R. C. Narula, and R. Thyagaranjan, "Growth of large diameter lithium niobate single crystals by czochralski method", *Ferroelectrics* **102**(1), 15-22 (1990).

[79] I. V. Ostrovskii and A. B. Nadtochiy, "Acoustoelectric Nonlinearity in Periodically Poled Lithium Tantalite", *American Institute of Physics Conference Proceedings* **838**, 55 (2006).

[80] Alistair C. Muir, *Interactions of Single Crystal Lithium Niobate Surfaces with Ultra-Violet Laser Radiation*, University of Southampton, Faculty of Engineering Science and Mathematics, Optoelectronics Research Centre, Retrieved from University of Southampton Research Repository, ePrints Soton, PhD Disserartion, 2008.

[81] L. Kovacs and K. Polgar, "Electrical Conductivity of $LiNbO_3$" in *Properties of Lithium Niobate*, EMIS Data reviews Series, edited by K. K. Wong, (INSPEC, Institution of Electrical Engineers, London, UK, 1989), pp. 91-96.

[82]R. Bhatt, S. Ganesamoorthy, I. Bhaumik, A.K. Karnal and P.K. Gupta, “Optical bandgap and electrical conductivity studies on near stoichiometric $LiNbO_3$ crystals prepared by VTE process”, *Journal of Physics and Chemistry of Solids* **73**(2), 257-261(2012).

[83]A. Sanson. A. Zaltron, N. Argiolas, C. Sada and M. Bazzan, “Polaronic deformation at the $Fe^{2+/3+}$ impurity site in Fe: $LiNbO_3$ crystals”, *Physical Review B* **91**, 094109 (2015).

[84]M. D. Fontana and P. Bourson, “Microstructure and defects probed by Raman spectroscopy in lithium niobate crystals and devices”, *Applied Physics Reviews* **2**, 040602 (2015).

[85]I. Ostrovskii and L. Cremaldi, “Split-mode ultrasonic transducer”, *The Journal of the Acoustical Society of America*” **134**(2), 1715-1723 (2013).

[86]M. S. Canney, V. A. Khokhlova, O. V. Bessonova, M. R. Bailey, and L. A. Crum, “Shock-Induced Heating and Millisecond Boiling in Gels and Tissue due to High Intensity Focused Ultrasound”, *Ultrasound in Medicine and Biology* **36**(2), 250-267 (2010).

[87]H. U. Ahmed, R. C. Hindley, L. Dickinson, A. Freeman, A. P. Kirkham, M. Sahu, R. Scott, C. Allen, J. V. Meulen, and M. Emberton, “Focal therapy for localized unifocal and multifocal prostate cancer: a prospective development study”, *The Lancet Oncology* **13**(6), 622-632 (2012).

[88]Y. Zhou, J. Zia, C. Warren, F. L. Starr, A. A. Brayman, L. A. Crum, and J. H. Hwang, “Targeted Long-Term venous Occlusion Using Pulsed High-Intensity Focused Ultrasound Combined with a Pro-Inflammatory Agent”, *Ultrasound in Medicine and Biology* **37**(10), 1653–1658 (2011).

[89]H. S. Hsu, V. Benjauthrit, F. Zheng, R. Chen, Y. Huang, Q. Zhou, and K. K. Shung, “PMN-PT-PZT composite films for high frequency ultrasonic transducer applications”, Sensors and Actuators A: Physical **179**, 121–124 (2012).

[90]A. L. Shuvalov and A. S. Gorkunova, “Transverse acoustic waves in piezoelectric and ferroelectric antiphase superlattices,” *Physical Review B* **59**, 9070 (1999).

[91]E. A. Eliseev, A. N. Morozovska, G. S. Svechnikov, V. Gopalan, and V. Y. Shur, “Static conductivity of charged domain walls in uniaxial ferroelectric semiconductors”, *Physical Review B* **83**, 235313 (2011).

[92]Y-F. Chen, S-N. Zhu, Y-Y. Zhu, N-B. Ming, B-B. Jin, and R-X. Wu, “High-frequency resonance in acoustic superlattice of periodically poled $LiTaO_3$”, *Applied Physics Letters* **70**, 592 (1997).

[93]I. V. Ostrovskii and A. B. Nadtochiy, “Free vibration of periodically poled ferroelectric plate”, *Journal of Applied Physics* **99**, 114106 (2006).

[94]D. S. Chezganov, E. O. Vlasov and V. Ya. Shur, “Periodical poling of $LiNbO_3$:MgO by electron beam”, *Ferroelectrics* **508**(1), 9-15 (2017).

[95]S. M. Shandarov, A. E. Mandel, A. V. Andrianova, G. I. Bolshanin, M. V. Borodin, A. Yu. Kim, S. V. Smirnov, A. R. Akhmatkhanov, and V. Ya. Shur, “Linear diffraction of light waves in periodically poled lithium niobate crystal”, *Ferroelectrics* **508**(1), 49-57 (2017).

[96]V. Ya. Shur, A. R. Akhmatkhanov, I. S. Baturin, “Micro- and nano-domain engineering in lithium niobate”, *Applied Physics Reviews* **2**, 40604 (2015).

[97]V. Ya. Shur, E.L. Rumyantsev, E. V. Nikolaeva, E. I. Shishkin, D. V. Fursov, R. G. Batchko, L. A. Eyres, M.M. Fejer, R.L. Byer, J. Sindel, “Formation of self-organized nanodomain patterns during spontaneous backswitching in lithium niobate”, *Ferroelectrics* **253**, 105–114(2001).

[98]V. S. Ilchenko, A. A. Savchenkov, A. B. Matsko, and L. Maleki, “Nonlinear Optics and Crystalline Whispering Gallery Mode Cavities”, *Physical Review Lett*ers **92**, 043903 (2004).

[99]N.G.R. Broderick, G.W. Ross, H.L. Offerhaus, D. J. Richardson, and D. C. Hanna, “Hexagonally Poled Lithium Niobate: A Two-Dimensional Nonlinear Photonic Crystal” *Physical Review Lett*ers **84**, 4345 (2000).

[100]M. L. Sundheimer, and P. Baldi, “New frequency standard for optical telecommunications based on difference-frequency generation in PPLN waveguides”, *Proceedings of the 2003 SBMO/IEEE MTT-S International Microwave and Optoelectronics Conference* - IMOC (2003).

[101]M. Ziyadi, A. Mohajerin-Ariaei, M. Chitgarha, S. Khaleghi, A. Almaiman, A. Abouzaid, J. Touch, M. Tur, L. Paraschis, C. Langrock, M. M. Fejer, and A. Willner, “Experimental demonstration of a variable bandwidth, shape and center-frequency RF photonics filter using a continuously tunable optical tapped-delay-line and having an optical output”, *Conference on Lasers and Electro-Optics (CLEO) - Laser Science to Photonic Applications* (2014).

[102]J. O. Vasseur, P. A. Deymier, B. Djafari-Rouhani, Y. Pennec, and A-C. Hladky-Hennion, “Absolute forbidden bands and waveguiding in two-dimensional phononic crystal plates”, *Physical Review B* **77**, 085415 (2008).

[103]J. M. Vasseur, A-C. Hladky-Hennion, B. Dubus, B. Djafari-Rouhani, and B. Morvan, “Design and characterization of stop-band filters using PZT layer on silicon substrate phononic crystals”, *The Journal of the Acoustical Society of America* **123**, 3039 (2008).

[104]C. Restoin, C. Darraud-Taupiac, J-L. Decossas, J-C. Varreile, V. Couderc, A. Barthelemy, A. Martinez, and J. Hauden, “Electron-beam poling on Ti:$LiNbO_3$”, *Applied Optics* **40**(33), 6056-6061 (2001).

[105]T. R. Volk, L. S. Kokhanchik, R. V. Gainutdinov, Y. V. Bodnarchuk, S. M. Shandarov, M. V. Borodin, S. D. Lavrov, H. Liu, and F. Chen, “Microdomain patterns recorded by an electron

beam in He-implanted optical waveguides on X-Cut $LiNbO_3$ crystals" *Journal of Lightwave Technology* **33**, 4761–4766 (2015).

[106]L. S. Kokhanchik and T. R. Volk, "Domain inversion in $LiNbO_3$ and Zn-doped $LiNbO_3$ crystals by the electron-beam irradiation of the nonpolar Y-surface", *Applied Physics B* **110,** 367-373(2013).

[107]L. S. Kokhanchik, M. N. Palatnikov, and O. B. Shcherbina, "Ferroelectric domains in near-stoichiometric $LiNbO_3$ by e-beam polarization reversal", *Phase Transitions* **84**, 797–803(2011).

[108]X. Li, K. Terabe, H. Hatano, and K. Kitamura, "Domain patterning in $LiNbO_3$ and $LiTaO_3$ by focused electron beam", *Journal of Crystal Growth* **292**, 324–327 (2006).

[109]D. S. Chezganov, M. M. Smirnov, D. K. Kuznetsov, and V. Y. Shur, "Electron Beam Domain Patterning of MgO-Doped Lithium Niobate Crystals Covered by Resist Layer", *Ferroelectrics* **476**, 117–126(2015).

[110]T. W. Fan, J. J. Qian, J. Wu, L. Y. Lin, and J. Yuan, "Tentative analysis of Swirl defects in silicon crystals", *Journal of Crystal Growth* **213**(3-4), 276-282 (2000).

[111] S. Siebentritt, S. Augustin, N. Papathanasiou, D. Hebert, A. Rockett, J. Bläsing and M. C. Lux-Steiner, "Polarized Luminescence of Defects in $CuGaSe_2$", *Materials Research Society Symposium Y-Thin-Film Compound Semiconductor Photovoltaics* **1012**, (2007).

[112]I. Pelant and J. Valenta, *Luminescence Spectroscopy of Semiconductors*, ISBN 978-0-19-875754-2, (Oxford University Press, 2012).

[113]A. M. Prokhorov and Y. S. Kuz'minov, *Physics and Chemistry of Crystalline Lithium Niobate*, ISBN 0-85274-002-6, Hilger, Bristol and New York, (IOP Publishing Ltd. 1990), p. 99.

[114] A. Kramida, Y. Ralchenko, J. Reader and NIST ASD Team (2018), NIST Atomic Spectra Database (ver. 5.5.2), National Institute of Standards and Technology, Gaithersburg, MD, (online

available at http://physics.nist.gov/asd).

[115]P. D. Townsend, updated by K. A. Green, *Luminescence of LiNbO$_3$, in Properties of Lithium Niobate* ,EMIS Data reviews Series, edited by K. K. Wong, (INSPEC, Institution of Electrical Engineers, 2002), pp. 185-186.

[116]B. M. Gorelov, “Microwave-Stimulated Electron Trapping by Dislocations in Zinc and Cadmium Sulfides”, *Technical Physics Letters* **31**(1), 40-42 (2005).

[117]M. Fox, *Optical Properties of Solids*, ISBN 978-0-19-957337-0, 2nd edition, (Oxford University Press, 2010).

[118]S. Cabuk and A. Mamedov, “Urbach rule and optical properties of the LiNbO$_3$ and LiTaO$_3$”, *Journal of Optics A, Pure and Applied Optics* **1**(3), 424 (1999).

[119]T. H. Gfroerer, “Photoluminescence in Analysis of Surfaces and Interfaces” in *Encyclopedia of Analytical Chemistry*, (John Wiley and Sons Limited, 2000).

[120]M. Imlau, H. Badorreck, and C. Merschjann, “Optical nonlinearities of small polarons in lithium niobate”, *Applied Physics Reviews* **2**, 040606 (2015).

[121]H. Haken, H. C. Wolf, Translated by W. D. Brewer, *The Physics of Atoms and Quanta*, 7th edition, (Springer, 2005).

[122] H-N. Ji, Y-P. Ok, W-P. Tai, J-H. Seol, and J-S. Lee “Preparation of Lead-free (K, Na)NbO$_3$-LiSbO$_3$ Ceramics with High Piezoelectric Constants by FeO Doping”, *Journal of the Korean Physical Soociety* **56**(4), 1156-1159 (2010).

[123]Y. S. Kuz’minov, *Lithium Niobate Crystals*, Cambridge International Science Publishing.

[124] H. Steigerwald, *Influence of UV Light and Heat on the Ferroelectric Properties of Lithium Niobate Crystals*, Doctoral Disserartion, Mathematisch-Naturwissenschaftlichen Fakultat, Rheinischen Friedrich-Wilhelms-Universitat Bonn, 2011.

[125]D-S. Byeon, S-M. Jeong, K-J. Hwang, M-Y. Yoon, H-J. Hwang, S. Kim, and H-L. Lee, "Oxide ion diffusion in Ba-doped $LaInO_3$ perovskite: A molecular dynamics study", *Journal of Power Sources* **222**, 282-287 (2013).

[126]M. Saxena and T. Maiti, "Effect of Ba-doping on high temperature thermoelectric properties of Sr2TiMoO6 double perovskites", *Journal of Alloys and Compounds* **710**, 472-478 (2017).

[127]H. Xie, W-Y. Hsu, and R. Raj, "Nonlinear optical properties of epitaxial lithium tantalate thin films", *Journal of Applied Physics* **77**, 3420 (1995).

[128]J. Lehman, A. Sanders, L. Hanssen, B. Wilthan, J. Zeng, and C. Jensen, "Very Black Infrared Detector from Vertically Aligned Carbon Nanotubes and Electric-Field Poling of Lithium Tantalate", *Nano Letters* **10**(9), 3261-3266 (2010).

[129]J. Wang, J. Gou, and W. Li, "Preperation of room temperature terahertz detector with lithium tantalate crystal and thin film", *American Institute of Physics Advances* **4**, 027106 (2014).

[130]C. K. Campbell, *Surface Wave Acoustic Devices for Mobile and Wireless Communications*, (Academic Press, INC, 1998).

[131]S. Matsumoto, E. J. Lim, H. M. Hertz, M. M. Fejer, "Quasiphase-matched second harmonic generation of blue light in electrically periodically-poled lithium tantalate waveguides", *Electronics Letters* **27**(22), 2040-2042 (1991).

[132]J. Koskela, J. V. Knuuttila, T. Makkonen, V. P. Plessky, and M. M. Salomaa, "Acoustic loss mechanisms in leaky SAW resonators on lithium tantalate", *IEEE Transactions on Ultrasonics,Ferroelectrics, and Frequency Control* **48**(6), 1517-1526 (2001).

[133]Lithium Tantalate ($LiTaO_3$), Precision Micro-Optics,(online available at: http://www.pmoptics.com/lithium_tantalate.html)

[134]B. Naranjo, J. K. Gimzewski and S. Putterman, "Observation of nuclear fusion driven by a

pyroelectric crystal", *Nature* **434**, 1115-1117 (2005).

[135]A. Ballato, "Electromechanical coupling factors of $LiNbO_3$" , *in Properties of Lithium Niobate*, EMIS Data reviews Series, edited by K. K. Wong, (INSPEC, Institution of Electrical Engineers, London, UK, 1989), pp. 108-111.

[136]A. B-Holder, "The polarizability model for ferroelectricity in perovskite oxides", *Journal of Physics: Condensed Matter* **24**(7), 273202 (2012).

[137]I. Ostrovskii, A. Nadtochiy, and L. Cremaldi, "Vibrations of Periodically Poled Lithium Niobate Bar with 0.3-mm Long Domains", arXiv:1610.07571 [cond-mat.mtrl-sci].

[138]I. Ostrovskii, "Research on acoustical memory discovered in the laboratory of Mack Breazeale", *Proceedings of Meetings of Acoustics* **9**, 045004 (2010).

[139]H. Cerva, P. Pongratz, and P. Skalicky, "Lattice defects in single-crystal lithium niobate I. Transmission electron microscopy", *Philosophical Magazine A* **54**(2), 185-197 (1986).

[140]H. Cerva, P. Pongratz, and P. Skalicky, "Lattice defects in single-crystal lithium niobate II. Electric fields of dislocations and small-angle grain boundaries", *Philosophical Magazine A* **54**(2), 199-212 (1986).

[141]V. Gopalan and T. E. Mitchell, "Wall velocities, switching times, and the stabilization mechanism of 180^0 domains in congruent $LiTaO_3$ crystals", *Journal of Applied Physics* **83**, 941 (1998).

[142]S. Kim, V. Gopalan, and A. Gruverman, "Coercive fields in ferroelectrics: A case study in lithium niobate and lithium tantalate," *Applied Physics Letters* **80**, 2740 (2002).

[143]X. Chen, "Ultrasonic Guided Waves in Piezoelectric Layered Composite with Different Interfacial Properties", *Advances in Materials Science and Engineering* **2011**, Article ID 701819 (2011).

LIST OF APPENDICES

APPENDIX A

The Mathematica codes for modelling the defect peaks for direct bandgap transitions, indirect bandgap transitions and the Urbach tail are given below:

Defect Peaks for Direct Bandgap LN

```
(*Peak Calculation for F-center defect in Lithium niobate *)
ClearAll[lambda, Eg, Ea, KT];
Element[Eg, Reals];
Element[Ea, Reals];
Eg = 3.97; (*Band Gap of LN in eV*)
Ea = 0.887;     (* guess energy of peak in eV*)
KT = 0.0257;  (*Boltzmann constant x Temperature (Room) in eV *)
spectrum =   Table[{lambda,     Re[Sqrt[(1239.84/lambda) - (Eg - Ea)]*  Exp[((1239.84/lambda)
- (Eg - Ea))/-KT]]}, {lambda, 350., 420.,     0.05}]
ListLinePlot[spectrum, PlotRange -> All]
Export["F-center-Direct-Peak.xls", spectrum]


(*Peak Calculation for Xe defect in Lithium niobate *)
ClearAll[lambda, Eg, Ea, KT];
Element[Eg, Reals];
Element[Ea, Reals];
Eg = 3.97; (*Band Gap of LN in eV*)
Ea = 1.416;(* Energy of peak from transmission spectra in eV*)
KT = 0.0257;  (*Boltzmann constant x Temperature (Room) in eV *)
spectrum = Table[{lambda, Re[Sqrt[(1239.84/lambda) - (Eg - Ea)]*
Exp[((1239.84/lambda) - (Eg - Ea))/-KT]]}, {lambda, 420., 520.,     0.05}]
ListLinePlot[spectrum, PlotRange -> All]
Export["Xe-Direct-Peak.xls", spectrum]


(*Peak Calculation for Antisite defect in Lithium niobate *)
 ClearAll[lambda, Eg, Ed, KT];
Element[Eg, Reals];
Element[Ed, Reals];
Eg = 3.97; (*Band Gap of LN in eV*)
Ed = 1.6;     (* Energy of peak from transmission spectra in eV*)
KT = 0.0257;  (*Boltzmann constant x Temperature (Room) in eV *)
spectrum = Table[{lambda, Re[Sqrt[(1239.84/lambda) - (Eg - Ed)]*
Exp[((1239.84/lambda) - (Eg - Ed))/-KT]]}, {lambda, 450., 550.,     0.05}]
ListLinePlot[spectrum, PlotRange -> All]
Export["Antisite-Direct-Peak.xls", spectrum]
```

Defect Peaks for Indirect Bandgap LN

```
(*Peak Calculation for F-center defect in Lithium niobate *)
 ClearAll[lambda, Eg, Ea, KT];
Element[Eg, Reals];
Element[Ea, Reals];
Eg = 3.97; (*Band Gap of LN in eV*)
Ea = 0.887;    (* guess energy of peak in eV*)
KT = 0.0257;  (*Boltzmann constant x Temperature (Room) in eV *)
ħω = 0.13;
spectrum = Table[{lambda, Re[(((1239.84/lambda) - ((Eg - ħω) - Ea))^2)*
Exp[((1239.84/lambda) - ((Eg - ħω) - Ea))/-KT]]}, {lambda, 350., 420., 0.05}]
ListLinePlot[spectrum, PlotRange -> All]
Export["F-center-Indirect-Peak.xls",spectrum]
```

```
(*Peak Calculation for Xe defect in Lithium niobate *)
ClearAll[lambda, Eg, Ea, KT];
Element[Eg, Reals];
Element[Ea, Reals];
Eg = 3.97; (*Band Gap of LN in eV*)
Ea = 1.416;  (* Energy of peak from transmission spectra in eV*)
KT = 0.0257; (*Boltzmann constant x Temperature (Room) in eV *)
ħω = 0.075;
spectrum = Table[{lambda, Re[(((1239.84/lambda) - ((Eg - ħω) - Ea))^2)*
Exp[((1239.84/lambda) - ((Eg - ħω) - Ea))/-KT]]}, {lambda, 400., 500., 0.05}]
ListLinePlot[spectrum, PlotRange -> All]
Export["Xe-Indirect-Peak.xls",spectrum]
```

Urbach Tail

```
(*Urbach rule for Xe defect in Lithium niobate*)
ClearAll[lambda, Eg, Ea, KT];
Element[Eg, Reals];
Element[Ea, Reals];
Eg = 3.97;      (*Band Gap of LN in eV*)
Ea = 1.416;     (* Acceptor Level in eV*)
KT = 0.0257;   (*Boltzmann constant x Temperature (Room) in eV *)
spectrum = Table[{lambda, Re[Sqrt[(1239.84/lambda) - (Eg - Ea)]*
Exp[((1239.84/lambda) - (Eg - Ea))/-KT] + HeavisideTheta[lambda - 485.35]*2500*
Exp[((1239.84/lambda) - 0.7192 Eg)/KT]]}, {lambda, 420., 520.,  0.05}]
ListLinePlot[spectrum, PlotRange -> All]
Export["Urbach-Xe.xls", spectrum]
```

```
(*Urbach rule for Antisite defect in Lithium niobate*)
ClearAll[lambda, Eg, Ed, KT];
Element[Eg, Reals];
Element[Ed, Reals];
Eg = 3.97;      (*Band Gap of LN in eV*)
Ed = 1.6;    (* donor Level in eV*)
KT = 0.0257;   (*Boltzmann constant x Temperature (Room) in eV *)
spectrum = Table[{lambda, Re[Sqrt[(1239.84/lambda) - (Eg - Ed)]*
Exp[((1239.84/lambda) - (Eg - Ed))/-KT] + HeavisideTheta[lambda - 523.1]*7700*
Exp[((1239.84/lambda) - 0.68 Eg)/KT]]}, {lambda, 420., 620.,    0.05}]
ListLinePlot[spectrum, PlotRange -> All]
Export["Urbach-Antisite.xls", spectrum]
```

Plot of Electromechanical Coupling Coefficient

```
(*Electromechanical Coupling Coefficient ECC for Ba impurity*)
ClearAll[P1, P2, P3, P4, P5, P6, P7, P8, P9, P10, K0, Kd];
Element[P1, Reals]; Element[P2, Reals]; Element[P3, Reals]; Element[P4, Reals]; Element[P5,
Reals]; Element[P6, Reals]; Element[P7, Reals]; Element[P8, Reals]; Element[K0, Reals];
Element[Kd, Reals];
(*P1 through P8 are the periodicities obtained from PL measurements on Ba distribution*)
P1 = 1.30; P2 = 1.20; P3 = 1.48; P4 = 1.12; P5 = 0.89; P6 = 0.66; P7 = 1.24; P8 = 0.72;
K0 = 2.21;(*Reference: KK Wong, page 108*) (*K0 is the constant part of the ECC*)
Kd = 0.221; (*Defect dependent part of the ECC is 10 percent of K0*)
K = Table[{z,    K0*(1 - (Kd/K0)*(Cos[2*Pi*z/P1] + Cos[2*Pi*z/P2] + Cos[2*Pi*z/P3] +
Cos[2*Pi*z/P4] + Cos[2*Pi*z/P5] + Cos[2*Pi*z/P6] +          Cos[2*Pi*z/P7] +
Cos[2*Pi*z/P8]))}, {z, 12., 24., 0.05}]
ListLinePlot[K, PlotRange -> All]
```

```
(*Electromechanical Coupling Coefficient ECC for Fe+ impurity*)
ClearAll[P1, P2, P3, P4, P5, P6, P7, P8, P9, P10, K0, Kd];
Element[P1, Reals]; Element[P2, Reals]; Element[P3, Reals]; Element[P4, Reals]; Element[P5,
Reals]; Element[P6, Reals]; Element[P7, Reals]; Element[P8, Reals]; Element[K0, Reals];
Element[Kd, Reals];
(*P1 through P10 are the periodicities obtained from PL measurements on Fe+ distribution*)
P1 = 2.54; P2 = 1.20; P3 = 0.80; P4 = 1.00; P5 = 1.12; P6 = 1.36; P7 = 1.30; P8 = 0.55; P9 =
0.86; P10 = 0.94;
K0 = 2.21;(*Reference: KK Wong, page 108*) (*K0 is the constant part of the ECC*)
Kd = 0.221; (*Defect dependent part of the ECC is 10 percent of K0*)
K = Table[{z,    K0*(1 - (Kd/K0)*(Cos[2*Pi*z/P1] + Cos[2*Pi*z/P2] + Cos[2*Pi*z/P3] +
Cos[2*Pi*z/P4] + Cos[2*Pi*z/P5] + Cos[2*Pi*z/P6] +          Cos[2*Pi*z/P7] + Cos[2*Pi*z/P8]
```

```
+ Cos[2*Pi*z/P9] +           Cos[2*Pi*z/P10]))}, {z, 12., 24., 0.05}]
ListLinePlot[K, PlotRange -> All]
```

APPENDIX B

Dispersion curves of Plate Acoustic Waves in YZ-cut Lithium niobate

The experimental setup to detect plate acoustic waves (PAW) in LN is shown in Figure B-1. The PAW is excited by applying rf-voltage to copper electrodes on the end faces of the sample. PAW modes were observed and data was recorded for the A_0 and S_0 modes. For the YZ-cut crystal, the acoustical waves propagate along the z direction. The group velocity v_g of a mode is calculated as

$$v_g = \frac{L}{T} \tag{B.1}$$

where L is the length of the sample and T is the delay time. Figure B-2 shows procedure to obtain the delay time for a particular propagating mode.

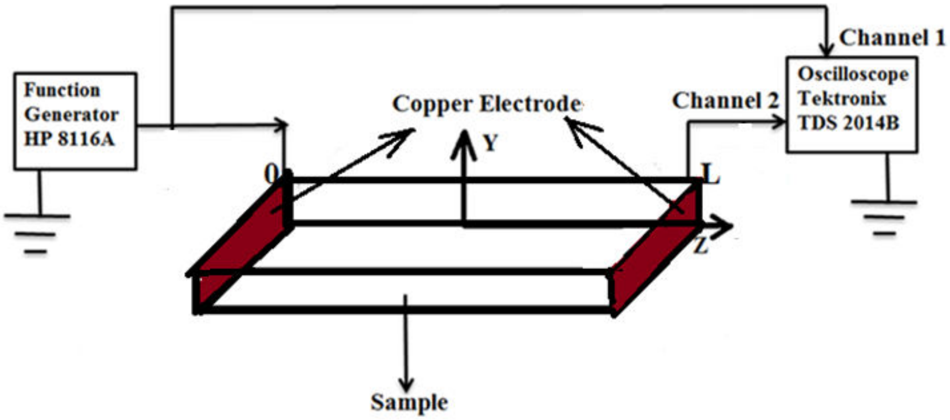

Figure B-1. The experimental setup to observe plate acoustic waves from YZ-LNO-Plate.

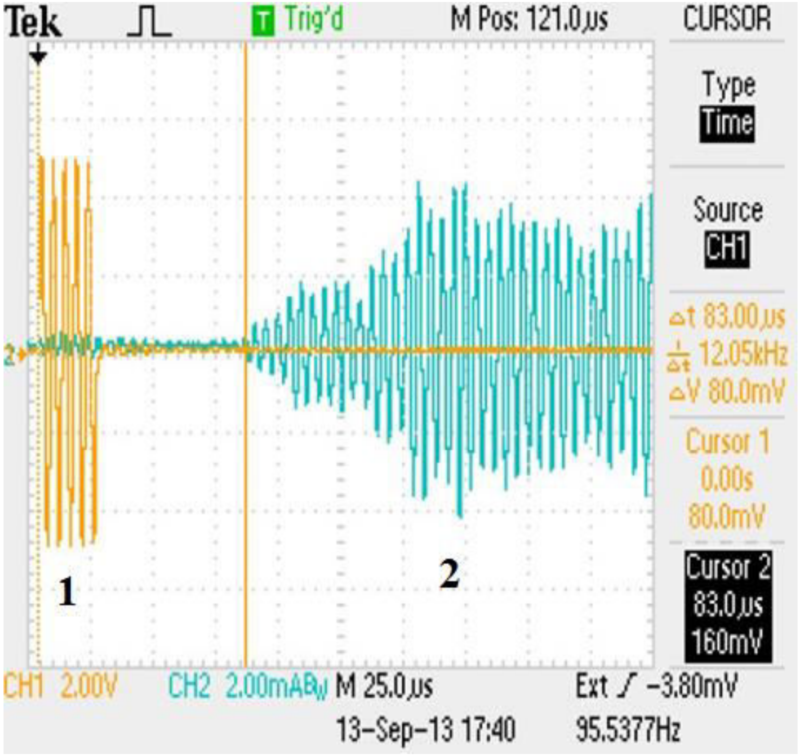

Figure B-2. Procedure to obtain time delay of a propagating mode. The input signal (1) contains a burst of 5 cycles. The input frequency is 2.5 MHz. The propagating S_0 mode is denoted by 2. The time difference between the start of the input signal to the start of the output signal gives the time delay.

The dispersion curve for the zeroth order lamb modes were plotted using the relation

$$v_p = \frac{\omega}{k} \quad , \quad v_g = \frac{\partial \omega}{\partial k} = \frac{1}{\left[\frac{\partial\left(\frac{\omega}{v_P}\right)}{\partial \omega}\right]} = \frac{1}{\left[\frac{v_P - \omega \frac{\partial v_P}{\partial \omega}}{v_P^2}\right]} = \frac{v_P^2}{v_P - \omega \frac{\partial v_P}{\partial \omega}} \qquad \text{(B.2)}$$

Where v_p is the phase velocity of the mode, ω is is the angular frequency and k is the wave number.

For a known curve of phase velocity versus frequency[143], equation (B.2) becomes

$$y_g = \frac{y_p^2}{y_p - x\dfrac{\Delta y_p}{\Delta x}} \qquad \text{(B.3)}$$

Where (x, y_p) are the co-ordinates of a point on the plot. Figure B-3 shows the dispersion of group velocity for the plate A_0 and S_0 modes.

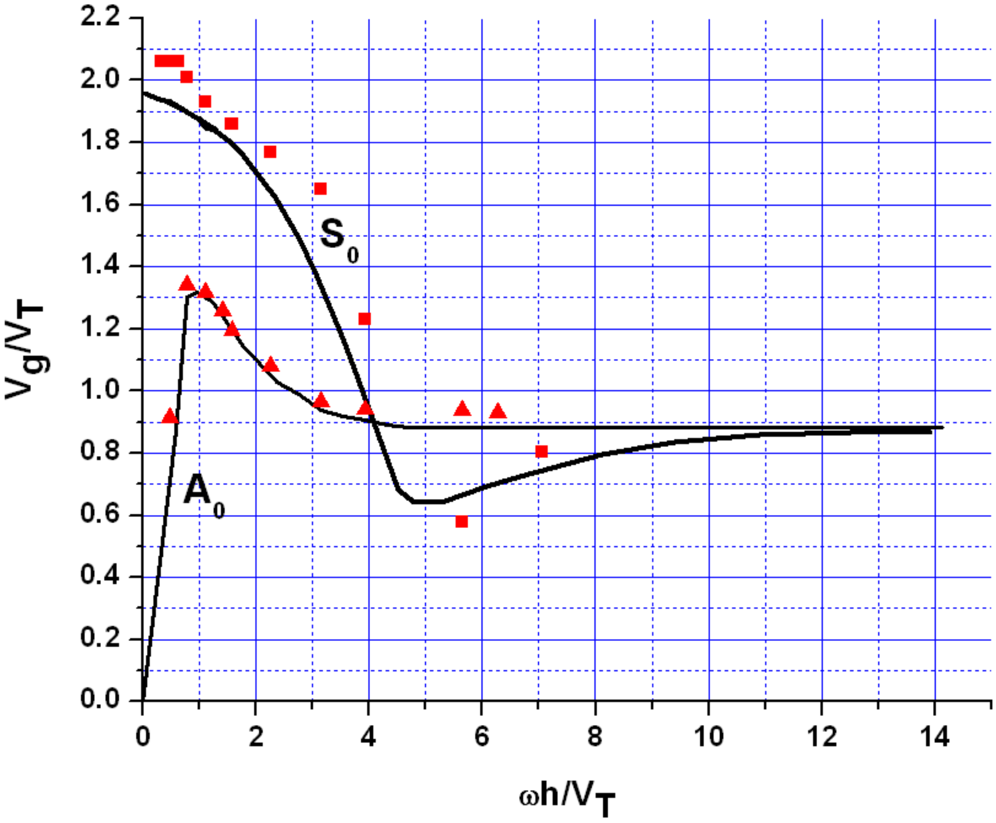

Figure B-3. Dispersion of group velocity of A_0 and S_0 modes in YZ-LNO-Plate. The symbol ω denotes the angular frequency and h denotes the half-thickness of the plate. The ordinate and abscissa are both normalized with respect to the velocity of the transverse wave V_T propagating in the z-direction.

The PAW modes are highly dispersive as seen in Figure B-3. The dispersive nature of the A_0 and S_0 modes can be seen in Figure B-4. As the frequency is changed from 4.2 MHz to 4.3 MHz, the delay time for the A_0 mode increases from 20.7 μs to 22.6 μs. Thus the A_0 mode becomes slower. The delay time for the S_0 mode decreases from 28.7 μs to 27.3 μs, the mode becomes faster.

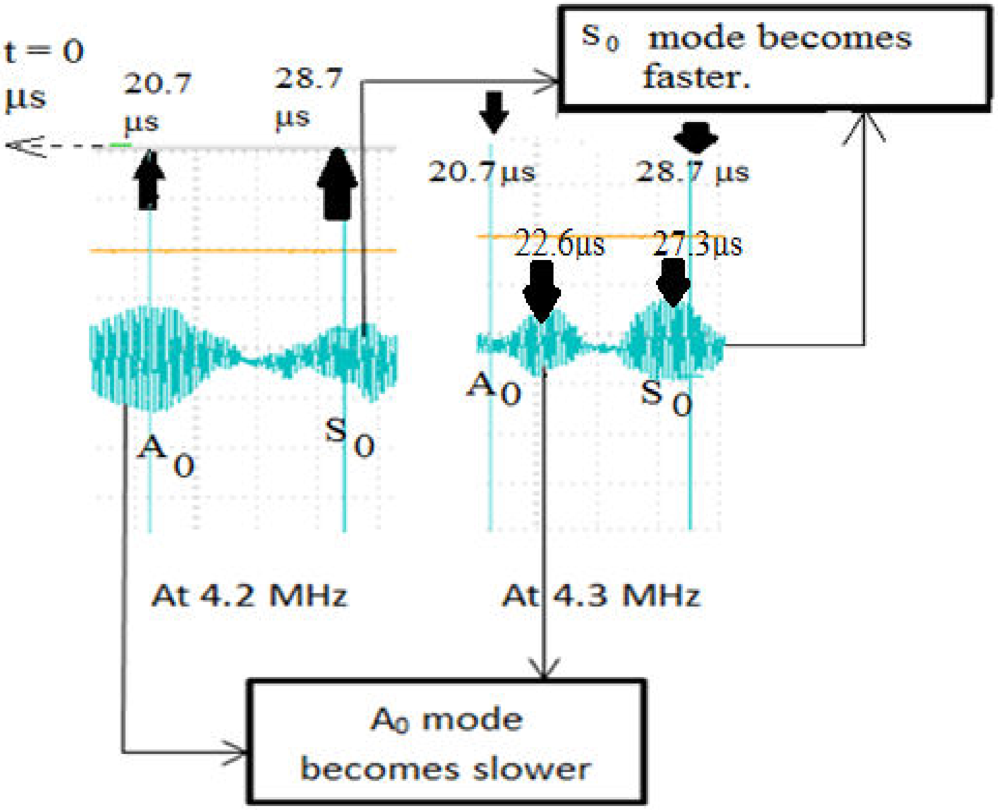

Figure B-4. Oscillograms showing the dispersive nature of the A_0 and S_0 modes.

VITA

Chandrima Chatterjee
PhD Candidate
Department of Physics and Astronomy, University of Mississippi

Education

- M.A. in Physics: The University of Mississippi, USA, **2014.**
- **Professional qualification:** B.Ed. (Bachelor of Education; with Physical Science and Mathematics): St. Xavier's College, University of Calcutta, India, **2011.** This is a professional degree, which is required to teach at the secondary and higher secondary school levels in India.
- M.Sc. in Physics: University of Calcutta, India, **2008.**
- B.Sc. in Physics (with Honors): University of Calcutta, India, **2006.**

Work Experience

- Instructor of PHYS 108 (Physical Science II), spring 2018, at the Department of Physics and Astronomy at the University of Mississippi. The course mainly covers the topics of electricity, magnetism, light and theory of relativity. The class comprises about 20 students.
- Teaching Assistant between Spring 2012 to Fall 2016, the Department of Physics and Astronomy at the University of Mississippi.: provided hands on experimental demonstration, instruction, guidance and evaluation on general physics labs.
- Research Assistant, summer 2012, summer 2014, summer 2015, summer 2016, spring 2017.
- Assistant Teacher of Physics at the Higher-secondary school level, Birla High School for Girls', Kolkata, India, 2011.
- Assistant Teacher of Physics at the Secondary and Higher-secondary school level, Methodist School, Dankuni, India, 2009-2010.

Leadership

- Co-founder and president (2016) of the University of Mississippi Women in Physics (UMWiP) group.
- Vice President of the Physics Graduate Student's Association (2015), Department of Physics and Astronomy, The University of Mississippi
- Member of the organizing committee for the Conference for Undergraduate Women in Physics (CUWIP), 2015, held at the University of Mississippi.

Publications

- Chandrima Chatterjee and Igor Ostrovskii, "Distribution of point defects in phononic periodically poled lithium niobate", Proceedings of Meetings on Acoustics **30**, 065008 (2017). (Online available at: http://asa.scitation.org/doi/abs/10.1121/2.0000556).

- Igor Ostrovskii, Oleg Korotchenkov, Nikolaj Borovoy, Andriy Nadtochiy, Roman Chupryna and Chandrima Chatterjee, "Nonstructural acousto-injection luminescence in metalized lithium niobate wafers", Ferroelectrics **514**:1, pp. 82-88 (2017). (Online available at: http://www.tandfonline.com/doi/full/10.1080/00150193.2017.1357957)

- Chandrima Chatterjee, and Igor Ostrovskii, "Nonuniform distribution of point defects in ferroelectric phononic crystal", The Journal of the Acoustical Society of America **141**, 3640 (2017). (Online available at: http://asa.scitation.org/doi/abs/10.1121/1.4987855).

- Chandrima Chatterjee, Lucien Cremaldi, and Igor Ostrovskii, "Nonclassical nonlinearity and crystal defects in lithium niobate", The Journal of the Acoustical Society of America **140**, 3324 (2016). (Online available at: http://asa.scitation.org/doi/abs/10.1121/1.4970590).

- Igor Ostrovskii, Oleg Korotchenkov, Nikolaj Borovoy, Andriy Nadtochiy, Roman Chupryna and Chandrima Chatterjee, "Nonstructural acousto-injection luminescence in metalized lithium niobate", The Journal of the Acoustical Society of America **139**, 2153 (2016). (Online available at: http://asa.scitation.org/doi/abs/10.1121/1.4950367).

- Chandrima Chatterjee and Igor Ostrovskii, "Nonuniform electromechanical efficiency and point defects in lithium niobate", The Journal of the Acoustical Society of America **142**, 2722 (2017). (Online available at: http://asa.scitation.org/doi/abs/10.1121/1.5014933).

- Chandrima Chatterjee and Igor Ostrovski, "Distribution of point defects in lithium niobate and defect-dependent electromechanical coupling", Proceedings of Meetings on Acoustics **31**, 045003 (2017). (Online available at: https://asa.scitation.org/doi/abs/10.1121/2.0000774).

- Chandrima Chatterjee, Daniel Miller and Igor Ostrovskii, "Comparative study of impurities in lithium tantalite and lithium niobate", The Journal of the Acoustical Society of America **143**, 1918 (2018). (Online available at: https://asa.scitation.org/doi/abs/10.1121/1.5036253).

Presentations

- Chandrima Chatterjee and Igor Ostrovskii, "Point Defects in Lithium Niobate", 8th Annual Research Symposium of the Graduate Student Council at the University of Mississippi, March, 2018 (Won second place in the STEM category).

- Chandrima Chatterjee and Igor Ostrovskii, "Nonuniform electromechanical efficiency and point defects in lithium niobate", 174th Meeting of the acoustical Society of America, New Orleans, December, 2017.

- Chandrima Chatterjee and Igor Ostrovskii, "Nonuniform distribution of point defects in ferroelectric phononic crystal", 173rd Meeting of the Acoustical Society of America and the 8th Forum Acusticum, Boston, June, 2017.

- Chandrima Chatterjee, "Experimental investigation of impurities and their effect on acousto-electric properties of lithium niobate", Colloquium at the Department of Physics and Astronomy, the University of Mississippi, October, 2016.

- Chandrima Chatterjee, “Point Defects in Lithium niobate”, University of Mississippi and University of Mississippi Medical Center Research Day, March 3, 2016.

- Chandrima Chatterjee, “Acoustical Memory in Lithium niobate”, 3 Minute Thesis Competition, The University of Mississippi , October, 2014 (Finalist).

- Chandrima Chatterjee, “Properties and Uses of Ferroelectric Materials”, 3 Minute Thesis Competition, The University of Mississippi , October, 2015 (Won second place in the PhD category).

- Chandrima Chatterjee and Igor Ostrovskii, “Distribution of Impuritites in Lithium niobate”, 82nd Meeting of the Southeastern Section of The American Physical Society, November, 2015, University of South Alabama, Mobile, Al.

- Chandrima Chatterjee, “Acoustical Memory in a YZ-Cut Lithium Niobate Plate”, Mississippi Academy of Sciences, Seventy-Ninth Annual Meeting, February, 2015, University of Southern Mississippi, Hattiesburg, MS.

- Chandrima Chatterjee, “Acoustical Memory in Lithium niobate”, APS Conference for Undergraduate Women in Physics, January 16-18, 2015, University of Mississippi.

- Saminda Adikaram, Chandrima Chatterjee, Igor Ostrovskii, “Lamb Wave Propagation in Electronic Material Plates”, Mississippi Academy of Sciences, Seventy-Eighth Annual Meeting, March, 2014, Lake Terrace Convention Center, Hattiesburg, MS.

Honors, awards and fellowship

- Dissertation Fellowship by University of Mississippi Graduate School for Spring 2017.

- Awarded grant for Women in Physics by The American Physical Society on November 2015. The Grant money will be received by the Department of Physics and Astronomy for running the University of Mississippi Women in Physics group (UMWiP) in the Department.

- Won the second place in the PhD category of The 3 Minute Thesis competition organized by the graduate school at the University of Mississippi. This is a competition where graduate students need to present one’s research in 3 minutes.

- Zdravko Stipcevic Honors, The Department of Physics and Astronomy, the University of Mississippi (2012-present).

- Inducted into Sigma Pi Sigma (2016).

Affiliations and memberships

- American Physical Society (APS)
- Society of Physics Students (SPS)
- Acoustical Society of America (ASA)
- Physics Graduate Students Association (PGSA), The Department of Physics and Astronomy, The University of Mississippi
- University of Mississippi Women in Physics (UMWiP)